An Environmental Test Stand for Large Area Testing of Silicon Photomultipliers

Lucas Darroch

A thesis submitted to McGill University in partial fulfillment of the requirements of the degree of Master of Science in Physics.

Department of Physics

McGill University

Montreal

Abstract

The discovery of massive neutrinos allows us to question their nature: are they Dirac or Majorana particles? The latter would be a new kind of fundamental particle, violating lepton number conservation through a particle to antiparticle transition. The most promising route to determining whether the neutrino is a Majoran is through neutrinoless double beta decay. nEXO is a next generation time projection chamber searching for neutrinoless double-beta decay in 5 tonnes of liquid xenon (LXe) enriched in the isotope ^{136}Xe. Interactions within LXe produce anti-correlated scintillation and ionization signals, which will be used to reconstruct the energy and position of each event. Silicon photomultipliers (SiPMs) have been identified as the devices to detect the vacuum ultraviolet scintillation light for nEXO. SiPMs are silicon devices ~ 1 cm^2 with single photon sensitivity, and have a quantum efficiency of $\sim 15\%$ at 175 nm. A baseline characterization of the many SiPMs that will be distributed among the nEXO collaboration is necessary: the detector will employ tiles of SiPMs, organized into staves, yielding a photo-coverage area of ~ 4.5 m^2. The development of integrated SiPM tiles is advanced within the collaboration, requiring precise testing in conditions similar to their deployment. This thesis presents the results from the design, assembly, and commissioning of an environmental test stand for measuring ~ 150 cm^2 of SiPMs at 168 K with quick turnaround between tile deployment, facilitating both a high-rate of baseline SiPM characterization, and precision testing of integrated tiles. In addition, some analysis for EXO-200, the prototype experiment for nEXO, is presented.

Résumé

La découverte des neutrinos massifs permet de s'interroger sur leur nature : s'agit-il de particules de Dirac ou de Majorana? Ce dernier serait un nouveau type de particule fondamentale, en violation de la conservation du nombre de leptons par une transition de particule à antiparticule. La voie la plus prometteuse pour déterminer si le neutrino est un Majoran est la double désintégration bêta sans émission de neutrinos. nEXO est une chambre à projection temporelle de la prochaine génération à la recherche d'une désintégration bêta double sans émission de neutrinos dans 5 tonnes de xénon liquide (LXe) enrichi en isotope ^{136}Xe. Les interactions au sein de LXe produisent des signaux de scintillation et d'ionisation anticorrélés, qui seront utilisés pour reconstruire l'énergie et la position de chaque événement. Les photomultiplicateurs au silicium (SiPMs) ont été identifiés comme étant les dispositifs permettant la détection de la lumière de scintillation ultraviolette sous vide pour le nEXO. Les SiPMs sont des dispositifs en silicium $\sim$ 1 cm^2 avec sensibilité à un seul photon, et ont une efficacité quantique de $\sim$ 15% à 175 nm. Une caractérisation de base des nombreux SiPMs qui seront perturbés dans le cadre de la collaboration nEXO est nécessaire : le détecteur utilisera des tuiles de SiPMs organisées en douelles, ce qui donnera une surface de couverture de $\sim$ 4,5 m^2. Le développement des tuiles de SiPMs intégrées est avancé dans le cadre de la collaboration, nécessitant des tests prècis dans des conditions similaires à leur développement. Cette thèse présente les résultats de la conception, de l'assemblage et de la mise en service d'un banc d'essai environnemental pour mesurer $\sim$ 150 cm^2 des SiPMs à 168 K avec une rotation rapide entre le déploiement des tuiles, facilitant à la fois un taux élevé de caractérisation de base du SiPMs et des tests précis des tuiles intégrées. De plus, certaines analyses pour EXO-200, l'expérience prototype pour nEXO, sont présentées.

Acknowledgments

I would like to acknowledge the support of all those persons who made this work possible. To my advisor, Thomas Brunner, whose guidance has seen me through the design, construction, and commissioning of the hardware, and more generally helped me throughout my degree. Thomas McElroy, whose persistence in the lab has lent itself to linking the many parts of this project together. Chris Chambers, who helped troubleshoot the many leaks in the vacuum system. Xiao Shang, for help welding the nitrogen plumbing and assembling the apparatus. Tsvetelin Totev, for helping countless times throughout the assembly and commissioning of the setup. Pascal Bourseguin and the Physics Machine Shop, for the advice and training to develop the high-precision parts. Robert Gagnon for help brazing or bonding the many prototype vacuum parts. Electro Loh Plating for their in-kind support towards all the bits and pieces holding everything together. The Université de Montréal Physics Machine Shop, for machining the majority of the custom hardware. And to Shannon Harrington, for translating the abstract to French, and for supporting me throughout this endeavour.

Statement of Originality

This statement is to certify that the works presented in this document are original and my own, with any contributions acknowledged in the thesis. The design, assembly, and testing of the test stand, and the development of the thermal-network model, which are presented in Section 3, were completed by me. The refinement of the EXO-200 purity model, and the characterization of a systematic contamination of the xenon within the EXO-200 detector, which are presented in Section 4, were completed by me.

Lucas Darroch

Contents

List of Figures

List of Tables

1 Introduction

1.1 The Standard Model

The Standard Model of Particle Physics (SM) is a scientific theory poised to describe matter and its interactions at a fundamental level. The SM uses interacting Quantum Field Theories (QFTs) that are constructed largely through fundamental symmetries using Noether's theorem. Noether's theorem may be stated concisely: for every symmetry of the Lagrangian[1], there is a corresponding conserved quantity. Thus Noether's theorem gives a prescriptive method to constrain the possible QFTs in the SM: through experimentation, observe conserved quantities in Nature, then (re)organize a Lagrangian that can accommodate those conserved quantities through the appropriate symmetries. In QFTs, field excitations represent particles that propagate over all trajectories in a quantum mechanical superposition. All trajectories for a particle meet at an interaction vertex where the outgoing particles are created, and the incoming particles are annihilated; the combinations of particles that meet at a vertex stem from the symmetries embedded in the Lagrangian. The symmetries relevant to the SM are also constrained by the fact that they are field theories: fields or couplings in the Lagrangian with mass terms of higher order than some critical number become irrelevant in the continuum limit. The irrelevant terms lead to accidental symmetries, such as lepton and baryon number conservation.

Interactions between fields are related to the order of the fields, e.g., the product of three fields is a three point interaction vertex. In the SM, gauge fields are used to mitigate the interactions between matter fields, and other gauge fields, through a local gauge invariance symmetry; local gauge invariance is satisfied by replacing four-derivatives with covariant derivatives. Using natural units ($\hbar = c = 1$), in the case of quantum electrodynamics (QED), the local U(1) gauge symmetry allows the introduction of the gauge field, A_μ, and fundamental unit of charge, e ; the Lagrangian for QED is [1]:

[1] A symmetry of the Lagrangian is a transformation that leaves the Lagrangian unchanged.

$$\mathcal{L}_{QED} = \bar{\psi_e}\ (i\gamma^\mu\partial_\mu - m_e\ )\,\psi_e\ + e\,\bar{\psi_e}\,\gamma^\mu\psi_e\,A_\mu - \frac{1}{4}F_{\mu\nu}F^{\mu\nu}. \tag{1}$$

By identifying $-e\,\bar{\psi_e}\,\gamma^\mu\psi_e$ as the four-vector current, j^μ, the QED Lagrangian can be connected to the Maxwell Lagrangian:

$$\mathcal{L}_{QED} = \mathcal{L}_{\text{Dirac}} + \mathcal{L}_{\text{Maxwell}}, \tag{2}$$

where $\mathcal{L}_{\text{Dirac}} = \bar{\psi_e}\ (i\gamma^\mu\partial_\mu - m_e\ )\,\psi_e$, and $\mathcal{L}_{\text{Maxwell}} = -j^\mu A_\mu - \frac{1}{4}F_{\mu\nu}F^{\mu\nu}$. The SM, which describes Quantum Chromo Dynamics (QCD), the weak interaction, and QED, can be generated by extending the required local gauge symmetry of the Lagrangian to the SU(3), SU(2), and U(1) gauge transformations; the quantization of these gauge fields results in the color gluons, W and Z, and photon quanta, respectively. However, local gauge symmetry fails to correctly describe particle masses. In the SM, the masses of the W, Z, and fermions are generated through the Higgs mechanism: spontaneous symmetry breaking of a gauge invariant complex scalar field (Higgs field, ϕ) allows interactions between the non-zero vacuum expectation of the Higgs field and massless gauge/fermionic fields. In the unitary gauge ($\phi = \mathcal{R}e\,\{\phi\}$), the Lagrangian for the SU(2) doublet containing the electron is [1]:

$$\mathcal{L}_{\,e}\ = -\frac{g_e}{\sqrt{2}}v\bar{\psi_e}\,\psi_e\ - \frac{g_e}{\sqrt{2}}h\bar{\psi_e}\,\psi_e\,, \tag{3}$$

where ψ_e is the electron field, v is the non-zero expectation of the Higgs field, and h is the Higgs boson. By choosing $g_e\ = \sqrt{2}\frac{m_e}{v}$, the Lagrangian becomes

$$\mathcal{L}_{\,e}\ = -m_e\,\bar{\psi_e}\,\psi_e\ - \frac{m_e}{v}\bar{\psi_e}\,\psi_e\,h, \tag{4}$$

and the electron has 'gained' a mass through an interaction with the Higgs field.

1.2 Neutrinos in the Standard Model

The W and Z bosons are particularly important for neutrino physics, since they are the only coupling neutrinos have to the other fermion fields. Due to this coupling, neutrinos are not directly observed, but rather are observed indirectly through their weak interactions. Three distinct flavor states for neutrinos exist, the v_e, v_μ, and v_τ; this postulate comes from the observation that neutrinos produced from charged current interactions with electrons can go on to induce further charged current interactions with electrons; the same is true for neutrinos produced in charged current interactions with muons, and tau electrons. Therefore, the neutrinos produced in charged current interactions with leptons carry some property that is related to the lepton that is conserved at interaction vertices: lepton flavor number [1]. For this reason, neutrinos produced in charged current interactions with electrons are referred to as electron neutrinos. For each flavor, leptons are assigned +1 if they are particles, and -1 if they are antiparticles. The process of lepton flavor conservation, as described above using $\beta^{\pm}$ decay, is shown in Figure 1-1.

Chirality is an important structure for weak interactions in the SM. Using the chiral projection operators, $\hat{P_R}$ and $\hat{P_L}$, which are defined by

$$\hat{P_R} = \frac{1}{2}\left(1+\gamma^5\right), \quad \text{and} \tag{5}$$

$$\hat{P_L} = \frac{1}{2}\left(1-\gamma^5\right), \tag{6}$$

any spinor, u, can be decomposed into chiral states:

$$u = (\hat{P_R}+\hat{P_L})u = \hat{P_R}u + \hat{P_L}u = u_R + u_L, \tag{7}$$

where u_R and u_L are eigenstates of the γ^5 matrix, with eigenvalues +1 and -1, respectively; for a more complete discussion of the γ matrices and spinors, see a QFT reference text [1, 2].

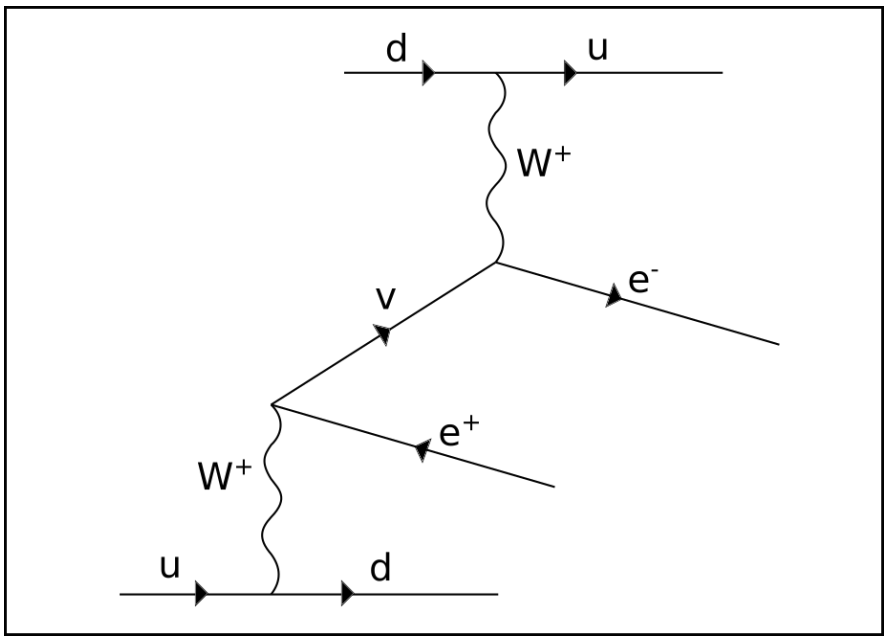

Figure 1-1: Feynman diagram showing conservation of lepton flavor number in charged-current interactions. Neutrinos produced along with an electron can induce further charged-current interactions with electrons. This observation suggests that neutrinos have some intrinsic property, flavor, which is associated with a particular generation of lepton, and is conserved at each interaction vertex [1].

Charged weak interactions have an inherently chiral structure since the interaction vertex has the factor [1]

$$\frac{-ig_W}{2\sqrt{2}}\gamma^\mu\left(1-\gamma^5\right), \tag{8}$$

where g_W is the W coupling. Equation 8 is called a 'vector minus axial-vector' (V-A) interaction because of the $\gamma^\mu - \gamma^\mu\gamma^5$ term. The chiral nature of charged-weak interactions can be shown using the corresponding four-vector current:

$$j^\mu = \frac{g_W}{2\sqrt{2}}\bar{u}\gamma^\mu\left(1-\gamma^5\right)u = \frac{g_W}{\sqrt{2}}\bar{u}\gamma^\mu\hat{P}_L u. \tag{9}$$

Matrix multiplication of the chiral projection operators shows that $\hat{P}_R\hat{P}_R = \hat{P}_R$, $\hat{P}_L\hat{P}_L = \hat{P}_L$,

and $\hat{P}_R\hat{P}_L = \hat{P}_L\hat{P}_R = 0$, which implies

$$\bar{u}\gamma^\mu \hat{P}_L u = \bar{u}\gamma^\mu \hat{P}_L\hat{P}_L\hat{P}_L u \tag{10}$$

$$= \bar{u}\hat{P}_R\gamma^\mu \hat{P}_L\hat{P}_L u \tag{11}$$

$$= \left(\hat{P}_L u\right)^\dagger \gamma^0\gamma^\mu \hat{P}_L \left(\hat{P}_L u\right) \tag{12}$$

$$= {u_L}^\dagger \gamma^0\gamma^\mu \hat{P}_L u_L \tag{13}$$

$$= \bar{u_L}\gamma^\mu \hat{P}_L u_L, \tag{14}$$

where the commutation of γ^μ and P_L used $\{\gamma^\mu, \gamma^5\} = 0$. Therefore, Equation 9 is equivalent to

$$j^\mu = \frac{g_W}{2\sqrt{2}}\bar{u_L}\gamma^\mu \left(1 - \gamma^5\right) u_L, \tag{15}$$

indicating that only chiral (right) left handed (anti)particles participate in charged weak currents. A similar equation is true for antiparticle spinors, w:

$$\bar{w}\gamma^\mu P_L w = \bar{w_R}\gamma^\mu P_L w_R, \tag{16}$$

where P_L projects out right handed chiral antineutrino states. Although weak neutral currents couple to left and right handed chiral particle/antiparticle states, they are still V-A interactions, so the currents for the same combinations of left/right handed chiral interactions is zero [1].

1.3 Neutrinos Beyond the Standard Model

The solar neutrino problem was a long standing disagreement between theory and experiment: models for stellar dynamics predicted a certain flux of electron neutrinos from the

fusion within our Sun - measurements of inverse beta-decay showed that the number of electrons was less than expected [3]. This disagreement was particularly egregious because the nuclear process for stellar dynamics was well understood [4, 5]. The observed neutrino flux was reconciled with stellar dynamics following the discovery of neutrino oscillations [6, 7]: the flavor state of neutrinos may change as they propagate through spacetime[2]. The accepted explanation for neutrino oscillations is that neutrinos have mass, and that neutrino mass eigenstates are distinct from flavor eigenstates, i.e., flavor eigenstates can be constructed as a superposition of neutrino mass eigenstates, by [9]:

$$\begin{bmatrix} \nu_e \\ \nu_\mu \\ \nu_\tau \end{bmatrix} = \begin{bmatrix} U_{e1} & U_{e2} & U_{e3} \\ U_{\mu 1} & U_{\mu 2} & U_{\mu 3} \\ U_{\tau 1} & U_{\tau 2} & U_{\tau 3} \end{bmatrix} \begin{bmatrix} \nu_1 \\ \nu_2 \\ \nu_3 \end{bmatrix}, \tag{17}$$

where ν_1, ν_2, and ν_3 are the neutrino mass eigenstates, and $U_{\alpha i}$ are the entries of the Pontecorvo-Maki-Nakagawa-Sakata (PMNS) matrix, with Greek letters denoting flavor states, and Latin numbers for mass state. When a pure flavor state is created at a charged current interaction vertex, it can be expressed as a superposition of the mass states through Equation 17; the mass states are eigenstates of the free-particle Hamiltonian [10]. As time evolves, each mass eigenstate in the superposition gains a phase factor $\exp(-E_i t)$. Neutrinos are ultra-relativistic particles, so $E_i = \sqrt{p^2 + m_i^2} \approx p + m_i^2/2E$, and the probability for a neutrino created in flavor state α to transition to flavor state β is

$$\begin{aligned} P(\nu_\alpha \to \nu_\beta) = \delta_{\alpha\beta} &- 4 \sum_{i<j} \Re \left[U_{\alpha i} U^*_{\beta i} U^*_{\alpha j} U_{\beta j} \right] \sin^2 \left(\frac{\Delta m^2_{ji} t}{4E} \right) \\ &+ 2 \sum_{i<j} \Im \left[U_{\alpha i} U^*_{\beta i} U^*_{\alpha j} U_{\beta j} \right] \sin^2 \left(\frac{\Delta m^2_{ji} t}{4E} \right). \end{aligned} \tag{18}$$

[2]Takaaki Kajita and Arthur B. McDonald were awarded the 2015 Nobel Prize in Physics "for the discovery of neutrino oscillations, which shows that neutrinos have mass [8]."

So the transition probability between flavor states depends on the entries of the PMNS matrix and the mass-squared differences, $\Delta m^2_{ij} = m^2_i - m^2_j$. Therefore neutrino oscillation experiments cannot constrain the absolute mass scale of neutrinos. However, mass-squared differences do give information on the relative mass scale of neutrinos. There are a number of experiments working to constrain parameters for neutrino oscillations using solar, atmospheric, reactor, and beam-line neutrinos that are omitted for brevity: perhaps the three most relevant experiments for a presentation of the neutrino mass hierarchy are KamLAND, MINOS, and Planck. The Kamioka Liquid Scintillator Antineutrino Detector (KamLAND) experiment uses the known flux of $\bar{\nu}_e$ emitted from nearby commercial nuclear reactors to study neutrino oscillations through inverse-beta decay. Using a two-neutrino model with combined results from SNO [11] and solar flux experiments [12], the KamLAND collaboration has reported $\Delta m^2_{21} \approx (7.6 \pm 0.2) \times 10^{-5}$ eV^2 [13]. The Main injector neutrino oscillation search (MINOS) experiment uses an accelerator to produce a beam of neutrinos to study oscillations spanning the distance between a near (on-site) and far (734 km) detector. The MINOS experiment is sensitive to the larger mass-splitting, through the disappearance of ν_μ, and has reported $|\Delta m^2_{32}| \approx (2.3 \pm 0.1) \times 10^{-3}$ eV^2 [14]. Studies of the cosmic microwave background (CMB), specifically the Planck collaboration, have set a limit of the sum of neutrino masses as $\sum m_i < 0.12$ eV [15]. When combined, these measurements provide three possible mass hierarchies for neutrinos: normal, $m_1 < m_2 << m_3$, inverted, $m_1 \approx m_2 >> m_3$, and degenerate, $m_1 \approx m_2 \approx m_3$. Due to the relative nature of the constraints on neutrino mass, the lightest neutrino mass is unconstrained; Figure 1-2 shows the neutrino masses for all three ordering schemes, as a function of the lightest neutrino mass [9].

1.4 Neutrino Mass

Massive neutrinos require a mechanism to generate their mass; the simplest and most consistent way to generate neutrino masses is through the conjugate Higgs mechanism, similar to the up quark [1]. In the unitary gauge, the Lagrangian for the SU(2) conjugate doublet

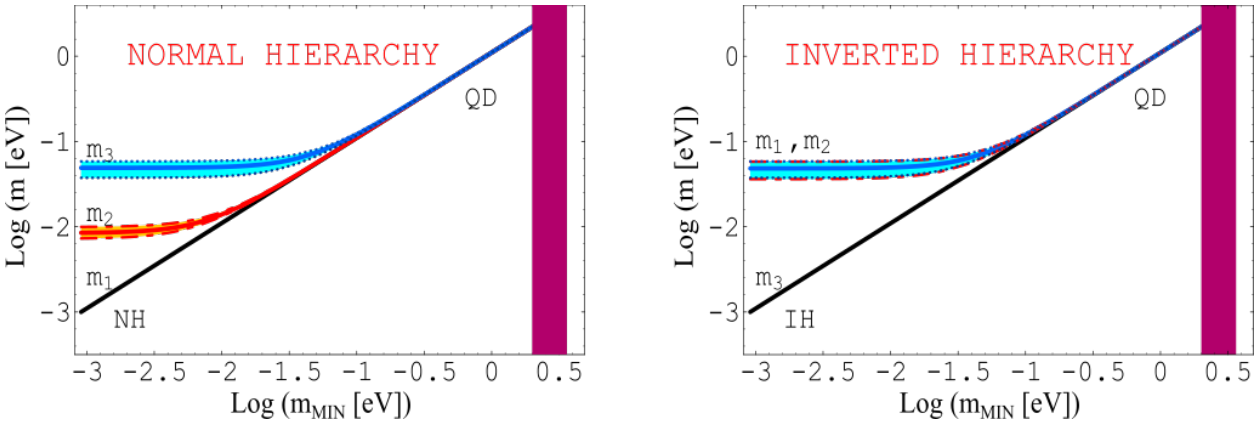

Figure 1-2: The normal (left) and inverted (right) mass hierarchies for neutrinos, as a function of the lightest neutrino mass. When the lightest neutrino mass is ~ 0.1 eV, the mass spectrum is degenerate. Figure reproduced from [9].

containing the neutrino is [1]:

$$\mathcal{L}_{\nu} = -\frac{g_\nu}{\sqrt{2}} v \bar{\nu} \nu, \tag{19}$$

where ν is the neutrino field. After decomposing the neutrino fields into chiral states, we find

$$\mathcal{L}_{\nu} = -\frac{g_\nu}{\sqrt{2}} v \left(\bar{\nu}_R \nu_L + \bar{\nu}_L \nu_R \right). \tag{20}$$

Here we see the introduction of right handed chiral neutrino states, which are excluded in all SM processes. By choosing $g_\nu = \sqrt{2}\frac{m_D}{v}$, the neutrino mass is

$$m_D = \frac{g_\nu v}{\sqrt{2}}. \tag{21}$$

Neutrino masses are much smaller than the other fermions in each generation, which, if the neutrino mass is generated through the above process, requires a particularly small coupling to the Higgs; a plot showing the masses of the fermions is shown in Figure 1-3 [1]. However, the right (left) handed chiral (anti)neutrinos are electroweak singlets with no coupling to the W or Z: they may be added to the Lagrangian without upsetting the SM gauge invariance.

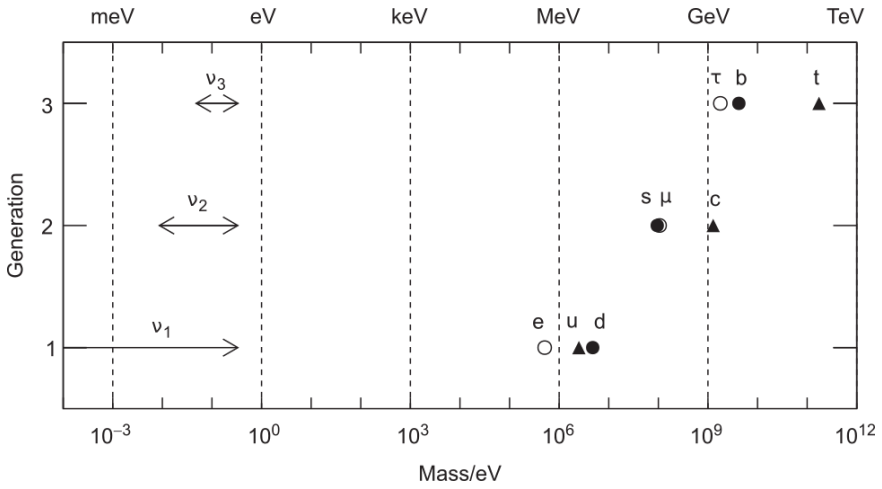

Figure 1-3: Fermion masses grouped by each generation; the normal hierarchy is assumed for the neutrino masses. The neutrino masses are ~ 10 orders of magnitude smaller than the other fermions in each generation, indicating either a small coupling between the neutrino and the Higgs, or some unknown mechanism for mass generation. Figure reproduced from [1].

By utilizing right handed chiral neutrino fields, and their CP conjugates, a new mass term can be constructed [1]:

$$\mathcal{L}_M = -\frac{1}{2} M \left(\bar{\nu_R^c}\nu_R + \bar{\nu_R}\nu_R^c\right) + \text{h.c.}, \tag{22}$$

where M is the Majorana mass, $\nu_R^c = \hat{C}\hat{P}\nu_R$ is a left handed anti neutrino, $\hat{C}$ is the charge conjugation operator, $\hat{P}$ is the parity operator, and h.c. is the Hermitian conjugate. Equation 22 provides a direct coupling between particle and antiparticle states, therefore charged fermions cannot have a Majorana mass term since they have a local symmetry associated with charge. Due to the existence of the hypothetical Majorana mass term in the Lagrangian, Equation 20 is referred to as the Dirac mass term, and the mass coefficient as the Dirac mass (m_D). The most general Lagrangian that includes right handed chiral neutrinos will include both a Dirac and Majorana mass term; as a matrix equation, the combined Lagrangian is

$$\mathcal{L} = -\frac{1}{2}\begin{bmatrix}\bar{\nu}_L \bar{\nu^c_R}\end{bmatrix}\begin{bmatrix}0 & m_D \\ m_D & M\end{bmatrix}\begin{bmatrix}\nu^c_L \\ \nu_R\end{bmatrix} + \text{h.c.} \tag{23}$$

In the limit $M >> m_D$, the eigenvectors for the matrix in Equation 23 correspond to heavy and light physical neutrino states, with approximate masses M and m_D^2/M, respectively. The mass of the light neutrino state can be made consistent with the observed neutrino mass if both the Majorana mass is taken near the GUT scale, and the Dirac mass is taken near the fermion scale. This arrangement is attractive as it allows the neutrinos to couple to the Higgs with the same strength as the other fermions, while also explaining the smallness of the neutrino mass. This combination of Dirac and Majorana masses 'lifting-up' a light neutrino state while 'driving-down' a heavy neutrino state is referred to as the Seesaw mechanism [16]. However, there is as of yet no experimental evidence to support the Seesaw mechanism hypothesis. If the Majorana (and Dirac) mass term for the neutrino is realized in Nature, then the Lagrangian would describe Majorana neutrinos. Therefore a positive signal of an neutrino to antineutrino transition[3] would not only imply that neutrinos are Majorana particles, a new class of particle, but would also lend credibility to the Seesaw mechanism, thereby explaining the relative smallness of the neutrino mass. The most promising experimental method to detect a neutrino to antineutrino transition is by searching for neutrinoless double beta decay ($0\nu\beta\beta$), which is explained in the next section.

[3]A neutrino to antineutrino transition may also explain the matter-antimatter asymmetry in the Universe through lepton number violation [9].

2 The Search for Majorana Neutrinos with $0\nu\beta\beta$

2.1 $0\nu\beta\beta$ Detectors

Two neutrino double beta decay ($2\nu\beta\beta$) is a SM process that occurs in certain even-even isotopes, where a single beta decay is either forbidden or suppressed; $2\nu\beta\beta$ was first proposed by Maria-Gopert Mayer [17], and has been observed in several isotopes [18]. Neutrinoless double beta decay is a hypothetical double beta decay process without neutrino emission, requiring a neutrino to antineutrino transition [19]. Since an observation of $0\nu\beta\beta$ would imply that neutrinos are Majorana particles, this has been a focus of the international science community. Several tonne-scale discovery experiments are searching in various candidate isotopes, utilizing distinct technologies [20–25]; these experiments will be discussed briefly below, with the relevant parameters organized into Table 2-1.

The Large Enriched Germanium Experiment for Neutrinoless Double-Beta Decay (LEGEND) [20] collaboration is developing a detector to search for $0\nu\beta\beta$ in ^{76}Ge, using high-purity germanium (HPGe) detectors. The LEGEND programme builds off the successes of both the Majorana Demonstrator [26] and Germanium Detector Array (GERDA) [27] experiments, which employ p-type point-contact HPGe diodes, enriched to $\sim 87\%$ in the isotope ^{76}Ge, as both the decay source and detector. HPGe detectors have the advantage of high-intrinsic energy resolution and low backgrounds around the region of interest, $Q_{0\nu\beta\beta} = 2039$ keV; here $Q_{0\nu\beta\beta}$ is the energy that would be released from a hypothetical $0\nu\beta\beta$ for the isotope being discussed. The LEGEND collaboration is realized through the merger of the GERDA and MAJORANA collaborations.

The Cryogenic Underground Observatory for Rare Events (CUORE) [21, 28] collaboration is searching for $0\nu\beta\beta$ in ^{130}Te, $Q_{0\nu\beta\beta} = 2527.5$ keV, using tellurium dioxide (TeO_2) crystals. The CUORE detector consists of 988 tellurium crystals, each made with natural tellurium ($\sim 34\%$ ^{130}Te), that act as both the decay source and detector. Each crystal is a bolometer that is cooled to ~ 10 mK; the heat generated from particle interactions

is measured by a thermistor. R&D efforts have begun on a follow-up experiment titled CUORE upgade with particle ID (CUPID) [22]. The CUPID-0 experiment is searching for $0\nu\beta\beta$ in ^{82}Se, $Q_{0\nu\beta\beta} = 2997.9$ keV, using 24 cylindrical ZnSe crystals, enriched to 95% in the isotope ^{82}Se. The primary technology improvement for CUPID is made through scintillating bolometers, which allows simultaneous measurements of the calormetric signal and scintillation light; energy is reconstructed in the same way as CUORE using the calorimetric signal, and the type of interaction can be identified through the scintillation light, which significantly lowers the background contribution.

The Kamioka Liquid Scintillator Antineutrino Detector (KamLAND) [29] collaboration has built a detector to study neutrino oscillations and geoneutrinos. The detector employs liquid scintillator (LS) within a 13 m diameter balloon. 1879 photomultiplier tubes (PMTs) are embedded in the inner walls of the containment vessel, facing the balloon. Antineutrinos are studied via inverse beta-decay reactions within the detector, by searching for the delayed coincidence from (fast) electron/positron annihilation and (slow) neutron capture. Following the completion of this project, the KamLAND collaboration evolved into the KamLAND-Zen [23] collaboration, which is searching for $0\nu\beta\beta$ in ^{136}Xe $Q_{\beta\beta} = 2458.08 \pm 0.31$ keV [30]. A $\sim$ 3 m inner balloon was lowered into the 13 m diameter outer balloon, and filled with LS spiked with Xe ($\sim$ 350 kg in phase-I, and 420 kg in phase-II), enriched to $\sim$ 91% in the isotope ^{136}Xe. Currently, the KamLAND-Zen collaboration has the most stringent half-life limit for $0\nu\beta\beta$ in ^{136}Xe and has loaded 750 kg of xenon for the next phase of running, KamLAND-Zen 800 [31].

The Sudbury Neutrino Observatory (SNO) [32] collaboration built a detector to study neutrino oscillations. The detector employed 1000 tonnes of heavy water within a 12 m diameter acrylic vessel. $\sim$ 9600 PMTs were embedded in a 19 m containment sphere, facing the acrylic vessel. Charged current, neutral current, and electron elastic scattering were studied through interactions between solar neutrinos and the heavy water. Similar to KamLAND, following the completion of its research programme, the SNO collaboration evolved into the

SNO+ [25, 33] collaboration. There are several physics goals for SNO+ that are organized into three operational phases; the final phase includes a search for $0\nu\beta\beta$ in ^{130}Te, and other exotic physics. The $0\nu\beta\beta$ search is achieved by filling the acrylic vessel with $\sim$ 4 tonnes of natural Te ($\sim$ 34% ^{130}Te) spiked LS. The SNO+ collaboration has projected a half-life sensitivity of $\sim 10^{26}$ yr to $0\nu\beta\beta$ in ^{130}Te assuming five years of operation, with an energy resolution of $\sim$ 10%.

The (n)Enriched Xenon Observatory (nEXO) [24] collaboration is developing a detector to search for $0\nu\beta\beta$ in liquid ^{136}Xe. The detector is a single phase, monolithic time-projection chamber (TPC). The detector utilizes 5-tonnes of LXe, enriched to 90% in the isotope ^{136}Xe, as both the decay source and detection medium. Scintillation and ionization are measured simultaneously using ~ 4.5 m^2 of silicon photomultipliers (SiPMs) for light detection, and $\sim$ 1 m^2 of fused silica tiles for charge collection. The nEXO programme builds off the success of EXO-200 [34], a similar single-phase LXe TPC, which decommissioned in December 2018. As R&D for the nEXO detector (and some analysis for EXO-200) is the focus of this work, the physics of the detector will be discussed in detail below.

2.2 Properties of LXe

There are several properties of LXe that make it an ideal candidate as a detection medium for a $0\nu\beta\beta$ search; given the scope of this work, the complete set of properties which are applicable more generally to particle physics will be omitted.

Xe is an inert gas, and so electrons/ions liberated through ionization will not form new chemical species within the detector, which would alter the macro/microscopic properties of the medium (with the exception of recombination); an inert medium is important for high-efficiency charge collection where electrons(ions) drift in an electric field towards an anode(cathode). The ionization potential for LXe (15.6$\pm$0.3 eV [35]) is lower than that for LAr (23.6$\pm$0.3 eV [36]) or LKr (18.4$\pm$0.3 eV [37]), which maximizes the ionization yield for a given energy deposition. A minimum ionizing particle (MIP) creates a low ionization density

Detector	Active Medium	Stage	Energy Resolution [$\frac{\text{FWHM}}{\text{Q}}$%]	Background [$\frac{\text{cts}}{\text{FWHM}\cdot\text{kg}\cdot\text{yr}}$]	Exposure [kg · yr]	$t_{1/2}^{0\nu\beta\beta}$ sensitivity [$\times 10^{25}$yr]	Half-life limit [$\times 10^{25}$yr]
GERDA [40]	^{76}Ge	Taking Data	0.16	1.86 $\times 10^{-3}$	82.4	11	> 9.0
Majorana Demonstrator [26]	^{76}Ge	Taking Data	0.12	11.9 $\times 10^{-3}$	26.0	4.8	> 2.7
LEGEND [20]	^{76}Ge	R&D	0.12	10^{-3}	-	1000	-
CUORE [21, 28]	^{130}Te	Taking Data	0.3	0.11	86.3	0.7 9.0 after 5 years	> 1.5
CUPID-0 [22]	^{82}Se	Phase-I Complete	0.67	7.0 $\times 10^{-2}$	5.29	0.5	> 0.35
KamLAND-Zen [23, 40]	^{136}Xe	Taking Data	11	0.45	504	5.6	> 10.7
EXO-200 [34]	^{136}Xe	Complete	1.15	0.13	234.1	5.0	> 3.5
nEXO [24, 41]	^{136}Xe	R&D	≤ 1.0	8.6 10^{-4}	-	920	-

Table 2-1: Published results and selected performance parameters for a number of experiments searching for $0\nu\beta\beta$. The SNO+ experiment has been excluded from this table since many of its parameters have not been published.

in LXe, which leads to a low rate of recombination when contrasted against a relativistic heavy ion. The low rate of recombination for MIPs in LXe allows nearly complete charge collection under modest electric fields [38]. This property is useful for a $0\nu\beta\beta$ search, since charge collection is generally more efficient than light collection[4], and the energy of a minimally ionizing electron in LXe is of the same order as the Q-value for $0\nu\beta\beta$ in ^{136}Xe; a plot of $-\langle dE/dx\rangle$ for xenon is shown in Figure 2-1 [39]. An impediment to high-efficiency charge collection is contamination of xenon with electronegative impurities, which can form stable molecules with liberated electrons, attenuating the collected charge. Continuous xenon purification is required to remove electronegative impurities that limit the energy resolution, and radioactive impurities that would constitute a substantial background within the fiducial volume of the detector.

The characteristic decay curves for MIPs and heavy-ion scintillation yield in LXe can be used for particle identification, since the (singlet) decay time from heavy-ion excitation is an order of magnitude faster than the decay time for electrons; a plot of the decay times for heavy-ions and electrons is shown in Figure 2-2 [42].

Of the stable rare gasses, xenon has the highest atomic number; this property is important for self-shielding, since a monolithic volume of xenon will not only have a greater fiducial volume than another rare gas, but will also have a greater ratio of fiducial volume to total volume than pixelated media; the attenuation length of γ-rays (γs) near the $0\nu\beta\beta$ Q-value in LXe is $\lambda_{att} \sim 8.7$ cm [43]. Natural xenon has a large ($\sim 8.8\%$ [44]) relative abundance of ^{136}Xe, which makes it feasible to enrich a large mass of xenon through centrifuges.

Possibly the most important property of LXe is the anticorrelation between the number of electrons and photons produced from an energy deposition [45]: the correlation leads to correlated fluctuations in particle number, which can be used to achieve high energy resolution when charge and light are measured simultaneously.

[4]The number of detected photons is scaled by attenuation through the media, obstructing (reflective) surfaces, photocoverge area, and the quantum efficiency of the photodetector.

Figure 2-1: Stopping power for electrons in xenon [39]. The Q-value for $0\nu\beta\beta$ in ^{136}Xe is near the energy for a minimum ionizing particle, which allows nearly complete charge collection since the low ionization density reduces the recombination probability. This plot suggests Xe detectors will have the best energy resolution when collecting charge from ~ 1 MeV electrons.

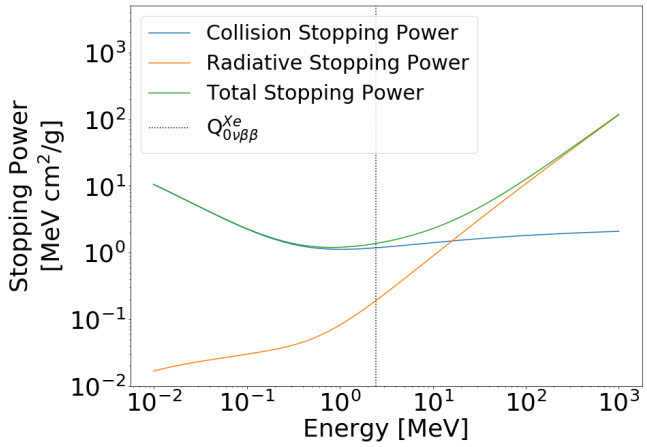

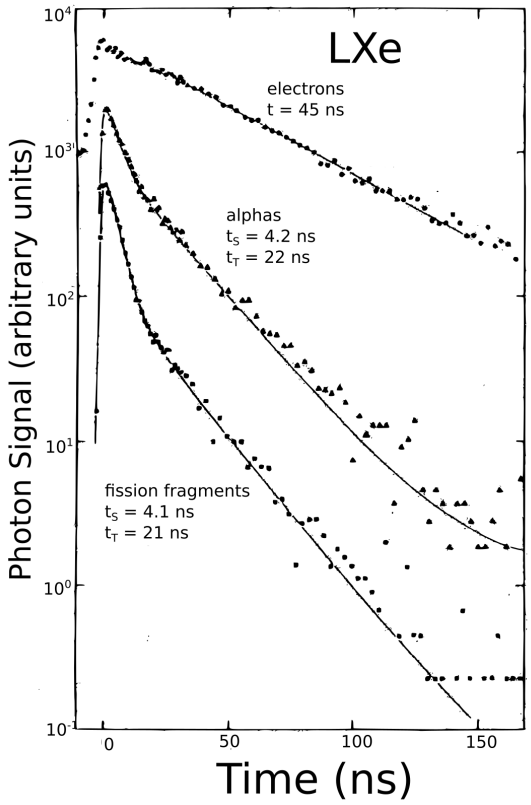

Figure 2-2: Scintillation yield for ionizing particles in LXe with no drift field. The long decay time for the scintillation signal from electrons is due to the low ionization density, which results in a low rate of recombination. The short decay time for alphas and fission fragments can be accounted for by the large linear energy transfer for these particles, which not only increases the ionization density, but their nuclear recoils transfer enough energy to access the triplet and singlet state of the excited dimer Xe_2^*. Figure reproduced from [42].

2.3 Correlation Between Charge and Scintillation Yield in LXe

When acting as a calorimeter, energy deposited in LXe can be reconstructed through the light and charge yield. There are two dominant channels for light production in LXe, excitation (Xe^*) and ionization-recombination (Xe^+) [46]:

Xe^*:

$Xe^* + Xe \rightarrow Xe_2^*$

$Xe_2^* \rightarrow 2Xe + h\nu$, and

Xe^+:

$Xe^+ + Xe \rightarrow Xe_2^+$

$Xe_2^+ + e^- \rightarrow Xe^* + Xe + heat$

$Xe^* + Xe \rightarrow Xe_2^*$

$Xe_2^* \rightarrow 2Xe + h\nu$,

where both processes yield 175 nm scintillation photons [47]. Because the energy difference between the ground state (Xe) and the excited dimer (Xe_2^*) is so large, it is believed that the disassociative transition of the dimer will always result in the creation of a single UV photon [48]:

$$N_\gamma = N_{ex} + N_{rec}, \tag{24}$$

where N_γ, N_{ex}, and N_{rec} are the number of UV photons, excited xenon atoms, and recombined xenon ions, respectively. Since some photons are created through ionization-recombination, the number of free electrons is given by:

$$N_e = N_{ion} - N_{rec} = N_{ion}\,(1 - r)\,, \tag{25}$$

where N_{ion} is the number of xenon ions escaping recombination, and r is the recombination probability, N_{rec}/N_{ion}. Equations 24 and 25 give a relationship between the number of quanta and the number of energy deposition modes:

$$N_\gamma + N_e = N_{ion} + N_{ex} = N_{ion}\,(1 + \alpha)\,, \tag{26}$$

where $\alpha = N_{ex}/N_{ion}$. An immediate result is for the maximum number of photons:

$$N_{\gamma_o} = N_{ion}\,(1 + \alpha - \chi)\,, \tag{27}$$

where we can identify χ as the ratio of escaping electrons, $(1 - r)$, at zero field. When an electric field is applied across LXe, the free electrons are collected at the anode. The action of the electric field also inhibits recombination by drifting charge towards the electrodes, and in general, the recombination probability is inversely proportional to the field strength. We can identify a recombination probability of zero with an infinite electric field, yielding:

$$N_{e_o} = N_{ion} = \frac{N_\gamma + N_e}{1 + \alpha},\ \text{or} \tag{28}$$

$$N_\gamma = N_{ion}\,(1 + \alpha - N_e/N_{e_o})\,. \tag{29}$$

Given $Q = eN_e$ and $S = N_\gamma/a$, where e and a are conversion factors between the number of quanta and their yields, we have the following measurable relationship:

$$\frac{S}{S_o} = \frac{1 + \alpha - Q/Q_o}{1 + \alpha - \chi}; \tag{30}$$

a plot of this relationship for 662 keV gamma rays is shown in Figure 2-3. The last equation implies the electric field dependent equation:

$$C(E) = A\frac{Q(E)}{Q_o} + B\frac{S(E)}{S_o} = 1, \tag{31}$$

where $A = (1+\alpha)^{-1}$, and $B = 1 - \chi A$. This relationship holds so long as there is no scintillation quenching process, and the electric field is high enough to collect all the escaping electrons, χ, as shown in Figure 2-3. However, there exists a theoretical scintillation quenching process that breaks Equation 26, from which Equation 31 was derived:

$Xe^* + Xe^*$:

$Xe^* + Xe^* \rightarrow Xe + Xe^+ + e^-$,

where the excess energy, $\sim E_{ex}$, is carried away by the electron, and thermalized before recombination or collection. The quenching process is more likely to occur with higher excitation density, and so for relativistic heavy ions in LXe, $C(E) < 1$, but for MIPs, $C(E) \approx 1$. The effect of scintillation quenching has not been experimentally verified for LXe, but the same theoretical mechanism for scintillation quenching exists for LAr, which has been verified [49]; Figure 2-4 shows $C(E)$ for different linear energy transfers (LET). It therefore follows that for MIPs in LXe, under electric fields of sufficient strength to collect escaping electrons, there exists an anticorrelation between scintillation and charge yield, according to Equation 31.

When measuring the ionization and scintillation yield in LXe, the energy resolution can thus be improved with higher drift fields [34] since charge collection is more effective than light collection; the correlation between ionization resolution and field strength for 570 keV γs in LXe is shown in Figure 2-5. In addition, since the number of electrons collected is related to the number of photons, the fluctuations in electron and photon number must also depend on each other. The correlated fluctuations between charge and light yield in

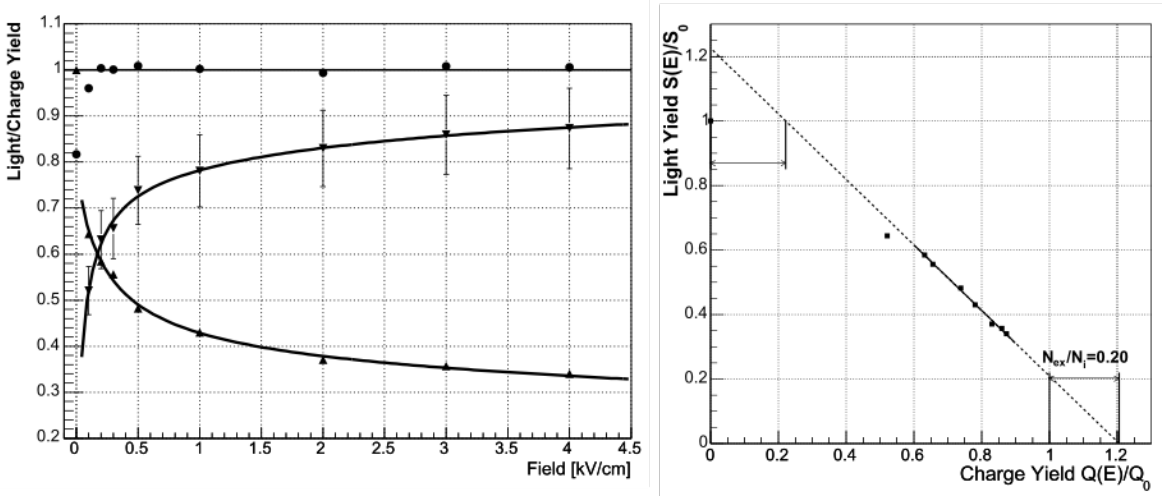

Figure 2-3: Measurements of the charge and light yield for ionization and excitation under a drift field in LXe. Left: the total yield of charge and light yield sums to 1, since recombined ions always result in the emission of a 178 nm photon. At low drift field the total yield < 1 since some of the escaping electrons (χ) cannot reach the anode within the trigger window. Right: measurements confirming Equation 30, the relative scintillation yield (S/S_o) as a function of relative charge yield (Q/Q_o). Figure reproduced from [50].

LXe were first reported by E. Conti et al. [45]. An observation of the anticorrelation in fluctuations using the state of the art EXO-200 detector is shown in Figure 2-6 [24]. An attractive feature of this correlation is that an improved energy resolution is possible when using a rotated energy, $\theta \sim \tan^{-1}(E_{scint}/E_{ion})$. Thus the best energy resolution in LXe can be achieved when exploiting the correlated fluctuations at high drift field, as is shown in Figure 2-5.

2.4 EXO-200

The EXO-200 detector is a single phase LXe TPC, which was located at the waste-isolation pilot-plant (WIPP), in Carlsbad, New Mexico. The laboratory at WIPP is $\sim$ 660 m underground, which provides an overburden of 1624 meters of water equivalent (m.w.e) [51]. Although the underground lab at WIPP provides a modest amount of overburden, the mine is excavated from the Salado salt formation, so the amount of U/Th radionuclides surrounding the lab is greatly reduced. The EXO-200 detector is within a class 1000 clean room within

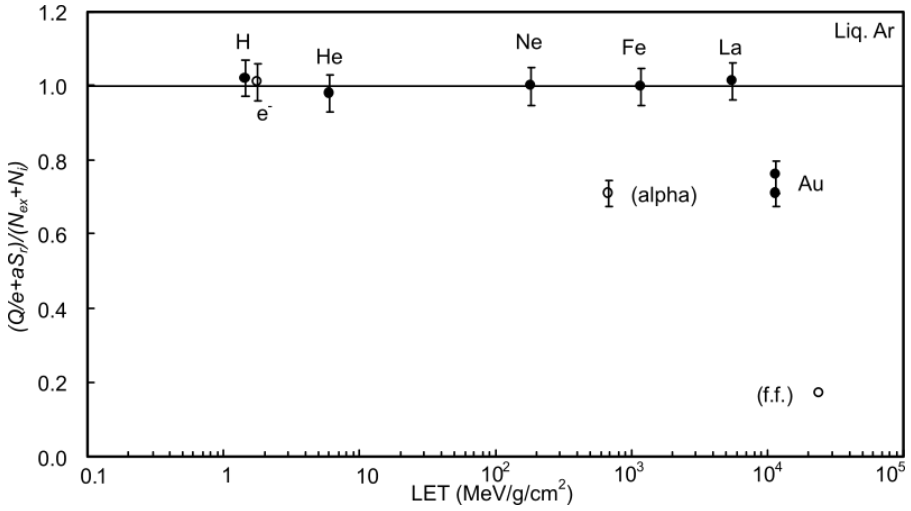

Figure 2-4: The ratio of the total quanta yield to the total ionization and excitation, with respect to linear energy transfer (LET) for LAr. In the absence of a scintillation quenching process, the ratio should be 1 because of the recombination scheme outlined in Equations 2.3 and 2.3. When the LET is high, the excitation density is also high enough that the scintillation quenching process has sufficient probability to attenuate the total quanta yield (< 1). In theory, the same quenching process is possible for LXe, although it has not been observed in an experiment. Figure reproduced from [49].

Figure 2-5: The effect of drift field on the energy resolution for LXe: as the drift field increases, the number of electrons collected at the anode also increases, providing a better energy resolution. The rotated energy resolution (σ_{min}) is an improvement over the charge resolution (σ_e) alone, since it accounts for the correlated fluctuations in charge and light yield. Figure reproduced from [45].

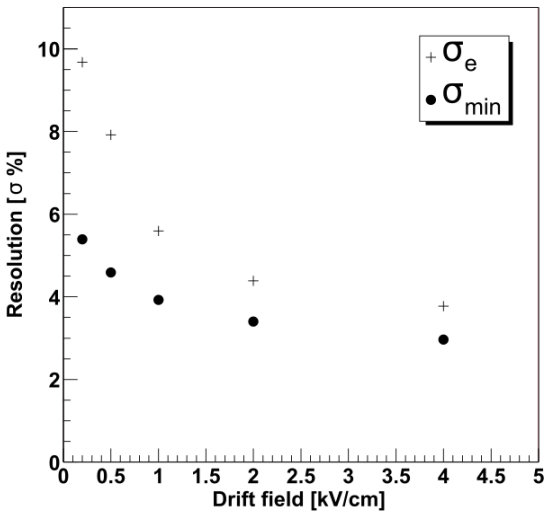

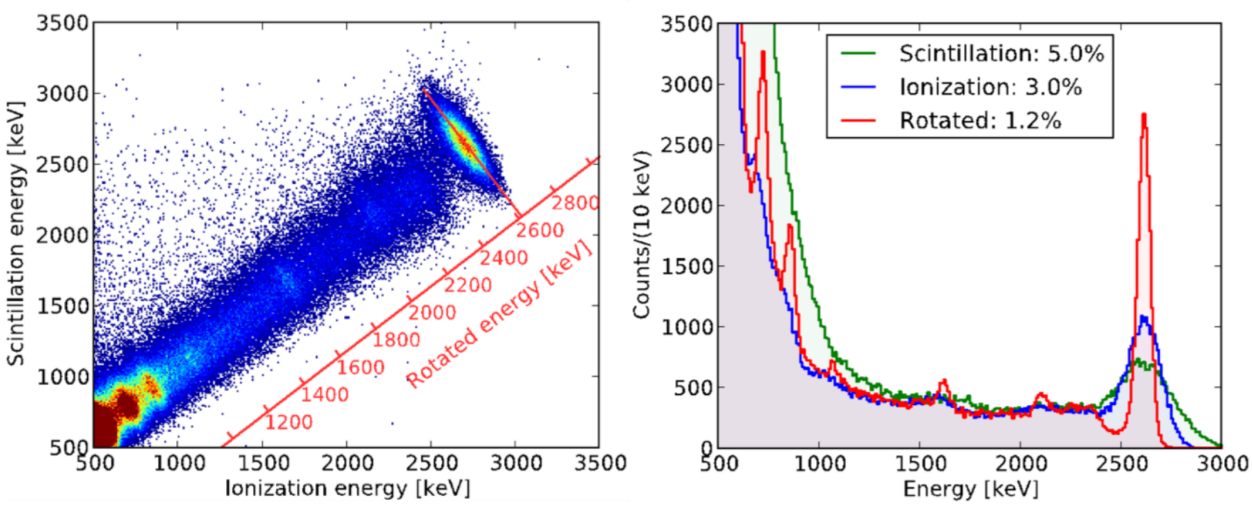

Figure 2-6: The scintillation and ionization spectra for energy deposition within LXe, using a ^{228}Th source. The ionization, scintillation, and rotated energy spectra are shown in the tile adjacent; it is clear that the rotated energy, $\theta \sim \tan^{-1}(E_{scint}/E_{ion})$, has an improved resolution when compared against the resolution of the ionization or scintillation signal by itself. Figure reproduced from [24].

a mine drift. External to the clean room is an array of plastic scintillators that provide an active muon veto. Inside the clean room, the cryostat is surrounded by low-radioactivity lead blocks for passive shielding. Within the cryostat, the TPC is immersed in an HFE-7000 bath that acts as additional passive shielding, and moderates the temperature of the detector. The TPC has an active mass of $\sim$ 110 kg of LXe. A diagram of the EXO-200 system is shown in Figure 2-7.

Phase-I of operations ran from September 2011 to January 2014, when they were halted following a fire, and a release of radioactive isotopes at the WIPP facility (both unrelated to EXO-200). While the WIPP facility was closed, several upgrades to the EXO-200 detector were planned, which included improvements to the electronics readout, and a radon suppression system. In April 2016, Phase-II of operations resumed with the upgraded EXO-200 detector until end of running in December 2018, resulting in a total livetime of 1181.3 days.

The EXO-200 detector is a right-angle cylindrical TPC, utilizing a common cathode to split the TPC vertically into two 'twin' TPCs. The common cathode is held at high voltage, and two anode wire planes at each end of the TPC are held at virtual ground. The wire

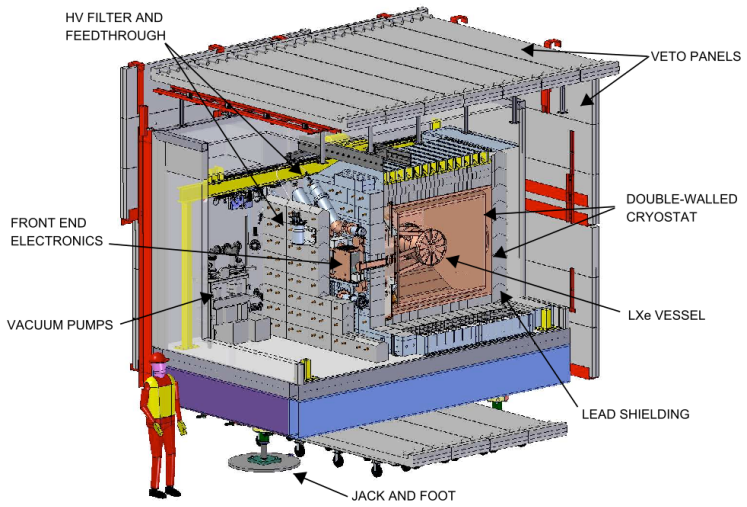

Figure 2-7: The EXO-200 system: the class 1000 clean room containing the detector is located within a salt drift $\sim$ 660 m underground at WIPP. The TPC vessel is immersed in an HFE-7000 bath for passive shielding and temperature regulation. The cryostat is further shielded using lead bricks, and scintillator panels line the Conex at the top and sides for an active muon veto. Figure reproduced from [52].

planes at each end consist of a charge collection (U) wire plane, and an induction (V) wire plane 6 mm in front of the U-plane, where the V wire plane is biased electrically in such a way that electrons pass through it; the U and V wire planes are oriented 60° towards each other. A field shaping cage is graded in ten stages from the cathode to anode to ensure a uniform drift field. Planes of large-area avalanche photo-diodes (LAAPDs) for light collection are located 6 mm behind both U wire planes. LAAPDs were chosen instead of the more conventional photomultiplier tubes because of their low radioactivity, small size, and high quantum efficiency at 175 nm. A more complete description of the EXO-200 detector can be found in [52], and a diagram of the EXO-200 detector is shown in Figure 2-8.

When a high-energy event occurs within the EXO-200 TPC, the LXe is ionized and excited as described in Section 2.3. The light is collected almost immediately ($\sim$ ns), whereas the charge is collected after drifting to the U wire plane ($\sim$ μs). The relative orientation between the U and V wire planes allows 2D event reconstruction using the induced signals on the V wires. Knowing the relevant field parameters, the time difference between the light and charge collection allows the event location to be reconstructed along the cylindrical axis; these two methods can be combined to give a full 3D event location within the TPC. 3D event reconstruction is necessary to ensure the event was located within the fiducial volume

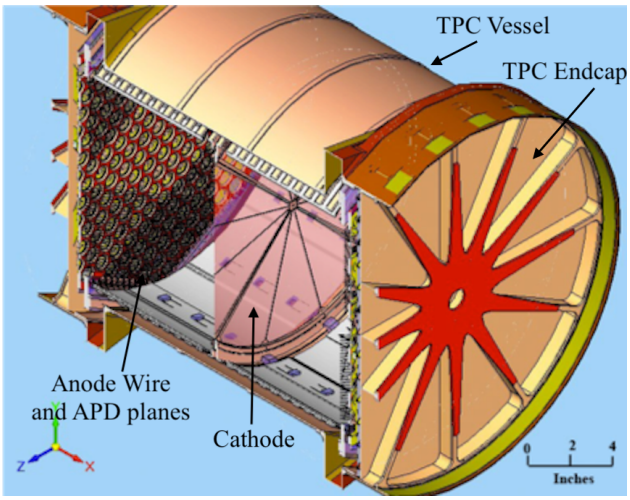

Figure 2-8: The EXO-200 detector. The common cathode separates the TPC in two 'twin' TPCs. The field shaping rings are used to ensure a uniform electric field from the cathode to the anode wire plane; the LAAPD plane is located behind the anode wire plane. Figure reproduced from [24].

of the detector, and to separate single-site from multi-site events; γs at the $0\nu\beta\beta$ Q-value deposit energy dominantly in multi-site events though Compton scatters, whereas βs deposit energy in single-site events through local collisions. The charge and light measurements are then combined, exploiting the correlated fluctuations between charge and light yield, to reconstruct the energy of the event.

Following the completion of the EXO-200 experiment, an analysis searching for $0\nu\beta\beta$ in ^{136}Xe using the full EXO-200 data set was performed. Given the exposure of 234.1 kg $\cdot$ yr, and the approximate background contribution of 0.13 $[\frac{\text{cts}}{\text{FWHM}\cdot\text{kg}\cdot\text{yr}}]$, there should be ~ 60 background events[5] at $Q_{0\nu\beta\beta} \pm 2\sigma$. The best fit to the background data for single site events in the ROI revealed an excess of ~ 7 events for Phase I, and a deficit of ~ 5 events for Phase II, indicating no statistically significant evidence for $0\nu\beta\beta$ in ^{136}Xe, thus leading to a new lower limit on the $0\nu\beta\beta$ half-life, $3.5 \cdot 10^{25}$ yr at the 90% confidence level [34]. A plot of the EXO-200 physics data and the best fit to the background model for Phase I and II is shown in Figure 2-9.

[5]The exact background contribution is 32.3 ± 2.3 events for Phase I, and 30.9 ± 2.4 events for Phase II, at $Q_{0\nu\beta\beta} \pm 2\sigma$ [34]

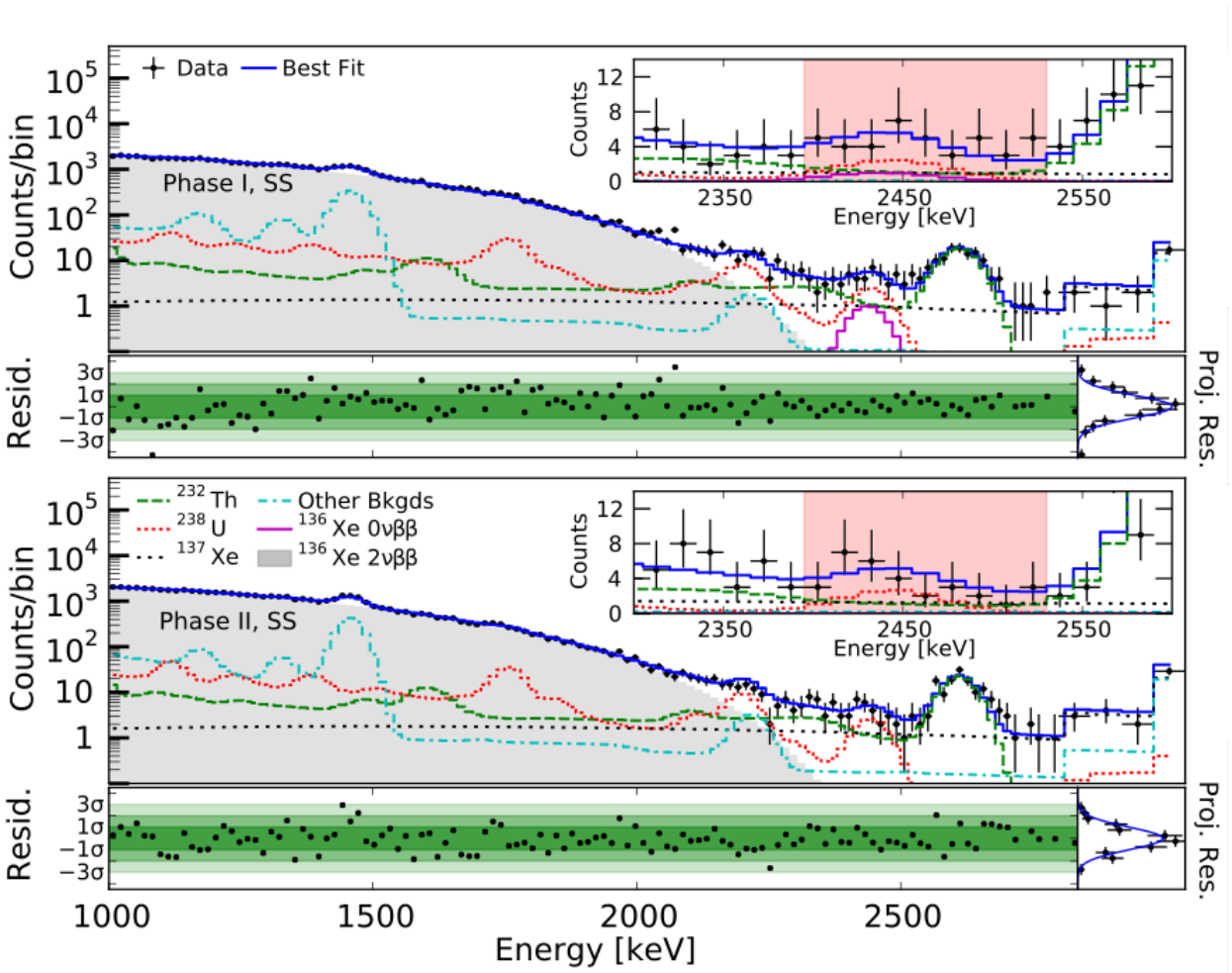

Figure 2-9: Best fit of the background model to the EXO-200 physics data. The single site spectrum for Phase I and II are shown in the top and bottom plots, respectively; the inlays are zoomed to the ROI. The best fit residuals follow a normal distribution, with small deviations accounted for in the systematics. The energy bins are 15 keV below 2800 keV, and 30 keV above 2800 keV. Figure reproduced from [34].

2.5 nEXO

The EXO-200 analysis technique demonstrated that the correlated fluctuations for charge and light yield could be used to reconstruct the energy of events with 1.15% energy resolution; it was also shown that event topology could be reconstructed, which allowed discrimination between βs and γs, and that the events occur within the fiducial volume. During the development of the EXO-200 detector, the nEXO collaboration formed to begin R&D on a tonne scale LXe TPC.

The nEXO detector is based on the successful EXO-200 concept. The TPC has an active mass of 5 tonnes of LXe, enriched to 90% in the isotope ^{136}Xe. Similar to EXO-200, the cryostat is filled with HFE-7000, which acts as additional passive shielding, and as a temperature regulator for the detector. The nEXO cryostat is located within a vacuum insulated sphere that is submerged in purified water, which attenuates the majority of the environmental radiation. The containing structure for the purified water is a water tank with an OD of 10 m and height of 9 m. The tank is instrumented with PMTs that are read out as Cherenkov detectors, providing an active muon veto. nEXO is anticipated to be housed at SNOLAB, in Sudbury, Ontario. The facilities at SNOLAB are $\sim$ 2070 m underground, which provides an overburden of $\sim$ 6010 m.w.e. SNOLAB is located in the active Creighton nickel mine, which is operated by Vale Canada Limited. Because of the geology in the mine, significant passive shielding is necessary to block radiation backgrounds from the decay chains of the naturally occurring ^{232}Th and ^{238}U in the surrounding rock. A diagram of the nEXO detector system is shown in Figure 2-10.

Similar to EXO-200, nEXO is a right-angled cylindrical TPC that reads out light and charge signals simultaneously. However, there are a number of key upgrades the nEXO detector makes over its predecessor. Some of these items are addressed in the text below, and a complete description can be found in [24].

nEXO will have a significantly lower background contribution at $Q\pm2\sigma$ than EXO-200 since it is being built as a monolithic detector: when scaling up the size of the detector,

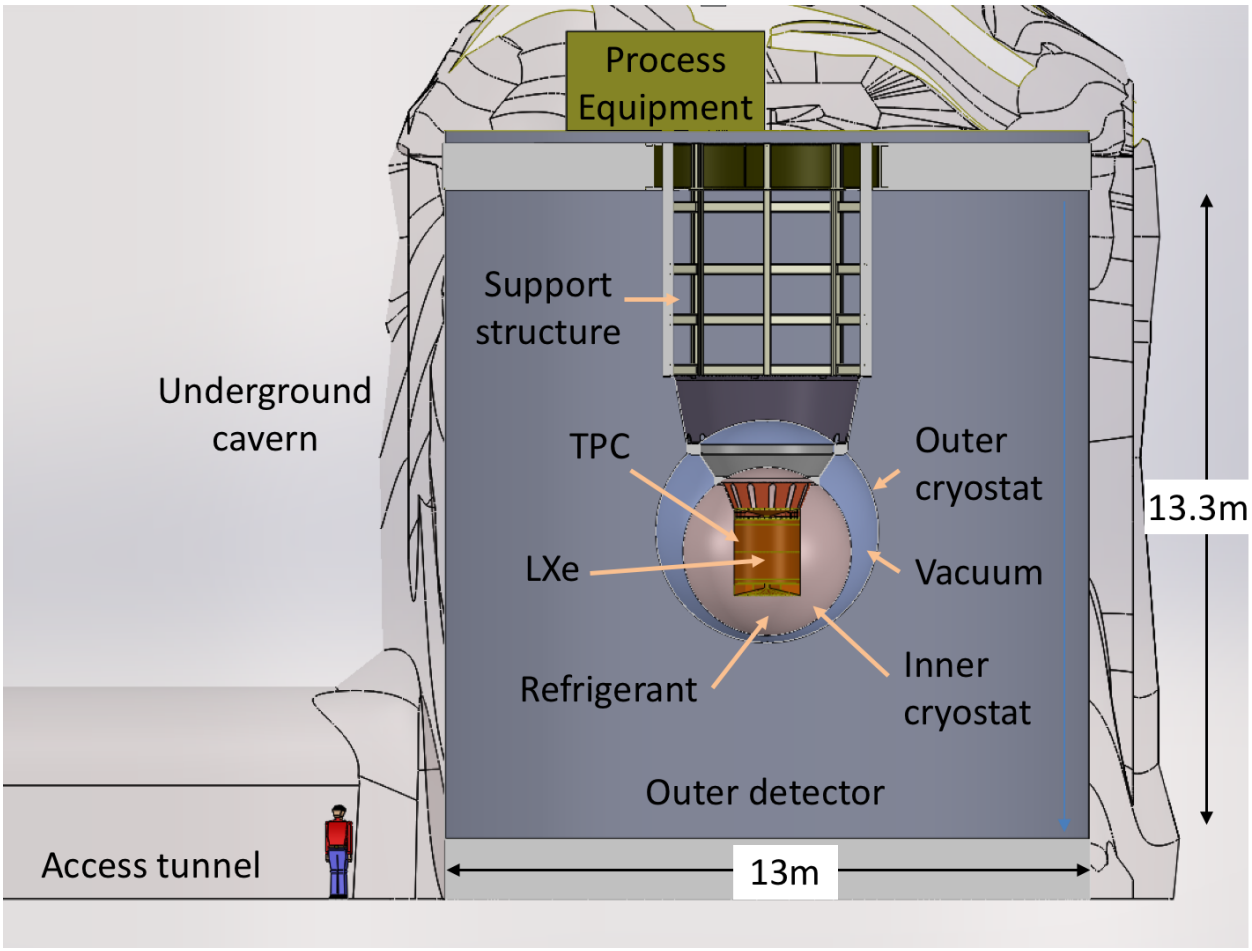

Figure 2-10: A preliminary design of the nEXO detector system, housed in the cryopit, at SNOLAB. The nEXO cryostat is contained within a vacuum insulated sphere, which is immersed in a tank of purified water. There are access drifts at the base of the water tank, and above; see text for a more complete description of the system. Figure reproduced from [24].

the fiducial volume grows faster than the shielding volume. The projected background for nEXO is $\sim 10^{-4}$ $[\frac{\text{cts}}{\text{FWHM}\cdot\text{kg}\cdot\text{yr}}]$ at $Q\pm 2\sigma$ [41], nearly three orders of magnitude less than EXO-200. nEXO also utilizes a single drift volume, maximizing the volume of LXe where external backgrounds are the lowest, and ensuring that the Rn decay daughters, which can drift and accumulate on the electrodes, are as far as possible from the inner most volume. As a consequence, for the same drift field the HV requirements are a factor two greater than for a common cathode TPC; for a drift field of 400 V/cm, the potential on the cathode must be $\approx$ -50 kV. The baseline HV system uses a 125 μm thin, slightly tensioned cathode, and 58 field shaping rings 4 mm in height and at a 20 mm pitch. The longer drift volume in nEXO also increases electron diffusion, and the capture probability by electronegative impurities within the LXe. To mitigate the capture by electronegative impurities, nEXO will substantially reduce the amount of plastics within the TPC, which are believed to outgas a significant amount of impurities. The concentration of impurities should also decrease, since the volume to surface area of the TPC increases by $\sim 3\times$ relative to EXO-200. Given the average electron lifetime $\tau_e \sim 3$ ms for Phase II of EXO-200, and the improvements made by nEXO listed above, a ~ 10 ms lifetime should be achievable for nEXO [24].

The baseline charge collection system in nEXO uses an array of tiles using a dielectric material [24]. Each tile is composed of X and Y channel strips, laid out orthogonaly using square pads of Au and Ti deposited onto a silica wafer; the pads are joined at the corners using a thin strip of metal that is insulated with a 1.5 μm thick SiO_2 dielectric. A diagram of the X/Y channel strips and a picture of a prototype charge collection tile are shown in Figure 2-11 [53]. There are several factors which motivate the departure from the stereo wire configuration that was used in EXO-200. Thermal cycling poses a greater risk of failure to wires under tension than to tiles, and if a failure does occur, then a system of modular tiles with on-board front end electronics mitigates the impact of dead channels. In-situ digitization reduces the number of cables and feedthroughs, and eliminates EM noise pickup along analog transmission lines. If the stereo wire system from EXO-200 was used, there

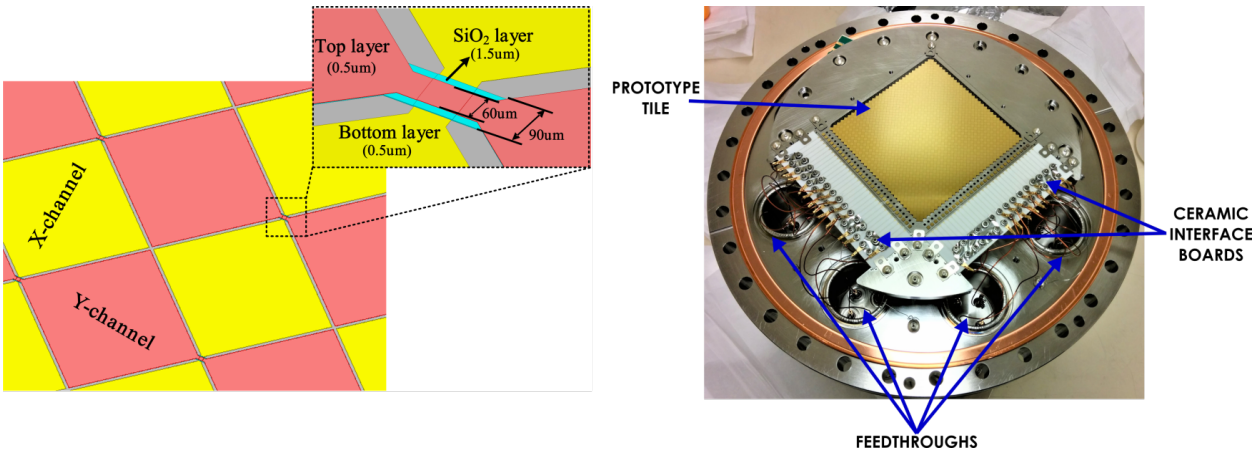

Figure 2-11: The proposed dielectric tile system for charge collection in nEXO. Left: the layout scheme of dielectric pads, joined at the corner to form orthogonal X and Y strips; each pad is insulated with a thin deposition of SiO_2. Right: a prototype charge collection tile, developed at Stanford for the nEXO collaboration. Figure reproduced from [53].

would be a large force on the TPC end cap introduced from the tensioned wires. The TPC end cap would require more rigidity to compensate for these forces, which would increase the mass of the detector vessel. Although the vessel is made from low activity copper, it is the largest background contribution for nEXO, and therefore minimizing the mass of the copper vessel is a priority. A drawback to the tile system is that induction signals are measured as the electrons drift towards the anode, and thus the integrated charge readout includes both the collected charge and induced charge; in EXO-200 two wires planes were used: the first to record the induced signals, and the second to collect the charge; the first wire plane blocks induction on the collection plane.

Silicon photomultipliers (SiPMs) have been identified as the devices to detect the vacuum ultraviolet scintillation light for nEXO [24]. Similar to the charge collection scheme, the SiPMs will be integrated into modular tiles with on-board front-end electronics. The tiles are grouped into long rectangular staves that cover the walls of the TPC, behind the field shaping rings. A SiPM tile and a computer image cutaway of the TPC, revealing the photodetector mounting concept, are shown in Figure 2-12. When considering devices for light detection in nEXO, PMTs are excluded outright due to radioactivity requirements; LAAPDs, as used in EXO-200, have a high capacitance, leading to high noise. The signal noise generated by

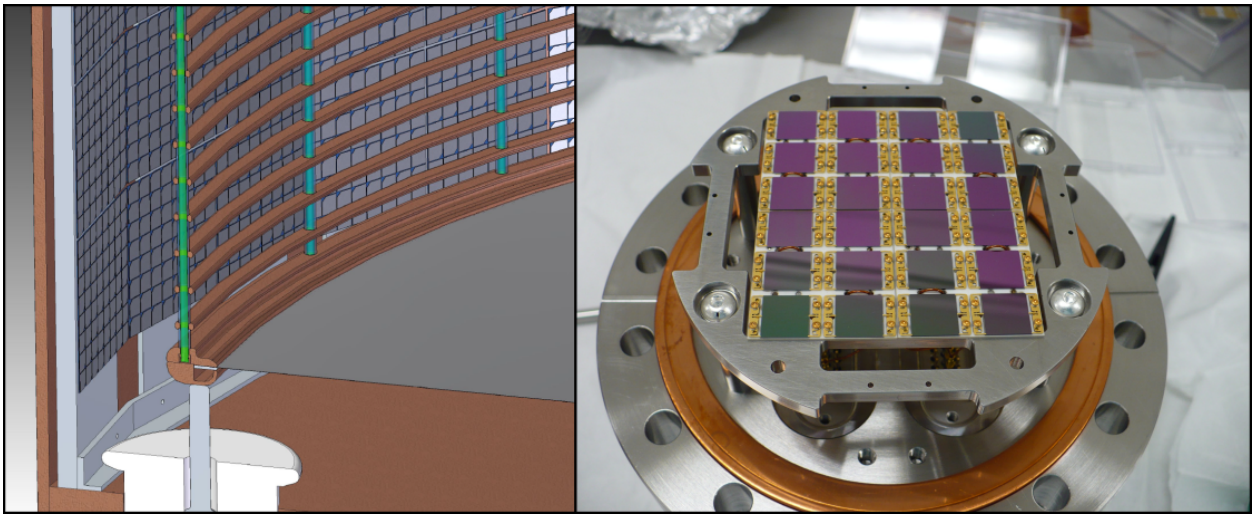

Figure 2-12: The light collection scheme for nEXO. SiPMs are integrated into 10×10 cm^2 tiles, which are then arranged into staves. Left: a cutaway of the nEXO TPC, showing staves mounted on the walls of the TPC vessel, behind the field shaping rings. Right: a preliminary 4×6 cm^2 SiPM tile, developed at Stanford, used to study in-LXe performance after integration. Figure reproduced from [24].

LAAPDs increases the effect of fluctuations, which in turn degrades the energy resolution of the detector. The circular geometry of LAAPDs also results in loose packing, reducing the total photocoverage area [54]. Recent developments in SiPM technology have made them suitable for detection of VUV light, with a quantum efficiency of $\sim$ 20%. Although LAAPDs have much higher quantum efficiency in LXe to VUV photons ($\sim$ 100%), the low noise, radioactivity, and high photocoverage area of SiPMs motivates their choice as the devices for light detection in nEXO.

3 Environmental Test Stand

3.1 Overview

SiPMs are silicon devices of up to 1 cm^2 in area with single photon sensitivity, and have a quantum efficiency of $\sim$ 15% at 175 nm. nEXO will use tiles of SiPMs, $\sim$ 10×10 cm^2, organized into staves, which will have a photo-coverage area of $\sim$ 4.5 m^2. The development of integrated tiles with front-end electronic 'on-board' is advanced within the collaboration, so precision testing of these tiles in conditions similar to their deployment is necessary. These requirements motivate the creation of an environmental test (ETS) stand for measuring $\sim$ 150 cm^2 of SiPMs at 168 K with quick turnaround between tile deployment, facilitating both a high-rate of baseline SiPM characterization, and precision testing of integrated tiles. To design the ETS, a thermal network model (TNM) was developed for a broad parameter optimization, followed by finite element analysis (FEA) using the COMSOL package [55]. The design, assembly, and commissioning of the ETS is documented in this chapter.

The primary design goal of the setup is to simulate the temperature environment of liquid xenon (LXe) and liquid argon (LAr), with stability < 1 K, for the testing of silicon photomultipliers (SiPMs) after they have been integrated into tiles. The secondary design goals are to achieve fast cool-down, < 10 h, and low power consumption, < 1 W, driving stable operation. Using a thermal-network model, a broad optimization is used to inform the general design. The broad optimization is achievable since the steady-state problem is reduced to a algebraic equation and the transient problem to a first-order differential equation; it is shown below that the thermal network model is equivalent to the heat equation in the continuum limit. Given the general design, a series of finite-element simulations are performed using COMSOL, solving the heat equation, to optimize specific configurations, design parameters, and to characterize the setup.

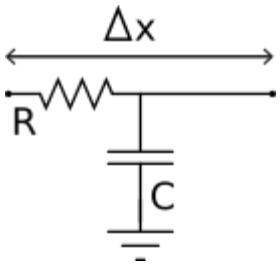

Figure 3-1: An elementary piece of a thermal network: the thermal element (TE). In limit when Δx goes to zero, the thermal element represents an infinitesimal piece of some macroscopic media, and is characterized by the heat equation.

3.2 Thermal Network Model

The heat equation [56] is used to study heat transmission in macroscopic media, but analytic solutions are challenging for complicated geometries. Further, when considering the heat equation, it is difficult to garner intuition about how each subsystem within the larger heat system behaves. However, there is a one-to-one correspondence between Ohm's law and Fourier's law, and electrical and thermal capacitance: this suggests that thermal resistors and capacitors can be connected to form thermal networks. An elementary piece of the thermal network, referred to as a thermal element (TE), is a resistor connected to a grounded capacitor and output terminal in parallel, as shown in Figure 3-1. The motivation for this choice is to reproduce the heat equation in the continuum limit. Suppose the TE had length Δx and was positioned at x_0. Then for $R = \frac{\Delta x}{kA}$ and $C = c\rho A\Delta x$ we have

$$T(x_0 + \Delta x) = T(x_0) - \left(\frac{\Delta x}{kA}\right)\dot{Q}(x_0) \tag{32}$$

$$\dot{Q}(x_0 + \Delta x) = \dot{Q}(x_0) - (c\rho A\Delta x)\frac{\partial T}{\partial t}, \tag{33}$$

where T is the temperature, Q is the heat, k is the thermal conductivity, c is the specific heat, ρ is the density, and A is the cross-sectional area. Equations 32 and 33 imply

$$\lim_{\Delta x \to\ 0} \frac{T(x_0 + \Delta x) - T(x_0)}{\Delta x} = \frac{\partial T}{\partial x} = -\frac{1}{kA}\dot{Q}, \quad \text{and} \tag{34}$$

$$\lim_{\Delta x \to\ 0} \frac{\dot{Q}(x_0 + \Delta x) - \dot{Q}(x_0)}{\Delta x} = \frac{\partial \dot{Q}}{\partial x} = -c\rho A\frac{\partial T}{\partial t}, \tag{35}$$

which can be combined by taking the x-derivative of Equation 34 and substituting Equation 35 to form the heat equation:

$$\frac{\partial^2 T}{\partial x^2} = -\frac{1}{kA}\frac{\partial \dot{Q}}{\partial x} = \frac{1}{\alpha}\frac{\partial T}{\partial t}, \tag{36}$$

where $\alpha = k/\rho c$. This result allows the construction of a thermal network to describe heat transmission in continuous media. An elementary example would be heat conducted along a thin rod: by daisy chaining TEs together, the rod can be constructed by requiring $L = n\Delta x$, where L is the length of the rod, and n is the number of TEs; here the continuum limit is characterized by $\lim_{n\to\infty}$ and $\lim_{\Delta x \to\ 0}$ such that L remains fixed. This method can be generalized to any geometry so long as

$$|\hat{x} \cdot \dot{\mathbf{Q}}| = 1 \Leftrightarrow |\hat{x} \cdot \nabla T| = 1, \quad \text{and} \tag{37}$$

$$|\hat{n} \cdot \dot{\mathbf{Q}}| = 0 \Leftrightarrow |\hat{n} \cdot \nabla T| = 0. \tag{38}$$

Figure 3-2 shows the thermal network for a thin rod, with boundary conditions imposed by an ideal temperature source. There are a features of note for this model: if the boundary conditions are constant, then the power across each capacitor goes to zero at steady state, i.e., $\lim_{t\to\infty} \dot{Q}_i^C = 0$. Under these conditions the thermal network reduces to a series resistor

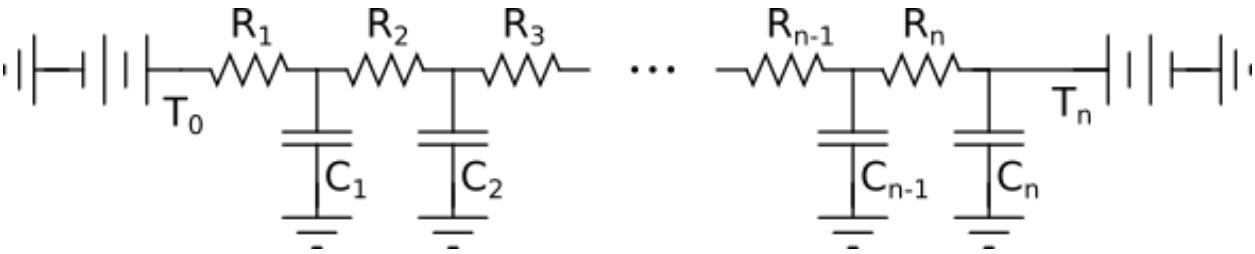

Figure 3-2: A thermal network describing heat propagation through some macroscopic media. Boundary conditions are imposed using an ideal temperature source (battery). This model can be expanded to include a radiative load by including an ideal current source at each node. In certain conditions described in the text, the thermal network reduces to a single resistor, or capacitor.

with equivalent resistance $R_{eq} = \Delta x \sum R_i$, and the network can be described using an algebraic equation; if the media is homogeneous and the geometric factor $\Delta x/A$ is constant, then $R = L/kA$. If the capacity of the media is sufficiently small, then the internal heat changes negligibly with temperature, and the system can be approximated by a single resistor with $R_{eq} = \Delta x \sum R_i$, as in steady-state. Similarly, if the resistance of the media is sufficiently small, then the change in temperature across each resistor is negligible, which can be approximated by $R_i = 0$, and the system reduces to a single capacitor with $C_{eq} = \Delta x \sum C_i$. The latter two features can motivate better conceptual design for thermal systems since it allows the introduction of elements commonly used in electrical engineering, such as filters, dividers, attenuators, and switches. The fact that at steady-state, the system can be reduced to a network of resistors allows a broad range of parameters to be optimized in a manner that would be computationally expensive and laborious with FEA, e.g., the number, length, and cross-section of standoffs can be varied with a few lines in a computer script, effectively yielding the results from thousands of design iterations in under a second of computation time - with FEA, the same parameters can be varied through computer scripts[6], but each simulation can take minutes under the best conditions[7], which scales the total computation time for thousands of iterations to days.

[6]This is generally true, but requires advanced knowledge of the CAD tools, and careful design to avoid invalid bodies.

[7]The best conditions would be fast meshing without failures, and fast simulations with converging residuals.

3.3 Conceptual Design

The general design concept is to construct a temperature divider between a cold dewar ($\sim$ 77 K) and the warm environment ($\sim$ 293 K), with a switch that can short-circuit the cold-side of the divider; the dewar is filled with liquid nitrogen (LIN) as an open cycle refrigerant, as shown in Figure 3-3. Each resistor in the divider is constructed using a series of concentric rings that are connected by three radially symmetric standoffs; the relative orientation of the standoffs are shifted by 60° degree for each connected ring. This arrangement allows fine tuning of the total resistance (R1+R2) and the divider resistance (R2/[R1+R2]) through the geometry and materials used for each component. A secondary motivation for the ring/standoff arrangement is that the capacity of the rings is much greater than the standoffs, and the resistance of the standoffs is much greater than the rings. In the context of the TNM, this arrangement can be approximated by a resistor for the standoffs, and a capacitor for the rings. Therefore each ring/standoff sub-assembly acts similarly to a low pass filter, so each divider is a daisy-chain of low pass filters. This inhibits the propagation of temperature/power variations from the environment/dewar to the SiPM top-plate. The setup is made compact by nesting the cold-side of the divider within the hot-side, and similarly nesting the LIN dewar within both. The cold-side and hot-side resistors are referred to as inner and outer resistors, respectively. LIN has a high latent heat, so in practical applications, its temperature is nearly uniform and at the boiling point: 77.35 K at 1 atm [57]. This property allows the dewar to be represented by an ideal temperature source with ΔT = 77.35 K. The vacuum chamber exchanges heat with its surrounding via free convection, and if the power delivered to the dewar is sufficiently low (large resistance), its temperature will remain in equilibrium with the room. Under these conditions the flange connected to the divider can be treated as an ideal temperature source[8] with $\Delta T \sim$ 300 K. To ensure temperature stability, the total resistance is made large, however, this also increases the time

[8]Simulations using free convection models showed that the vacuum chamber would remain at room temperature, but the flanges that are thermally connected to the cryostat are $\sim$ 5 K below room temperature. This boundary condition was used for the later calculations.

for cooldown. To mitigate the increased cooldown time, a cold-finger is fixed in place at the top of the dewar using a thin disk. If the resistance of the disk is made large enough, only a small amount of power is transmitted through the cold-finger; if the LIN level is raised so that the cold-finger is submerged, then power bypasses both the thin disk and the cold half of the temperature divider. This process of power bypass acts as a switch that is controlled by the fill level. The resistance of each divider is chosen to passively control the temperature at the top-plate: during regular operation, the steady-state temperature should be 165 K (LXe [57]); when the cold-finger is engaged, the temperature should be $\sim$ 87 K (LAr [57]).

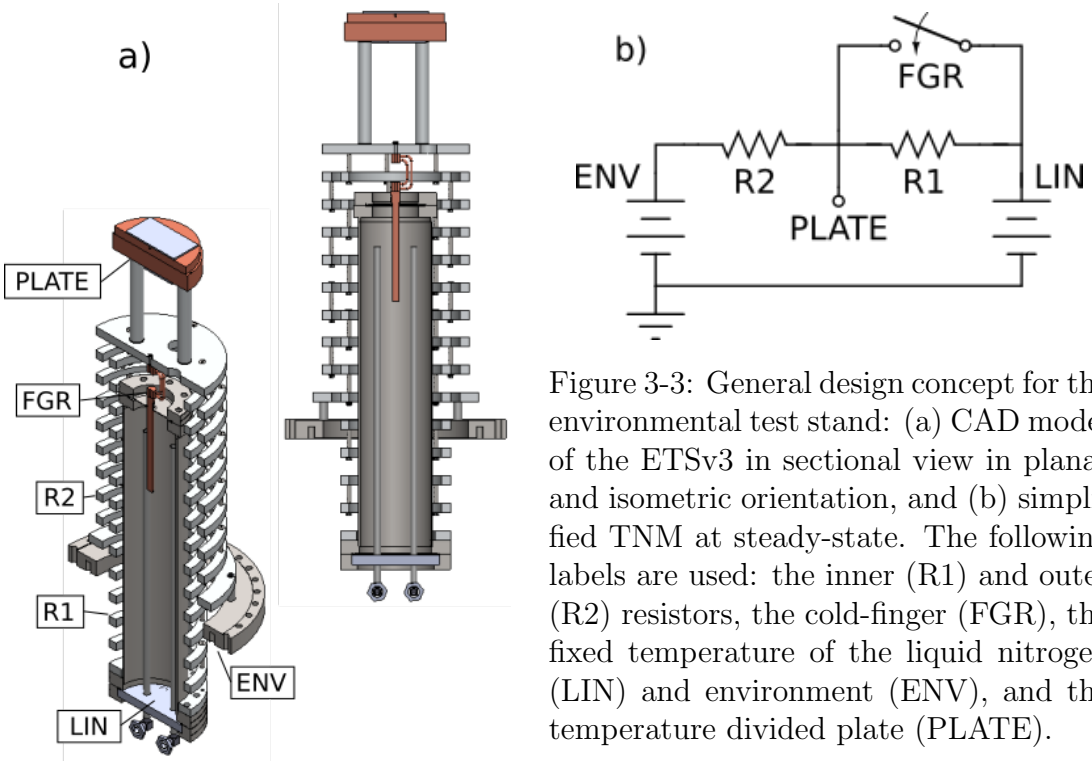

Figure 3-3: General design concept for the environmental test stand: (a) CAD model of the ETSv3 in sectional view in planar and isometric orientation, and (b) simplified TNM at steady-state. The following labels are used: the inner (R1) and outer (R2) resistors, the cold-finger (FGR), the fixed temperature of the liquid nitrogen (LIN) and environment (ENV), and the temperature divided plate (PLATE).

An expanded TNM with all loads and resistances is shown in Figure 3-4. The additional resistances considered for the cold-finger system are the cold-finger rod, the insulating disk, the dewar walls, and the braid connecting the rod to the union plate. The top-plate is joined to the union plate with a stand where heaters are placed for fine temperature control. Three additional fixed loads that need consideration are the SiPM cabling, the LIN plumbing, and

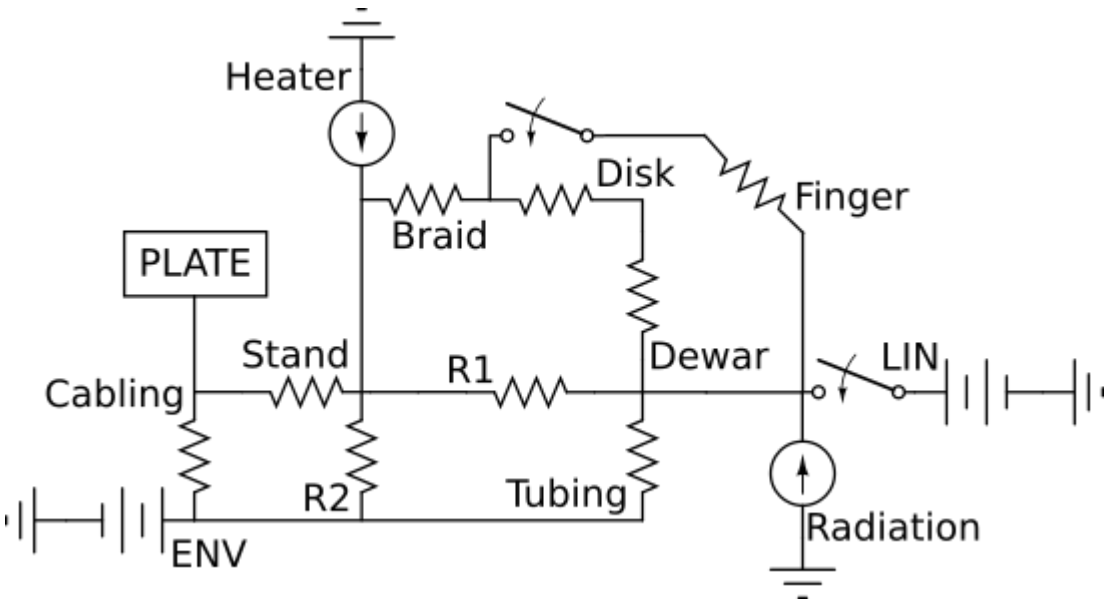

Figure 3-4: The steady-state expanded thermal network with anticipated loads - see text for descriptions.

the thermal radiation. Most of the radiated power is from the vacuum chamber, however the SiPM cabling, LIN tubing, and resistors can radiate heat to the LIN dewar. Most of the components in the expanded thermal network are tightly constrained, except for the values of the inner/outer divider resistances, R1 and R2. For a fixed temperature at the SiPM plate, the outer divider resistance can be found as a function of the inner divider resistance; Figure 3-5 shows a plot of this function for four isotherms, neglecting radiation. For a cold top-plate ($\sim$ 120 K) with a large absolute resistance, the outer divider should have a resistance $\sim 2\times$ as large as the inner divider resistance. There have been several design iterations to the ETS; Table 3-2 summarizes the different models. A comparison between the TNM and COMSOL for the ETSv1 model is shown in Table 3-3; the larger difference for the Outer Rings between COMSOL and the TNM is due to approximations made in the TNM for the conductive path along the flat-head screws with nuts and washers; with a simpler geometry the difference falls $< 1\%$.

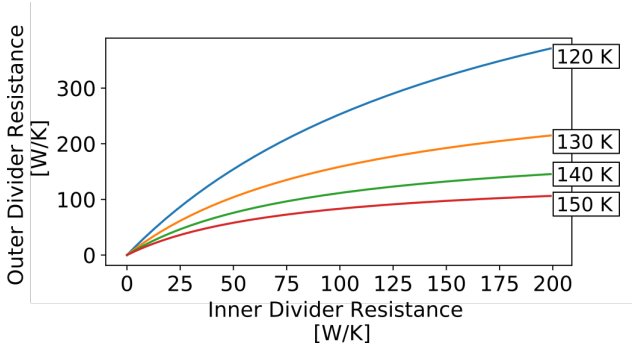

Figure 3-5: The relationship between the hot- and cold-side divider resistance for several steady-state isotherms at the SiPM plate. The relationship is generated using the expanded thermal network with constrained resistances as the input parameters.

Model	SiPM Cabling	Standoffs Outer, Inner	Cold-Finger Insulation
ETSv1	64-channel ribbon cable	24-1/2", 15-1/2"	Macor
ETSv2	64-channel ribbon cable	18-1", 14-1"	Macor
ETSv3a	10-channel coaxial cable	10-1", 14-1"	SS
ETSv3b[†]	10-channel coaxial cable	10-1", 14-1"	SS

[†]The ETSv3b model uses Mylar multi-layer insulation for radiation shielding.

Table 3-2: The various iterations of the Environmental Test Stand. The 'Standoffs' column can be read (number of standoff sections)-(standoff length).

	COMSOL	TNM	Percent Difference
Temperature [K]			
SiPM Top-plate	152.06	152.68	0.41
Dewar Flange	79.39	79.61	0.28
Power [mW]			
Cold-Finger	299.82	304.69	1.60
LIN Supply/Return	310.87	310.80	0.023
SiPM Cabling	155.91	154.79	0.72
Outer Rings	344.96	315.82	9.22

Table 3-3: A comparison between COMSOL and the TNM for various parameters, using the ETSv1 model; see text for discussion of results.

3.4 COMSOL Simulations

With the geometry roughly set using the thermal-network model, finite-element simulations are performed using COMSOL multiphysics [55] to refine the setup with greater accuracy. These simulations are performed neglecting radiative and vacuum-conductive loads to focus on the thermal conduction throughout the cryostat while retaining computational efficiency. Two major operating constraints changed following the completion of these simulations, the amount of SiPM cabling and the number of rings in the outer resister, so the validity of the simulations is limited to the gross effects of cable length, standoff material, and cold-finger configurations that motivated the final design. After finalizing the cryostat design, a final set of simulations are performed to investigate the effects of radiation, with and without Mylar multi-layer insulation (MLI); gas-phase conduction is neglected because the cryostat is designed to operate in high-vacuum.

3.4.1 Parameter Characterization

The ETSv2 model is used in this section and differs slightly from what is shown in Figure 3-3 (ETSv3) because of changes to the vacuum chamber and SiPM cabling. The vacuum chamber is configured such that there are 18 outer rings, and the SiPMs are connected using a 64-channel unshielded ribbon cable. A Macor insulated cold-finger was also used for these simulations, but was found to leak at an unacceptable rate after thermocycling, and was replaced with thin stainless-steel for insulation.

The parameter characterization is broken up into three investigations: a broad sweep covering the different combinations of materials for each sub-system, and their configurations. The best candidates from the prior investigation are selected for a set of simulations to understand the relationship between the diameter of the cold-finger and the SiPM cable length. Again, the best candidates are selected for a final investigation that allows the standoff material to vary across the set of outer/inner rings.

There are three standoff materials considered in the broad sweep: Macor, stainless-steel,

and aluminum; all of the outer/inner rings use the same standoff material so that the different possible extremes for the divider resistances can be investigated. Mixing combinations of the three standoff materials between the outer/inner rings gives nine different standoff configurations.

The SiPM cable configuration has four arrangements, split into two subgroups: LIN attenuation and LXe attenuation. LIN attenuation is achieved by fixing three aluminum rods to the dewar that extend through holes in the divider top-plate, just under the SiPM top-plate; the cables would be clamped to a aluminum plate attached to the rods. LXe attenuation is achieved by clamping the SiPM cables to the bottom of the SiPM top-plate. A visualization of these configurations is shown in Figure 3-6.

The cold-finger can be installed with and without insulation, giving different steady state temperatures. Figure 3-7 details the results of this investigation, where no attenuation, LXe attenuation, LIN attenuation, and LIN/LXe attenuation are represented with green, yellow, red, and blue markers, respectively. Four configurations are selected for further study and are indicated by the red box, utilizing wires that are LXe attenuated, with an insulated cold-finger; these configurations were chosen since they produced a steady-state temperature at the top plate close to the the desired temperature, and use commonly available materials, i.e., aluminum and stainless-steel.

As may be expected, LIN attenuation, i.e., the red markers in Figure 3-7, effectively 'shorts-out' the divider system, giving the coldest values at the SiPM mounting-plate - this effect is most apparent in the Mc-XX configurations, where the resistance between the top-plate and environment is largest. Since the SiPM top-plate and mounting-plate has very low resistance, the temperature gap between 'no attenuation' and 'LXe attenuation' ($\sim$ 5 K) suggests that there will be local heating near the SiPMs if the cabling is not attenuated; the LXe attenuation scheme is therefore considered the best configuration. Although Macor is the best performing material for the outer standoffs, its performance is very close to stainless-steel; the ubiquity and strength of stainless-steel make it a more suitable choice

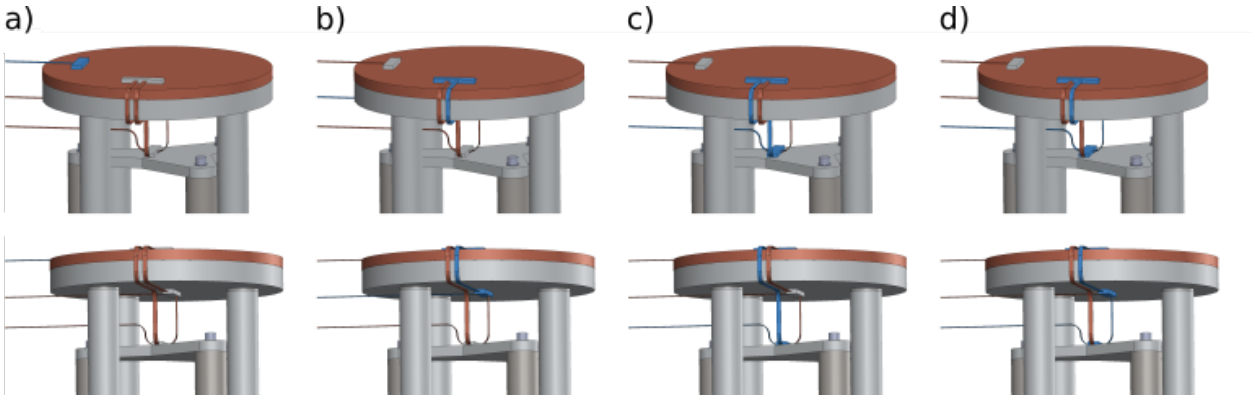

Figure 3-6: The various 'hot' and 'cold' cable configurations used in the broad parameter sweep; the cable layout is highlighted in blue. (a) no attenuation: the SiPM cabling is attached directly to the SiPMs. (b) LXe attenuation: the SiPM cable is clamped to the bottom of the SiPM top-plate, and then is connected to the SiPMs. (c) LIN attenuation: the SiPM cabling is clamped to a plate directly attached to the dewar, and then is connected to the SiPMs. (d) LIN/LXe attenuation: the SiPMs cabling is clamped to the dewar-plate, then to the bottom of the SiPM plate, then connected to the SiPMs.

than Macor, which has glass-like properties and would need custom machining. The SS-XX group is selected for further study; the Al-SS configuration is included for purely academic reasons as it displays a 'too-hot' bias. When no cold-finger insulation is used, the top-plate temperatures become nearly independent of the cold-finger activity; similar to LIN attenuation, this configuration effectively 'shorts-out' the divider system, and is therefore undesirable.

With the four selected configurations of standoff material and cable arrangement, the next set of COMSOL simulations are performed. The secondary sweep investigates the effect of cold-finger diameter and cable length. The cold-finger diameter is varied between 1/16 and 1/4 of an inch, and the cable length is varied between 5.67 and 22.68 inches; the seemingly arbitrary values for cable length are chosen since 5.67 inches is the minimum distance between the flange and top plate, and 22.68 is an integer multiple of 5.67, which facilitated a shortcut[9] in the simulation process. The length of the cold finger and area of the cabling is fixed, but Fourier's law allows the data generated from these simulations to

[9]Since the geometric factor in thermal resistance is $\Delta x/\mathrm{A}$, longer cable lengths can be investigated without creating CAD models with cable slack by using taut wires with a reduced cross section.

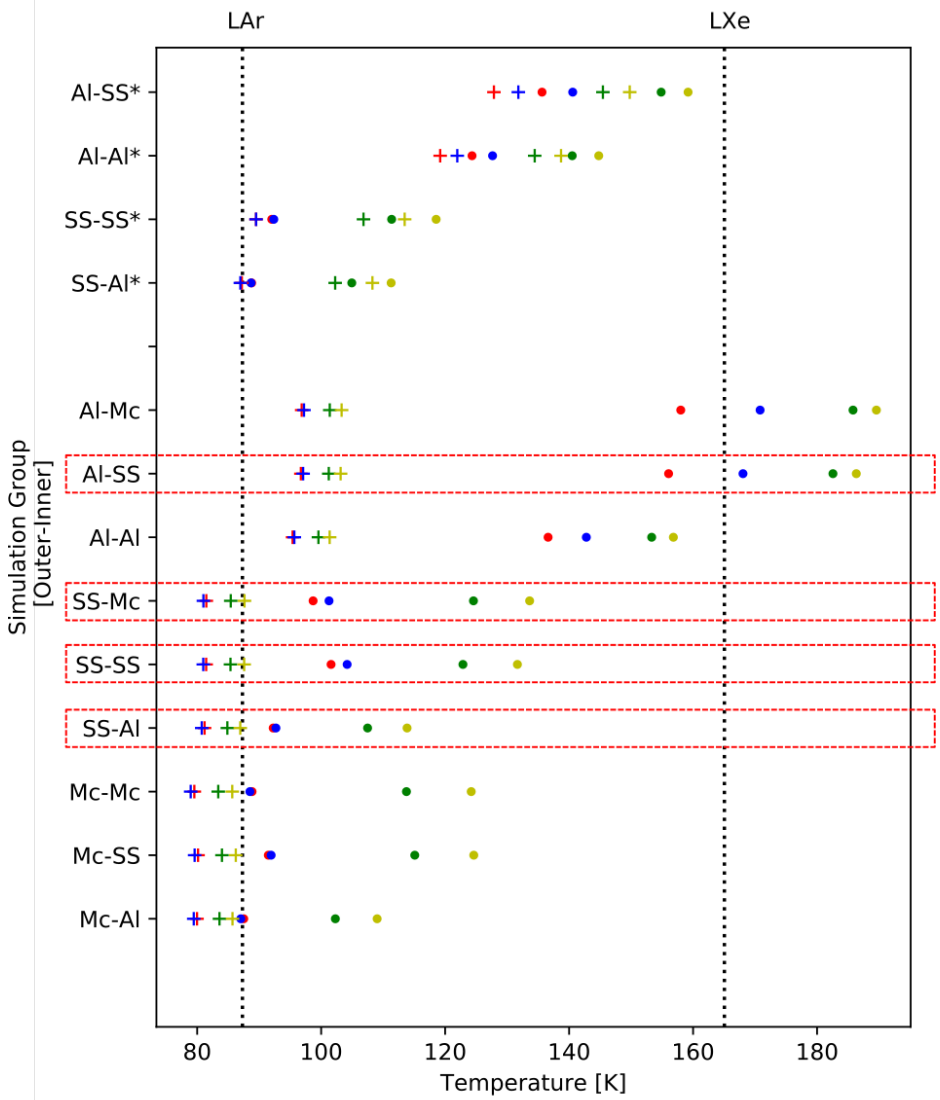

Figure 3-7: COMSOL broad sweep: an investigation into cable, standoff, and cold-finger configurations. The reported temperatures are the average value of the copper SiPM mounting-plate. Each row represents materials used for the standoffs composing the outer/inner rings. Within a row, each color represents a cable configuration: no attenuation (green), LXe attenuation (yellow), LIN attenuation (red), and LIN/LXe attenuation (blue). Like-colours within a row have the same configuration, however a cross is used if the cold-finger is active, and a circle if it is inactive. The top four rows marked with an asterisk indicate a cold-finger without insulation, and is only partially investigated. Suitable configurations will cluster about LAr/LXe temperatures for an active/inactive cold-finger; the temperatures should be below the targets as radiative loads are not considered, and more generally, since heat is easily added to a system, but not easily removed. The red box indicates configurations selected for further study.

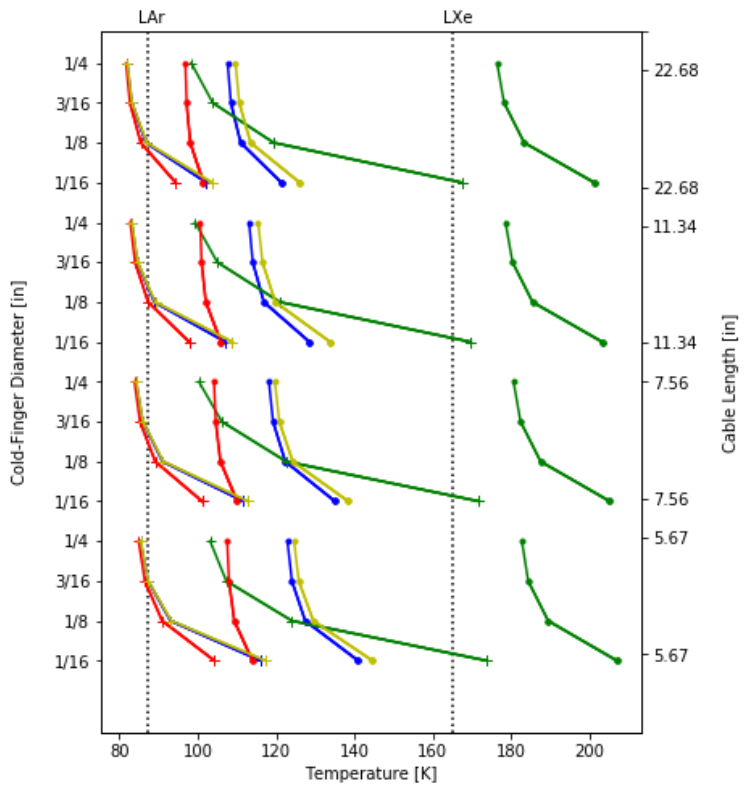

Figure 3-8: COMSOL narrow sweep: an investigation into cable length and cold-finger diameter for the hot-indirect cable configuration. The reported temperatures are the average value of the copper SiPM mounting-plate. The four standoff configurations for the outer-inner resistors are: SS-Mc (yellow), SS-SS (blue), SS-Al (red), Al-SS (green); as for Figure 3-7, a cross is used if the cold-finger is active, and a circle if it is inactive. As can be observed, the effect of increasing the diameter of the cold-finger on the SiPM stand reaches an asymptotic value at around 1/4 of an inch; the effect of increasing the SiPM cable length is small and approximately linear.

apply to other lengths/areas, provided the geometric factor $\Delta x/A$ remains constant. Figure 3-8 details the results of this investigation.

Varying the cold-finger diameter has an exponential effect, reaching an asymptotic value when the finger diameter is greater than 1/4 of an inch; varying the cable length has an approximately linear effect. As evident in the plots, Macor standoffs have little effect relative to stainless-steel, despite having about an order of magnitude lower thermal conductivity. This is an indication that the resistance of the standoffs, for Macor and stainless-steel, is large compared to the stainless-steel screws within the standoffs. In contrast to this relationship, the aluminum standoffs have a resistance comparable to the stainless-steel screws. This is due to the conductance of aluminum being about an order of magnitude greater than stainless-steel. Therefore an upper limit to the resistance of outer/inner standoffs is set by the stainless-steel screws, but the resistance can be reduced by using a conducting material. Therefore the ideal choice for standoffs is some combination of stainless-steel and aluminum.

Although different combinations of standoff material have been considered, they have

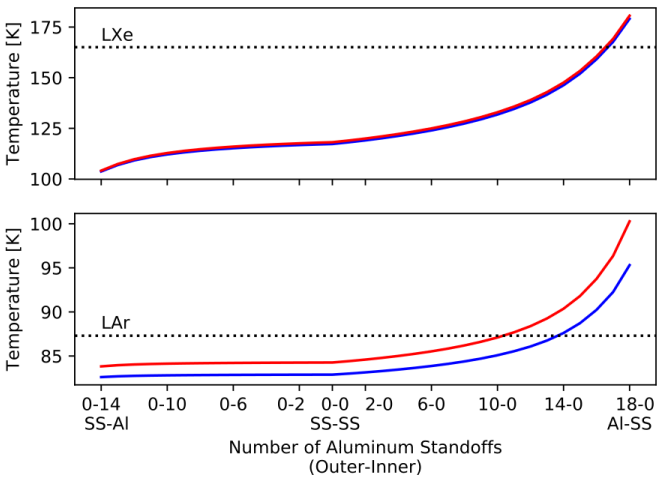

Figure 3-9: The SiPM mounting-plate temperature calculated for different combinations of standoff materials; there are 14 and 18 standoffs in the outer and inner rings, respectively. Each step changes the material for the three standoffs in the 'low-pass filter' sub-assembly, from the lowest sub-assembly up to the divider top-plate; the data points are connected by a line to help guide the eye. A SiPM cable length of 7.56 inches is used; a cold-finger diameter of 0.25 and 0.375 inches is indicated by the red and blue curves, respectively.

been homogeneous for the outer/inner rings. To better understand the effect of divider resistance on the SiPM mounting-plate temperature, the standoff materials are mixed for the outer/inner rings. The first arrangement considered is SS-Al, then for each inner 'low-pass filter' the three Al standoffs are swapped for SS, from the bottom up to the divider top-plate, until the arrangement is SS-SS. From here the SS standoffs for each outer 'low-pass filter' are swapped for Al in the same manner, until the arrangement is Al-SS. Figure 3-9 details the temperature of the SiPM stand when mixing different standoff materials for the outer/inner rings. The SiPM mounting-plate temperature is very sensitive to the resistance of the outer-divider, and less so to the inner-divider. The coldest temperature at the SiPM mounting-plate comes from the SS-Al arrangement, which is used in the final design.

3.4.2 Radiative Considerations

As mentioned previously, the number of outer rings and cable type has changed following the parameter characterization: the simulations in this section use the ETSv3 model. Fewer outer rings are used so that the top of vacuum chamber is at the same level as the optical table, enabling a simpler beam path for the later SiPM characterization. The 64-wire

unshielded ribbon cable is swapped for ten coaxial cables with a multiplexer. The coaxial shielding contributes a significant amount of copper, reducing the total resistance by an order of magnitude, despite having fewer cables. This change is compensated for by using a larger diameter cold-finger and heavier gauge cold-finger braid, which are described in a later section.

Four sets of steady-state simulations are performed for the finalized model: no surface-to-surface radiation, surface-to-surface radiation, surface-to-surface radiation with five layers of MLI, and surface-to-surface radiation with 15 layers of MLI, which are shown in Figures 3-10. The boundary conditions are set so that the vacuum chamber exchanges heat with the environment through natural convection and radiation with an ambient temperature of 293.15 K. There are four sections wrapped in MLI: the inside of the vacuum chamber, the outer rings, inner rings, and dewar. The effective emissivity from the MLI is approximated by imposing new emissivities at the boundaries for the dewar, inner rings, and outer rings.

Transient simulations were performed to estimate the cooldown time for the setup. Figure 3-11 shows a plot of the temperature at the SiPM top-plate from a transient simulation with radiation and no MLI. For the geometry of the ETS, transient simulations with radiation take several days to compute, and often crash midway through due to insufficient memory, leaving only partial simulation data. A generalised logistic function [58] has been used as a semi-empirical model to extrapolate crashed transient simulations, and is used later in the analysis to extrapolate real data. Figure 3-12 shows a generalised logistic function fitted to the first 4 h of the former transient simulation. The fit is then extrapolated for the entire duration of the simulation, so that the two may be compared. The fits are performed using the MINUIT2 solver under the ROOT data analysis package [59].

3.4.3 Thermodynamics

By calculating the steady-state temperature of each component, then integrating the temperature dependant capacitance from the initial conditions to final state, the total energy

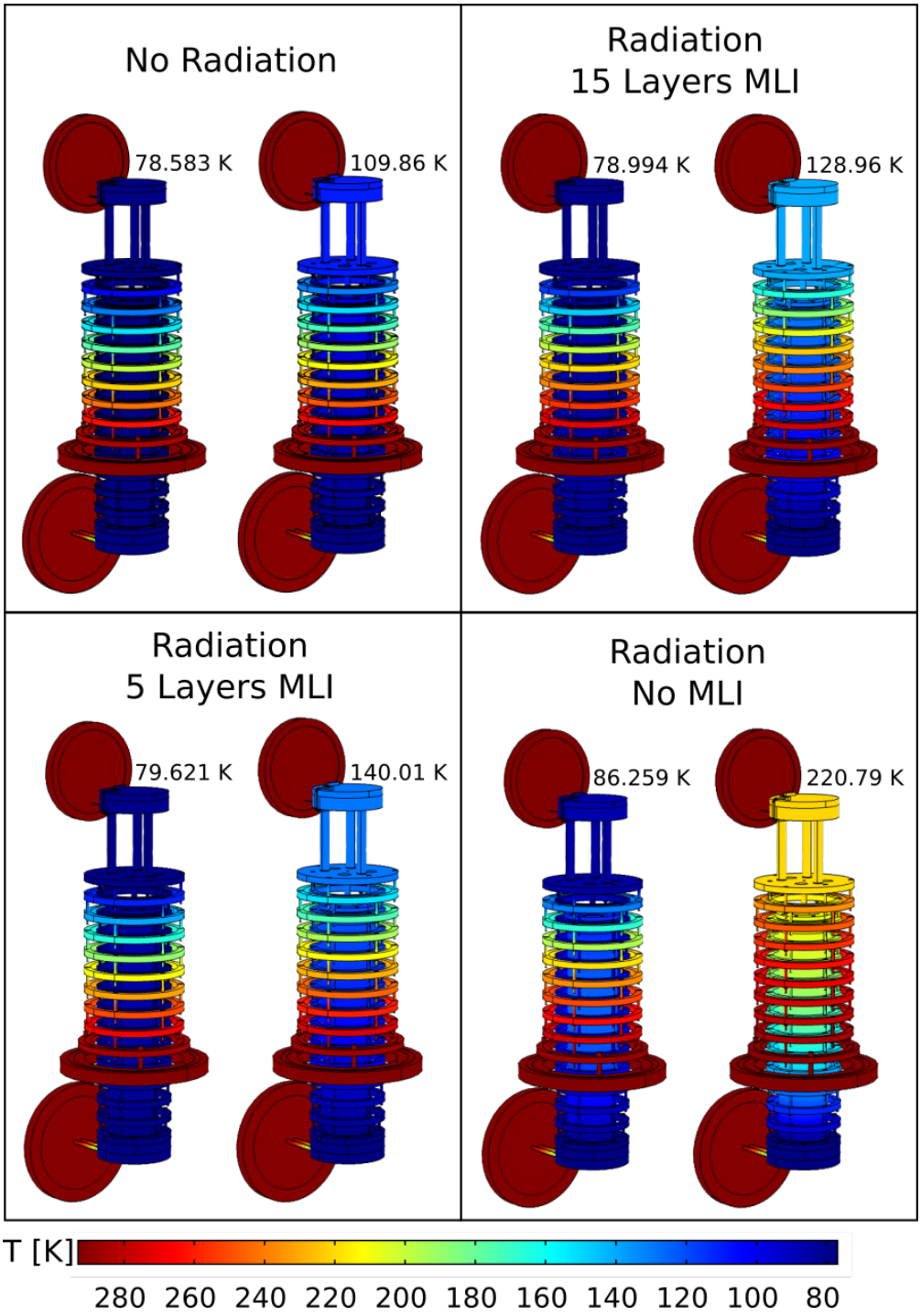

Figure 3-10: A heat map of the environmental test stand with and without surface-to-surface radiation. Each quadrant includes simulations with the cold-finger active (left) and inactive (right); the average temperature of the SiPM top-plate is included in the graphic. The vacuum chamber has been removed in post-processing so that the temperature distribution can be clearly seen.

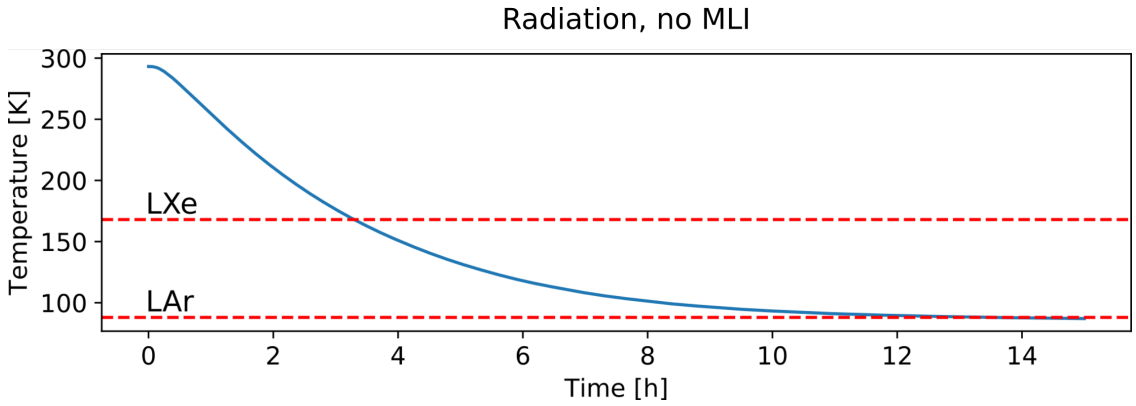

Figure 3-11: The temperature of the SiPM top-plate during a cooldown simulation. The simulation uses free convection across the vacuum chamber to dissipate heat, and includes surface-to-surface radiation between the vacuum chamber and the cryostat. The model uses no MLI, and the cold-finger is engaged.

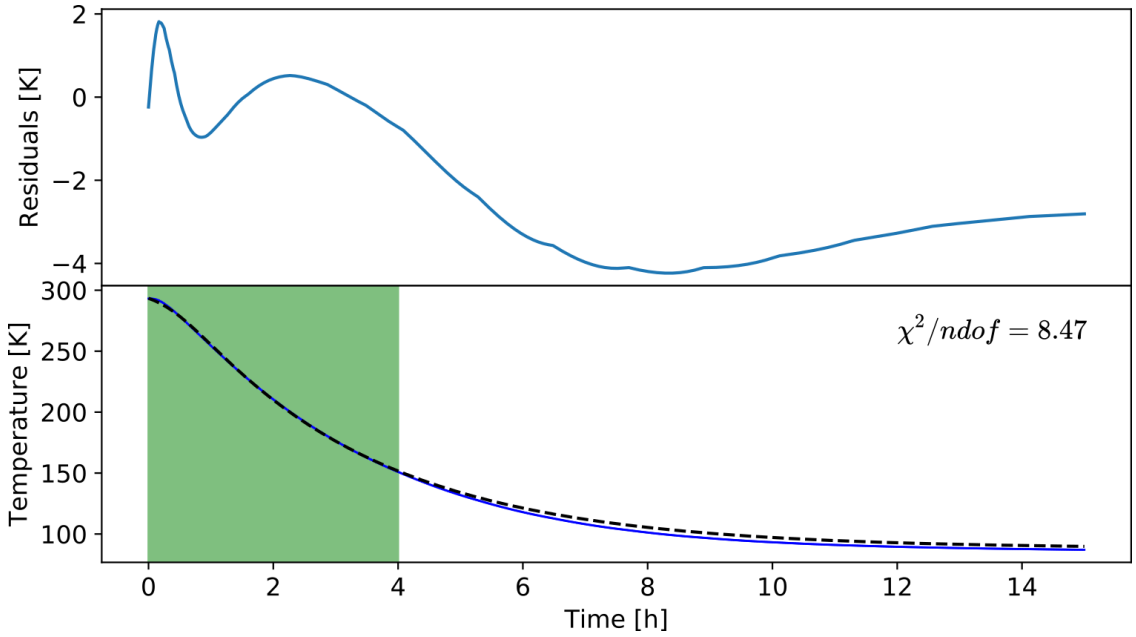

Figure 3-12: A plot of a generalised logistic function, fit to simulated data, as a test for extrapolation; the residuals for the fit are shown above. The simulated data set was truncated to 4 h (green region), then used as the input for the fit. The fit is extrapolated to the full length of the simulation. The extrapolation is marked by a dashed black line, and the simulation by a blue line. An autocorrelation, i.e., continuity, can be seen in the residuals, indicating a systematic difference between the logistic function extrapolation model and the simulated data; this difference is constrained < 5 K.

required for cooldown can be calculated; the estimated energy change for cooldown is $\sim$ -1.5 MJ, neglecting radiation. By calculating the power transmitted through each component that interacts with the environment (SiPM cabling, outer resistor, LIN tubing) at steady-state (TNM or COMSOL), the total power delivered to the LIN can be determined; the estimated power at steady-state is $\sim$ 1 W; the radiative load can be estimated by using the Stefan-Boltzmann law for the stainless-steel in line-of-sight with the cryostat; the total radiative load is $\sim$ 17 W. By wrapping the inner walls of the chamber, outer rings, inner rings, and dewar in MLI, an effective emissivity can be calculated using the Lockheed equation [60]: for N layers of a sheet with emissivity ϵ, the effective emissivity is N/ϵ. For $\sim$ 10 layers of MLI at each section, the total radiative load will be $<$ 1 W.

Using the latent heat of vaporization for LIN, $\sim$ 5600 J/mol [57], it can be estimated that $\sim$ -1 MJ of energy requires boiling $\sim$ 6 l of LIN. This suggests that reaching LXe temperatures will require boiling $\sim$ 9 l of LIN, and maintaining steady-state will require boiling $\sim$ 0.5 l of LIN per day, if a significant amount of MLI is used. Since the LIN dewar has a volume $\sim$ 14 l, cooldown will require one or two 'top-ups' so that the cold-finger remains engaged; the setup can remain cool for $\sim$ 1 1/2 weeks after the cold finger has been disengaged under our thermal load assumptions.

3.5 Apparatus

3.5.1 The Environmental Test Stand

All components are assembled using silver coated stainless-steel screws and bolts. Because the system undergoes thermal cycling, spring washers are used to mitigate thermal contraction/expansion. Vented washers or screws are used between all mating surfaces to prevent the slow outgassing of trapped air. All parts are cleaned with simple green, sonicated with acetone, then ethanol before assembly. The temperature divider is built using ten low-pass filters on the hot-side, and 14 low-pass filters on the cold-side (ETSv3). Each filter sub-assembly is composed of an aluminum ring, three 8-32 stainless-steel screws, and aluminum/stainless-

steel standoffs. The aluminum rings were cut from a 8" and a 6" OD 6061 aluminum tube, with wall thickness 0.5", and 0.5" height. Each ring was later turned on the lathe for a polished finish. The standoffs are stainless-steel on the hot-side, and aluminum on the cold-side, to bias the divided temperature towards colder values. Figure 3-13 shows the assembly process for the temperature divider and the dewar adapter. Because of the large surface area of environmental test stand and low resistance of the divider, radiative loads are larger than the conductive loads. This effect is mitigated by wrapping the dewar (15 layers), cold-side (5 layers), and hot-side (3 layers) of the divider in Mylar MLI. To reduce surface contact between layers, the Mylar sheets are crinkled, then wrapped around the components with some slack. Figure 3-14 shows the dewar/divider assemblies wrapped in MLI before being installed in the vacuum chamber.

The thermal switch assembly consists of two sub-assemblies: the cold-finger flange and high-power connector. To build the cold-finger flange, a 4-1/2" blank 316L stainless-steel CF-flange was precision machined into a custom 'nipple' feedthrough with 0.040" wall thickness. A C101 copper rod was precision machined to a radius 0.004" smaller than the CF-flange nipple; a ridge is machined into both components so that the copper rod can rest atop the nipple, forming a butt-lap joint. The two components are brazed together using Sil-Fos (Ag5%Cu89%P6%) brazing alloy[10]. Figure 3-15 shows drawings and photographs of the cold-finger flange. The high-power connector is built using a 00 AWG copper grounding braid for transmission and 1" OD 101 copper disks as connectors: the middle of the grounding braid is clamped between two disks using stainless-steel screws. Each end of the copper braid is connected to the circumference of a third copper disk using a high-torque stainless-steel pipe clamp. These two ends act as connectors and are coupled to the cold-finger and divider top-plate using 8-32 screws. Figure 3-16 shows the high-power connector sub-assembly, and Figure 3-17 shows the complete thermal switch assembly fixed to the dewar.

The bottom cross of the vacuum chamber is mounted on a large aluminum plate, tapped

[10]Blue Demon welding products.

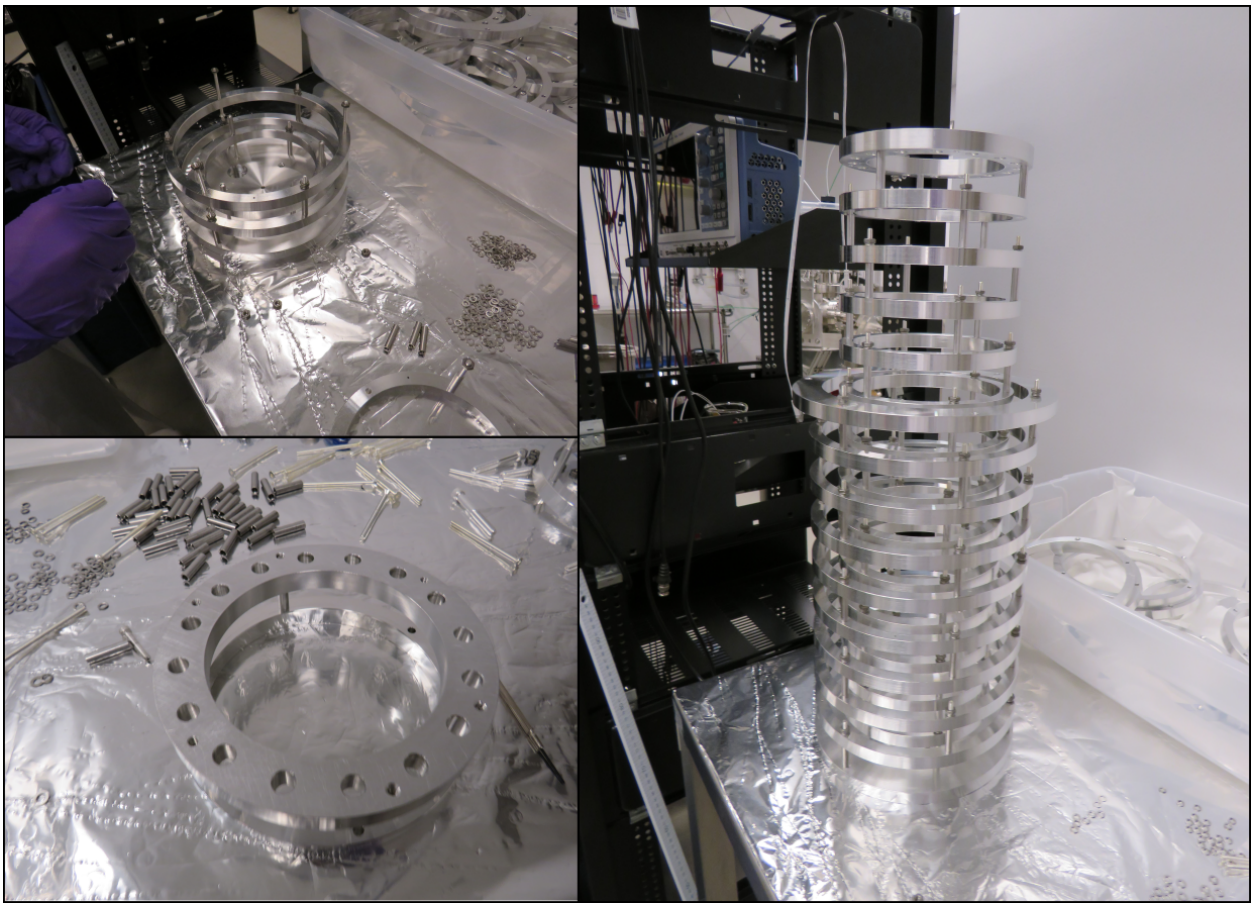

Figure 3-13: The assembly of the temperature divider resistors, without MLI. The top left picture shows the assembly of the temperature divider; the bottom left picture shows the adapter for the inner rings and the dewar; the right picture shows the assembled temperature divider. The outer and inner rings can be detached from the divider top-plate without a full disassembly. The assembly area was covered with aluminum foil, then wiped with acetone and ethanol.

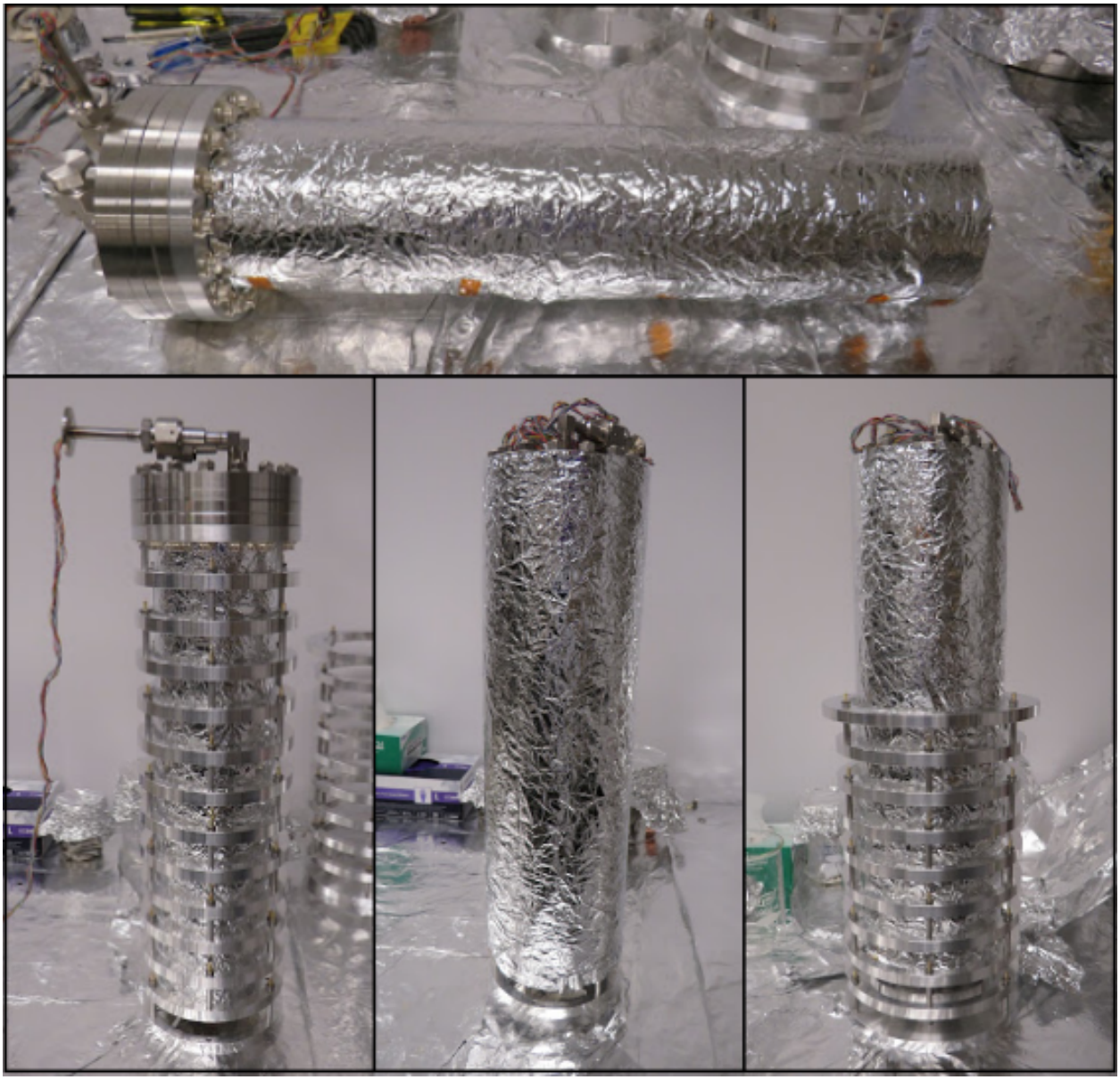

Figure 3-14: The assembly of the temperature divider, with MLI. The top picture shows the dewar and inner ring adapter wrapped in 15 layers of MLI. The bottom pictures show the progressive assembly after adding the inner rings, MLI, then the outer rings.

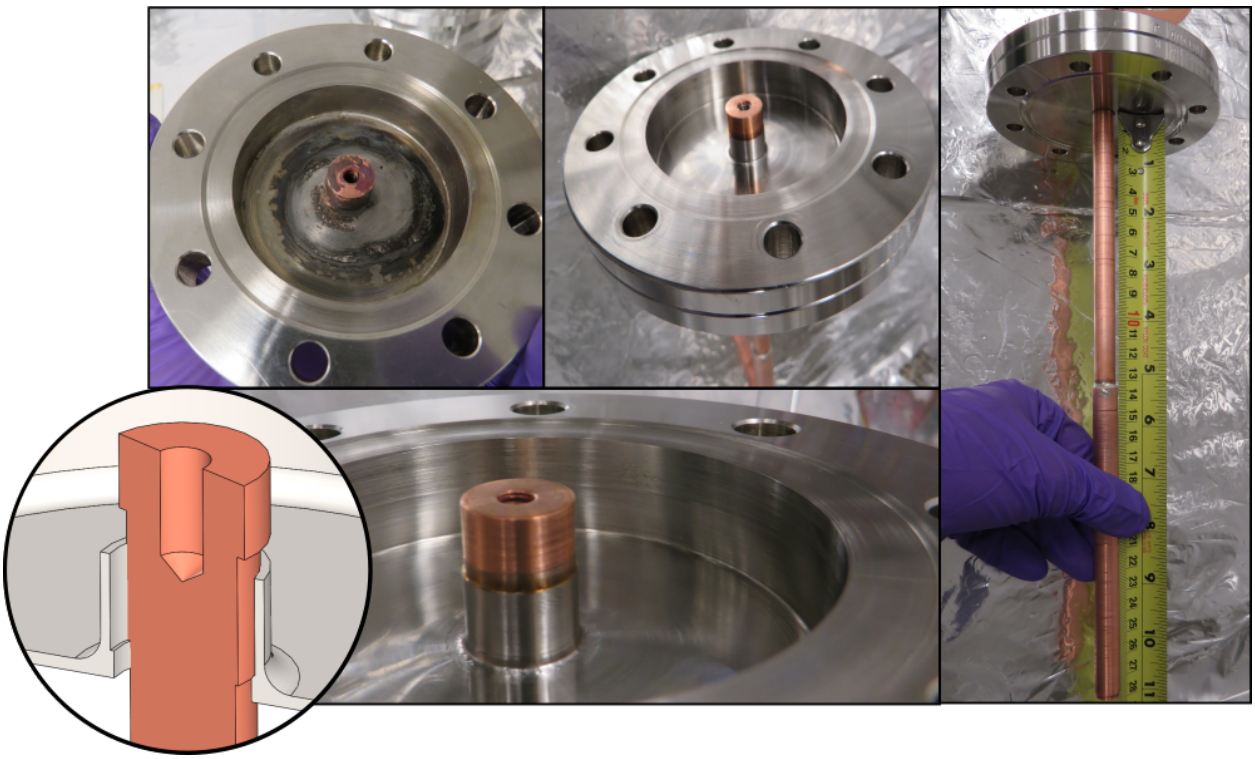

Figure 3-15: The cold-finger flange sub-assembly. The panels in the top-left/middle show the sub-assembly after brazing and post-brazing machining. The panel on the right shows the cold-finger flange and rod on the dewar-side. The bottom panel shows a close up of the brazed joint, and a CAD section-view of the joint geometry - the lap-joint has a width of 0.004" and the butt-joint has a width of 0.100". The top of the cold-finger is tapped with a stainless-steel helicoil for an 8-32 screw. The joint area was roughened with a steel file, then all parts were cleaned with simple green, sonicated with acetone, then ethanol, before brazing.

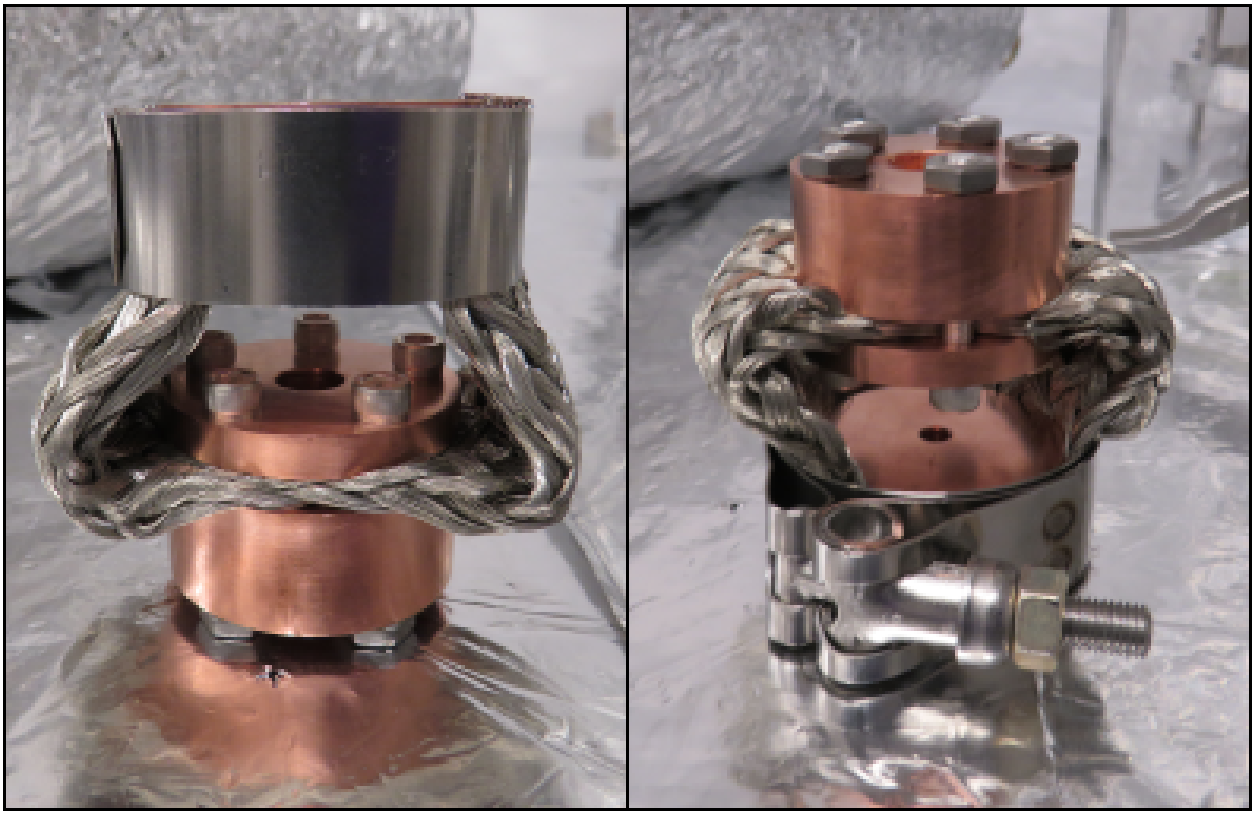

Figure 3-16: The high-power connector sub-assembly. A 00 AWG tin-coated grounding braid is used to conduct heat between the cold-finger and the divider top-plate. The grounding braid is clamped between two C101 copper disks using five 8-32 stainless-steel screws, forming the 'bottom-side' connector; the grounding braid is fixed to the sides of another C101 copper disk using a stainless-steel high-torque pipe clamp, forming the 'top-side' connector. The 'true' orientation of the high-power connector is shown in the left panel: a flat-head stainless-steel is underneath the grounding braid, so that the high-power connector can be fixed to the tapped hole inside the cold-finger. The 'top-side' of the high-power connector is tapped with a stainless-steel helicoil for an 8-32 screw.

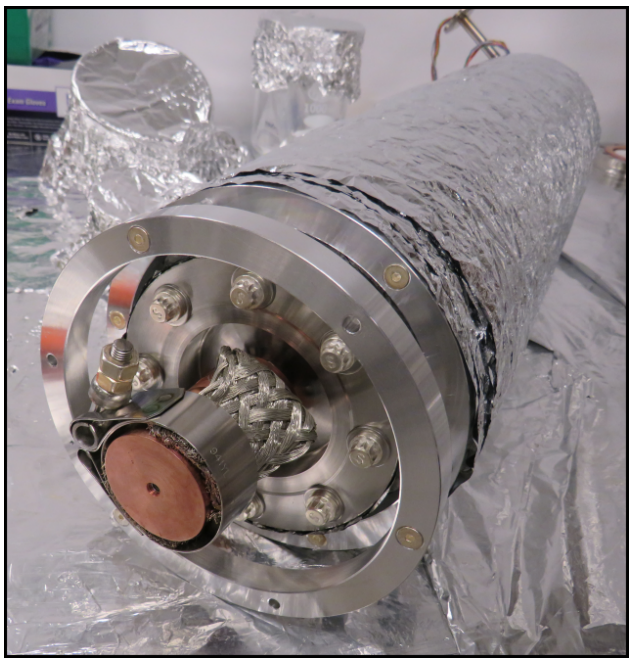

Figure 3-17: The inner rings and dewar, wrapped in MLI, with the thermal-switch assembly attached. The inner ring assembly is lowered into the outer ring assembly, as shown in Figure 3-14. A flat-head stainless-steel screw is used to join the divider top-plate to the tapped hole in the 'top-side' of the high-power connector. All mating surfaces are coated with high-vacuum grease to aid in thermal conductivity. The MLI is not wrapped to the top of the inner ring assembly to allow the placement of thermocouples.

with stainless-steel helicoils to the same bolt pattern as the 12" reducer flange, which acts as a plate-nut; the plate nut is mounted on an aluminum-extrusion stand. The LIN plumbing and slow-control cables use a feedthrough flange that is mounted on the bottom cross. Stainless-steel bellows are welded to the LIN plumbing feedthrough; the bellows are terminated by demountable VCR connections that mate to the dewar. The slow-control cables are fixed to the inner walls of the bottom cross using Kapton tape; a short length of the cables ($\sim$ 6") are bunched up near the feedthrough flange so that the electrical feedthroughs can be removed without demounting the LIN plumbing. Figure 3-18 shows the bottom cross, mounting stand, and feedthroughs.

The SiPMs will be mounted on a removable copper disk (SiPM mounting-plate) that sits atop the SiPM top-plate, and are operated using 10 coaxial cables. The coaxial cables are Kapton insulated with a 32 AWG braided core. Because the thermal conductivity of the coaxial cables is large, before connecting to the SiPMs, the cables are temperature attenuated to the SiPM top-plate. The temperature attenuation is accomplished by clamping the coaxial cables to the bottom of the SiPM top-plate with an aluminum plate. The attenuated cables are terminated with PEEK push-on connectors, ready to be mated with cabling from the

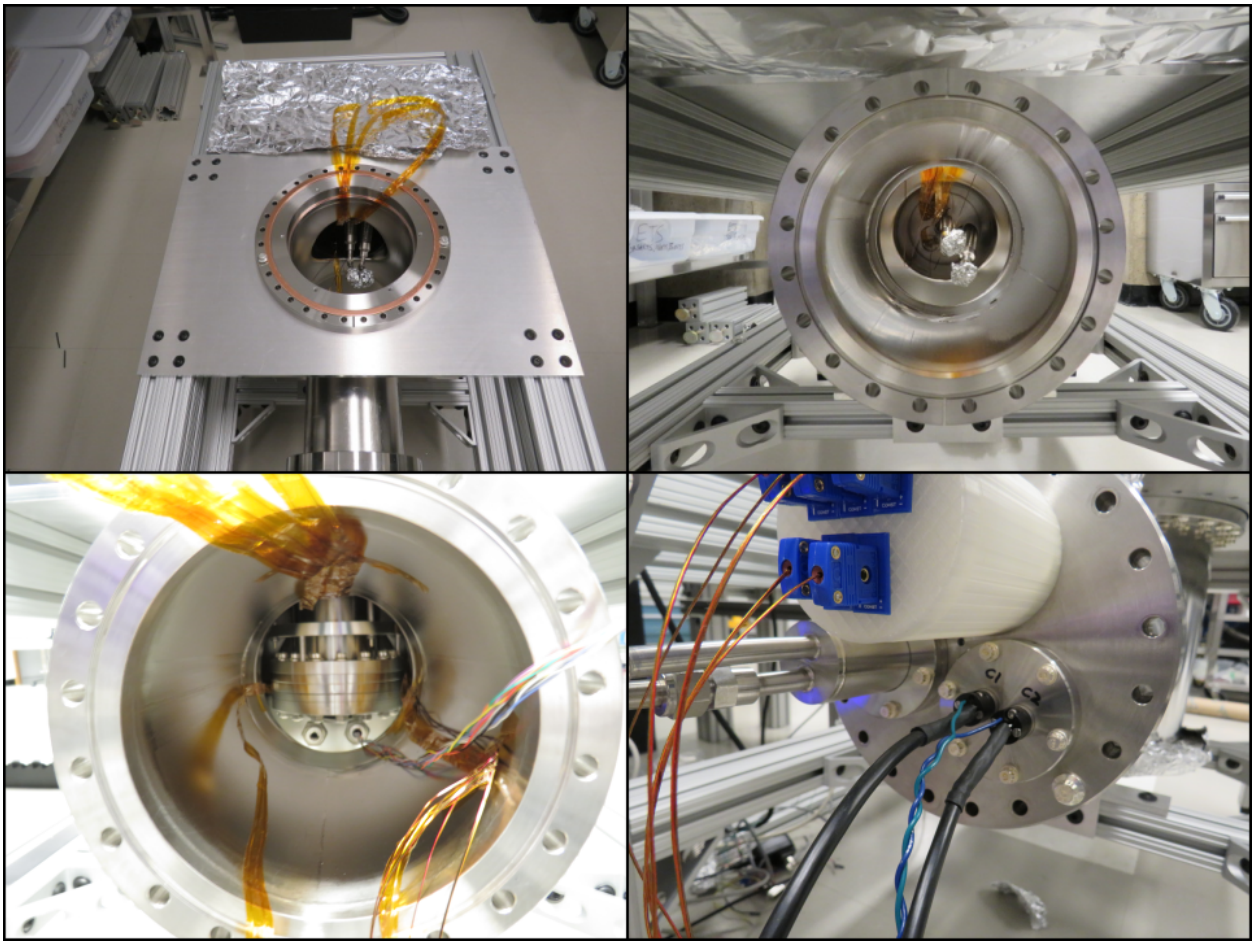

Figure 3-18: The bottom section of the environmental test stand vacuum chamber with feedthroughs. The top-left panel shows the bottom cross atop the aluminum plate nut, which is mounted to the aluminum stand. The bellows and cabling can be seen in the opening of the cross. The top-right panel shows the opposite side of the feedthrough flange, where the pump is mounted. The bottom-left panel shows the ETS dewar with the feedthrough flange removed; the VCR connections can be seen beneath the dewar. The bottom-right panel shows the feedthrough flange attached with all interconnections: thermocouples at the 12 o'clock position, RTDs and electrical power at the 4 o'clock position, and LIN plumbing at the 8 o'clock position.

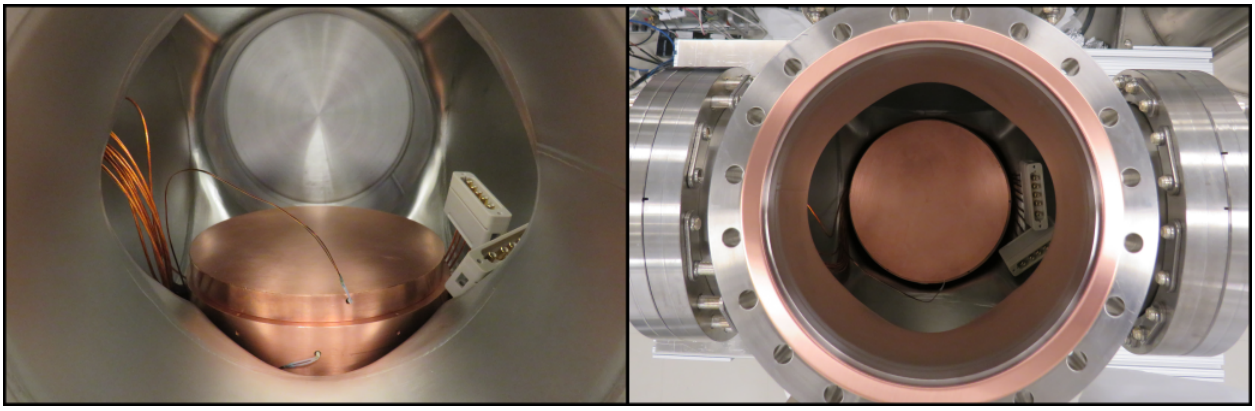

Figure 3-19: The environmental test stand SiPM mounting- and top-plate, assembled within the vacuum chamber. The left panel shows the view from the access port, where the mounting-plate can be removed. The coaxial cables can be seen on the left where they disappear underneath the SiPM top-plate for temperature attenuation, then reappear on the right side, and terminate with PEEK push-on connectors. Several RTDs can be seen embedded in the SiPM top-plate for temperature measurement. The right panel shows the SiPM mounting-plate from above, where optical elements will be used to scan the SiPMs.

mounted SiPMs. Figure 3-19 shows the SiPM mounting- and top-plate and Figure 3-20 shows the assembled environmental test stand.

The leak rate for all of the welds and demountable connections were tested using a helium leak-checker, and found to remain leak-tight up to 10^{-12} Torr l/s (the limit of the detector). The leak rate of the cold-finger flange was also verified at cryogenic temperatures by submerging the top of the dewar in LIN for $\sim$ 5 min, then removing it from the LIN and immediately checking the brazed joint. This test was repeated four times: twice a leak was found at $\sim 10^{-8}$ Torr l/s, and twice no leak was found up to 10^{-12} Torr l/s. In the former case, after about $\sim$ 2 min, the leak-rate had fallen bellow 10^{-12} Torr l/s. This result suggests a reversible leak in the brazed joint, however the maximum leak-rate measured (10^{-8} Torr l/s) is too small to be significant for the $\sim$ 100 l system.

3.5.2 Slow Controls

Primary temperature measurement is done at the SiPM top-plate using three platinum (PT-101) resistance temperature detectors (RTDs). The device lead wires are connected to an 18

pin Sub-C electrical feedthrough, which is connected to a Model 350 Cryogenic Temperature Controller through two shielded CAT8 RJ45 cables. Three polymide resistive heaters are fixed to the aluminum posts that join the SiPM top-plate to the divider top-plate, and are powered through the Model 350 using a PID feedback system. The polymide heaters are connected in parallel using 24 AWG bare wire, that is insulated using Kapton tape, and connected to the remaining two pins of the Sub-C feedthrough. A spare RTD is hanging freely in the top cross for future use.

The secondary temperature measurements are done using five T-type thermocouples that are fixed to the cryostat at several locations. These locations are chosen to understand both the evolution of the system from room temperature to steady-state, and to provide test data for the thermal-network model. T-type thermocouples are chosen because of their accuracy/repeatability at low temperatures, and robustness in an alternating oxidizing/reducing atmosphere. The thermocouples are constructed with 24 AWG bare copper/constantan wire, twisted and spot welded at the junction between the two materials. The malleable welded junction is hammered into a flat probe-end that is fixed to the cryostat with Kapton tape. Each thermocouple pair is made into an insulated ribbon cable by using two long pieces of Kapton tape, stuck together with the wires inside. External thermocouples are used to carry the signal through the feedthrough flange, to a LabJack T7 ADC where the thermoelectric voltage is measured deferentially; a LM94021 thermistor is used as a reference temperature by the LabJack.

The LIN level is monitored using a sensor-rod that is constructed using common resistors and LEDs. The sensor-rod is composed of 24 resistors that have a high temperature coefficient of resistivity, and are fixed 20 mm apart within an acrylic tube. Four resistors are connected in series to form a channel, yielding six channels with a common ground. Two green LEDs with a temperature dependent forward voltage are placed at the 1/3 and 2/3 point along the sensor rod, acting as secondary sensors, forming two additional channels. The cabling is fed through the LIN return line and integrated with a voltage divider for each

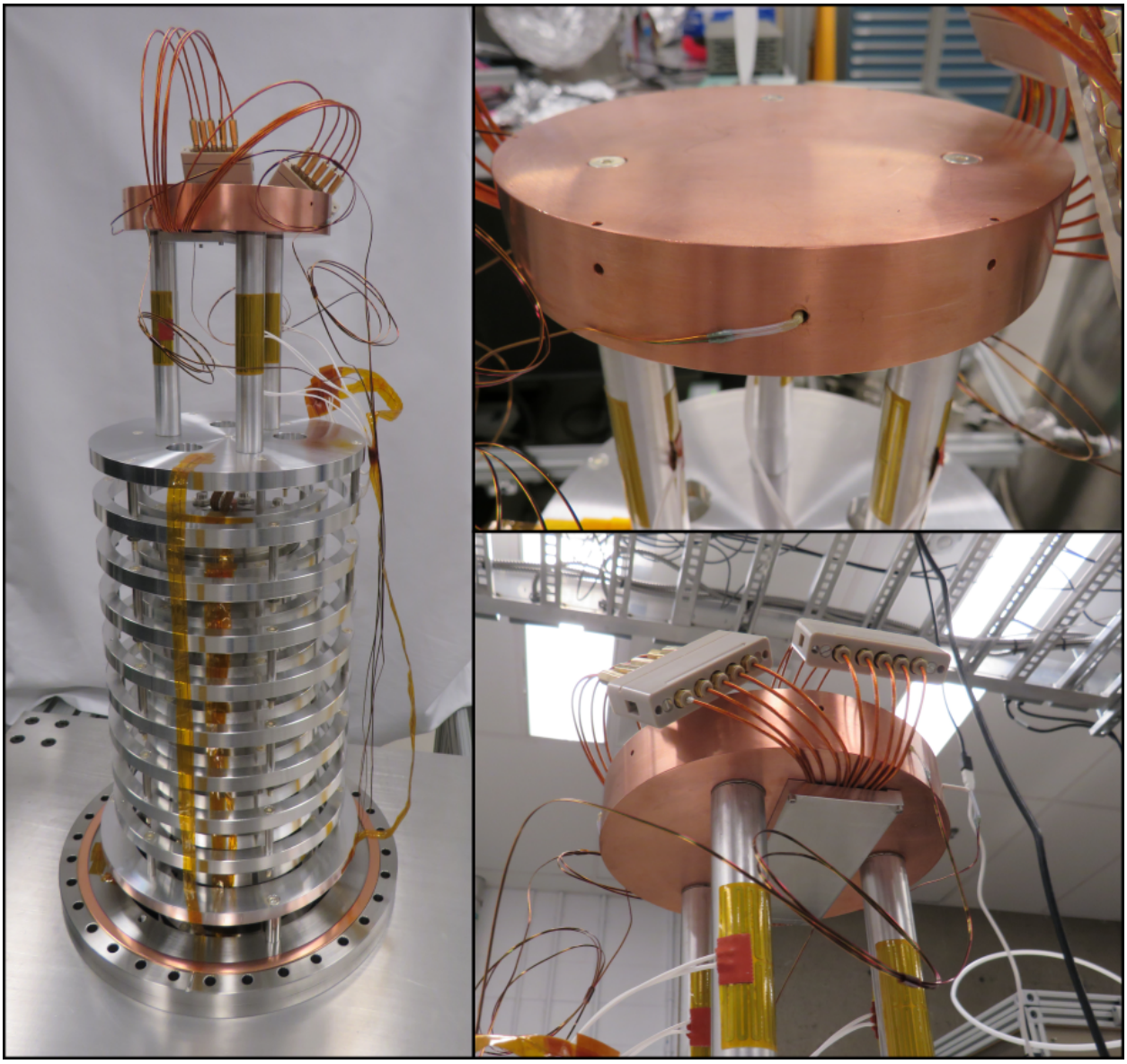

Figure 3-20: The full environmental test stand assembly. The left panel shows the environmental test stand with temperature monitoring and control cables attached. The thermocouples can be seen running along the center of the assembly, where they are attached at various locations; the cabling for the polymide heaters and RTDs can be seen running along the right side. The polymide heaters are connected in parallel, and fixed to the aluminum posts that join the divider top-plate to the SiPM top-plate. The RTDs are mounted within the SiPM top-plate using vacuum grease. The top-right panel shows a close-up of an RTD mounted inside of the SiPM top-plate. The bottom-right panel shows the coaxial cables clamped to the SiPM top-plate for temperature attenuation, using an aluminum plate.

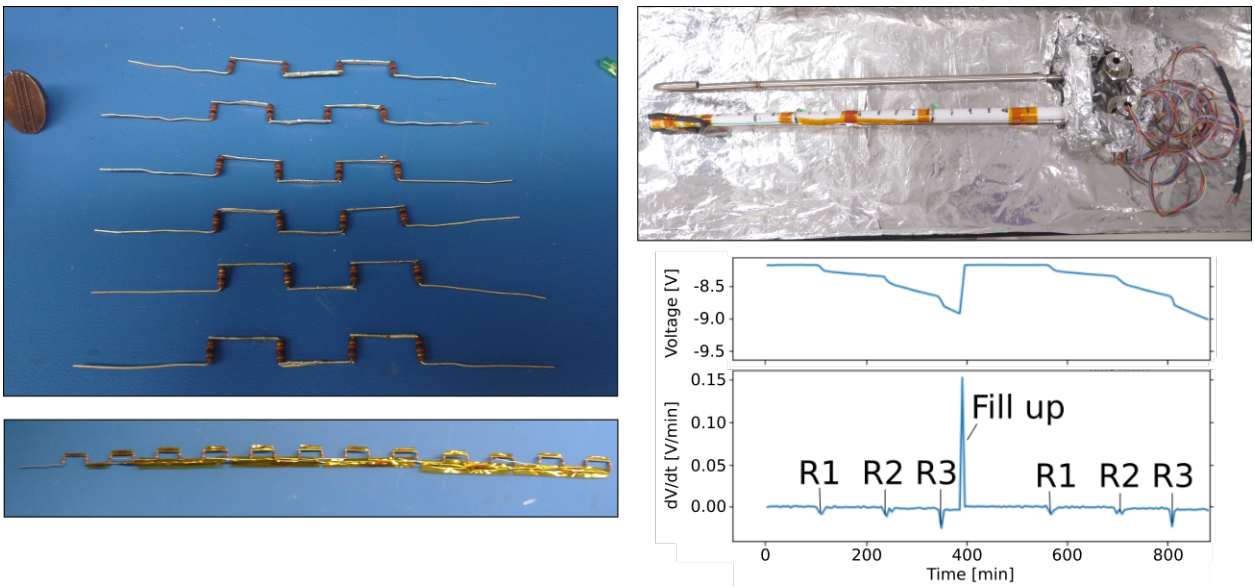

Figure 3-21: The LIN sensing rod. The left panel shows four series resistors that form a channel for the LIN level sensing-rod. Each channel is connected in parallel with a common ground which allows a 260 mm range for determining the LIN level, in steps of 20 mm. The top-right panel shows the LIN sensing rod, fixed to the return line. The sensor cabling is fed through the return line and integrated into an external voltage divider where the temperature dependent resistance is measured. The bottom right panel shows voltage measurements for a prototype sensor channel. When the liquid nitrogen level falls below a resistor, its resistance decreases, and the corresponding voltage change is measured using a voltage divider. By simultaneously viewing the time-derivative of the voltage, the change in resistance caused by the LIN level can be seen clearly as spikes in the graph.

channel. Each channel uses an input voltage of 15 V, and the divided voltage is measured using a LabJack T7 ADC. The resistance of each resistor changes from 10 kΩ at ambient temperature ($\sim$ 293 K) to $\sim$ 18 kΩ when submerged in LIN ($\sim$ 77 K); similarly the forward voltage of the green LEDs changes from 5 V to 10 V. The temperature dependence is large enough in the resistors that when the LIN level falls below them, enough heat is dissipated to see a clear step in the divided voltage after $\sim$ 5 min; the effect is less pronounced in the LEDs, and can be seen as a more gradual slope after $\sim$ 30 min. Figure 3-21 shows the sensor rod and a plot characterizing a single resistor channel for the sensor rod using LIN.

A Pirani gauge is used to measure the pressure within the vacuum chamber. Figure 3-22 shows a cross-section of the environmental test stand with the locations for each device in the slow-control system labelled.

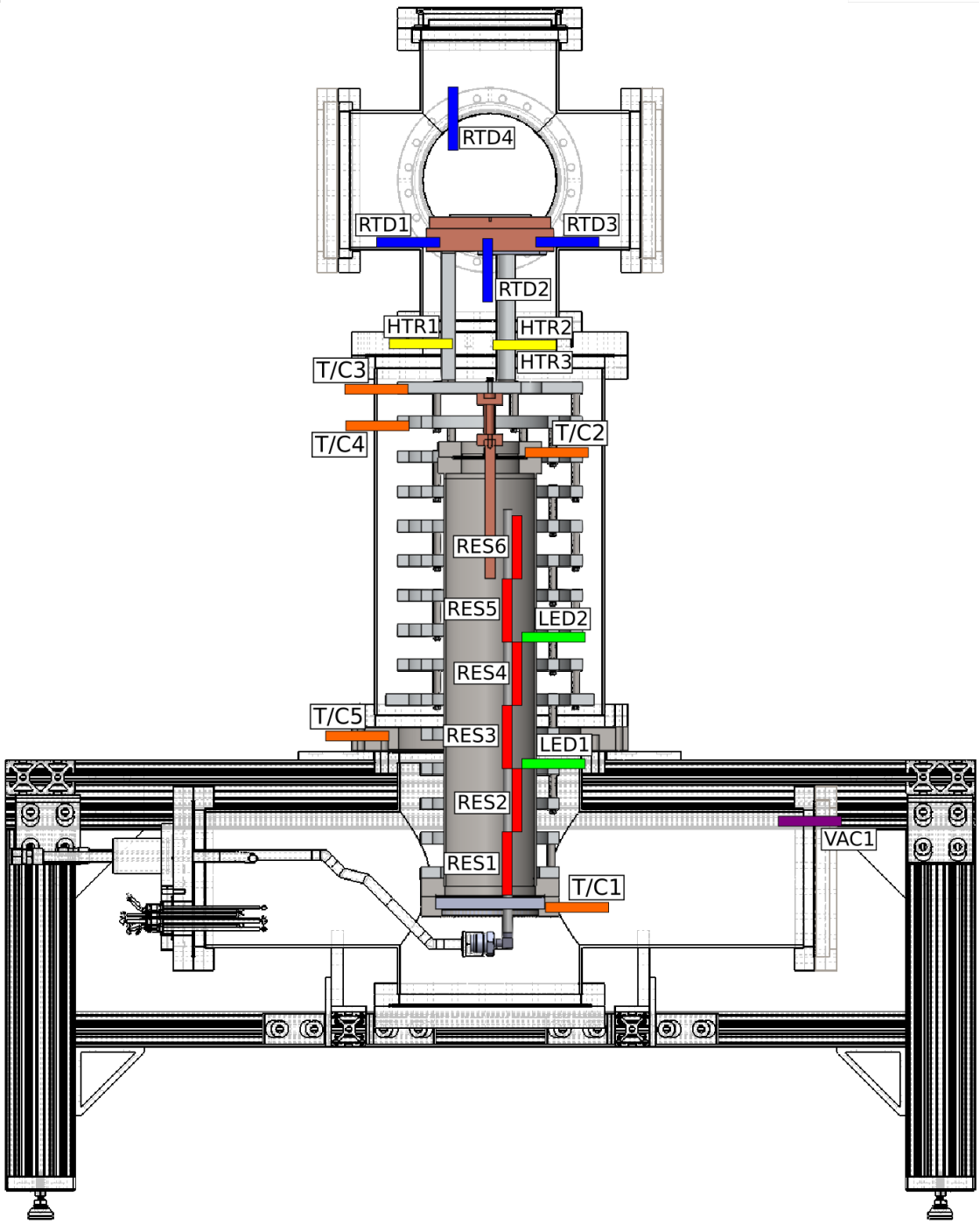

Figure 3-22: The slow-control system for the environmental test stand cryostat. The temperature of the SiPM top-plate is measured with three PT-101 RTDs, and is regulated with a PID controller and polymide heaters. Five T-type thermocouples are used to measure the temperature at various locations across the divider. A sensing rod is placed within the dewar to measure the LIN level using temperature dependent resistors and LEDs. A Pirani gauge is used to measure the pressure within the vacuum chamber. A spare PT-101 RTD is freely hanging by the top-plate.

3.6 Data Acquisition

A python computer program interfaces with the LabJack and writes the voltage values to a text file with a specified frequency. A second computer script queries the text file and plots the processed data over any time range, and updates the plot with a specified frequency. This combination allows real-time monitoring of the slow-control data.

3.7 Commissioning

Two commissioning runs have been completed to test the operation of the cryostat: the first run to test the cryostat and slow control system, and the second to verify the integrity of the vacuum system at cryogenic temperatures; MLI was not used in these first two tests (ETSv3a).

The first commissioning run was conducted with ~ 1 atm of nitrogen within the vacuum chamber: the top flange of the vacuum chamber was replaced with a piece of aluminum foil. Then nitrogen gas was blown into the vacuum chamber, from the bottom, to displace oxygen and water; the over-pressurization caused the aluminum foil to inflate slightly, then air began to leak from the sides. After ~ 5 h, the aluminum foil was replaced with a CF-flange, and the dewar was filled with LIN. After ~ 1 h, LIN began flowing out of the return line, indicating that the dewar was full. The slow controls were monitored for ~ 3.5 h; Figure 3-23 shows the results from the test. The power of the cryostat was calculated using the rate of LIN vaporization through the LIN level sensors; it was found that the cryostat consumed ~ 200 W of power, indicating significant conduction through the gas; Figure 3-24 shows the bottom of the vacuum chamber, iced from conduction through the nitrogen gas. All systems operated as intended, indicating a successful test.

The results from the second commissioning run are shown in Figure 3-25. A dry scroll pump[11] was used to provide the vacuum for the cryostat. When the pressure in the chamber fell to $\sim 2 \cdot 10^{-3}$ Torr, the dewar was filled with nitrogen. When nitrogen started flowing

[11] Edwards XDS 10 dry scroll pump, 10 m^3/h

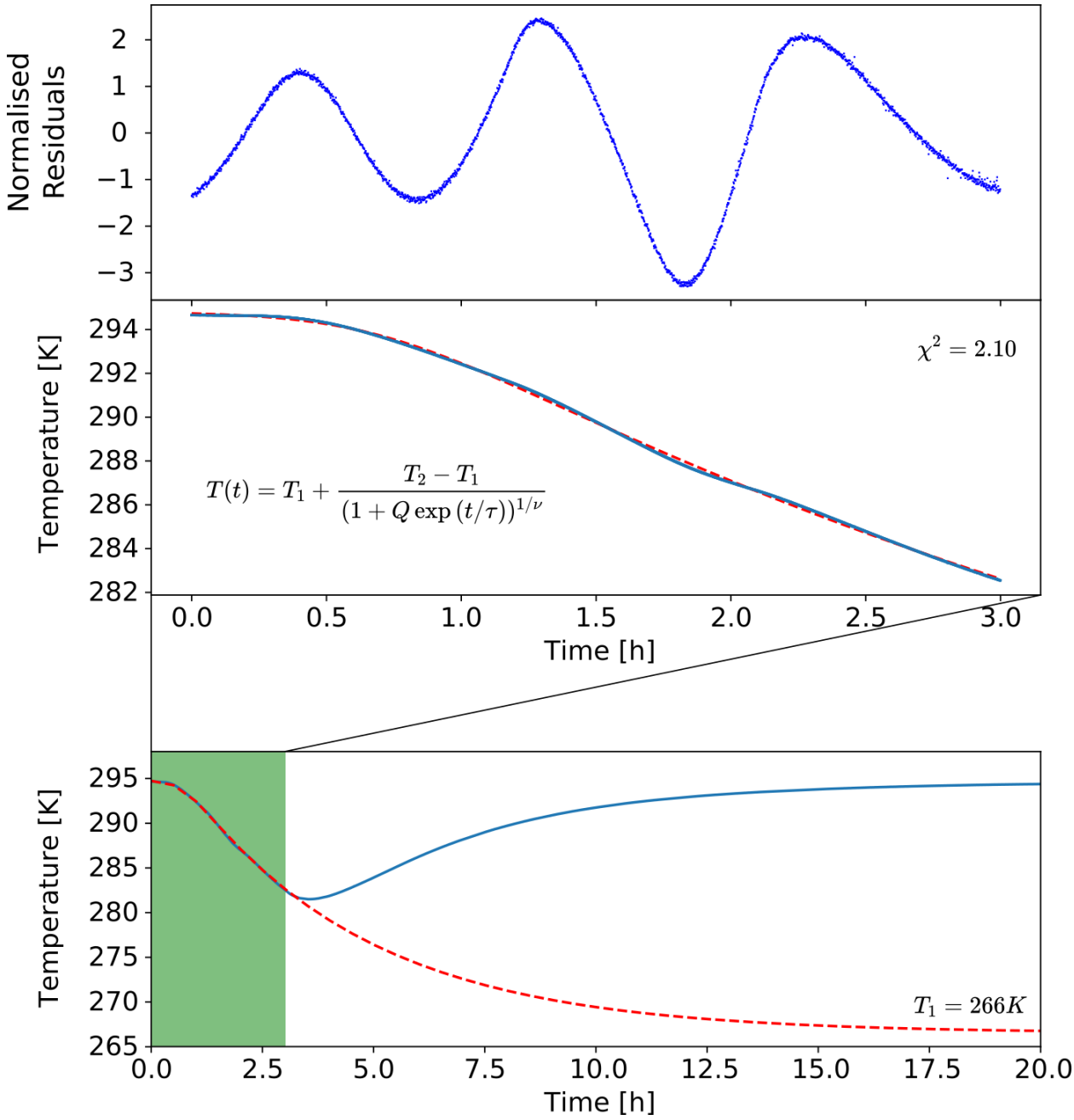

Figure 3-23: Data from the first commissioning run. The bottom plot shows the temperature at the SiPM top-plate (blue), and an extrapolation (red) by fitting the data in the shaded green region using a generalised logistic function. The top plots show a blow-up of the shaded green region, where the residuals have been normalised by the standard error for each measurement. The temperature measurements from the three RTDs are averaged, and have a standard error of $100/\sqrt{3}$ mK, which is not visible in the scale shown. The LIN level falls over time, so the power is also reduced; the power increases when the dewar is 'topped up.' The oscillation in the residuals may be affected by this phenomenon.

Figure 3-24: The bottom of the vacuum chamber, iced from conducting heat between the LIN dewar and the chamber walls. Using the LIN level sensors, the power consumption of the cryostat is calculated to be $\sim$ 200 W, which is an order of magnitude greater than the estimated value for the cryostat in an ideal vacuum.

into the system, the pressure dropped further to $\sim 1.4 \cdot 10^{-3}$ Torr. After about $\sim$ 45 min, LIN began flowing out of the return line, indicating that the dewar was full. By monitoring the LIN level sensors, it was determined that the power consumption of the cryostat was $\sim$ 34 W, which is $\sim$ 16 W more than the expectation from radiation[12] and conduction in a vacuum. The valve to the vacuum chamber was closed, and the scroll pump was replaced with a turbo molecular pump, backed by a smaller dry scroll pump[13]; a cold-cathode gauge (CCG) was used to measure the vacuum pressure by the turbo molecular pump. When the valve was opened, the CCG read a steady-state pressure of $\sim 2 \cdot 10^{-5}$ Torr. Through three fill-up cycles, it was determined that the power consumption of the cryostat was $\sim$ 22.5 W, which is $\sim$ 4.5 W more than the expectation from radiation and conduction in a vacuum. At $\sim$ 14 h, the cryostat was left to continue running overnight. By the next morning, the SiPM top-plate had warmed by $\sim$ 5 K, and the dewar was nearly empty. The dewar was refilled and the previous tests were repeated. Again, it was found that the power consumption of the cryostat was $\sim$ 22.5 W. A final test was performed with a full dewar by closing the valve to the turbo molecular pump. Immediately after closing the valve, the pressure in the vacuum chamber began to rise at a rate of $\sim$ 0.12 mTorr/min, as read by the Pirani gauge; the temperature of the SiPM top-plate began to rise at a rate of $\sim$ 23 mK/min, and the

[12]Considering only the dewar was at low temperature, the radiative load should be less than 17 W, which was calculated for the system at steady state.

[13]Edwards EXPT pumping station: EXT75DX turbomolecular pump, $> 10^1 1$ inlet compression ratio for N2, and XDS 5 dry scroll pump, 5 m^3/h.

temperature of the free RTD began to fall at a rate of ~ 120 mK/min; this test was repeated with the same outcome, and the results are shown in Figure 3-26. The valve was left closed, and the pressure rose to an asymptotic value of $\sim 3 \cdot 10^{-2}$ Torr at ~ 37 h. A thermocouple was attached at various locations to the walls and flanges of the vacuum chamber, with room temperature measured as a reference. The top cross was found to be ~ 1 K below room temperature, while the middle nipple and bottom cross were found to be ~ 5 K below room temperature; the coldest locations on the vacuum chamber were the locations that froze during the initial commissioning run in 1 atm of nitrogen. At ~ 40 h, the rate of pressure increase rose to $\sim 1.25 \cdot 10^{-2}$ Torr/min, reaching an asymptotic value of ~ 300 Torr after about 5 h; the acceleration was coincident with the dewar reaching ~ 230 K, suggesting the vaporization of frozen water [57]; the pump data is shown in Figure 3-27.

The results of the second commissioning run are summarized below:

- Power consumption ~ 34 W at $\sim 1.4 \cdot 10^{-3}$ Torr, 17 W more than calculation for ideal vacuum.
- Power consumption ~ 22.5 W at $\sim 2 \cdot 10^{-5}$ Torr, 4.5 W more than calculation for ideal vacuum.
- A fit to the data suggests an asymptotic temperature of ~ 194 K at the SiPM top-plate, after ~ 40 h.
- The system was leaking at a rate of ~ 0.12 mTorr/min.
- When the valve to the pump was closed, the SiPM top-plate warmed at a rate of ~ 23 mK/min, and the free RTD cooled at a rate of ~ 120 mK/min.
- The vacuum chamber was coldest at the locations consistent with conduction through gas within the vacuum chamber.

The decrease in power consumption after the vacuum was improved suggests that heat was lost by conduction through the gas. Extrapolating the data shows a steady-state tem-

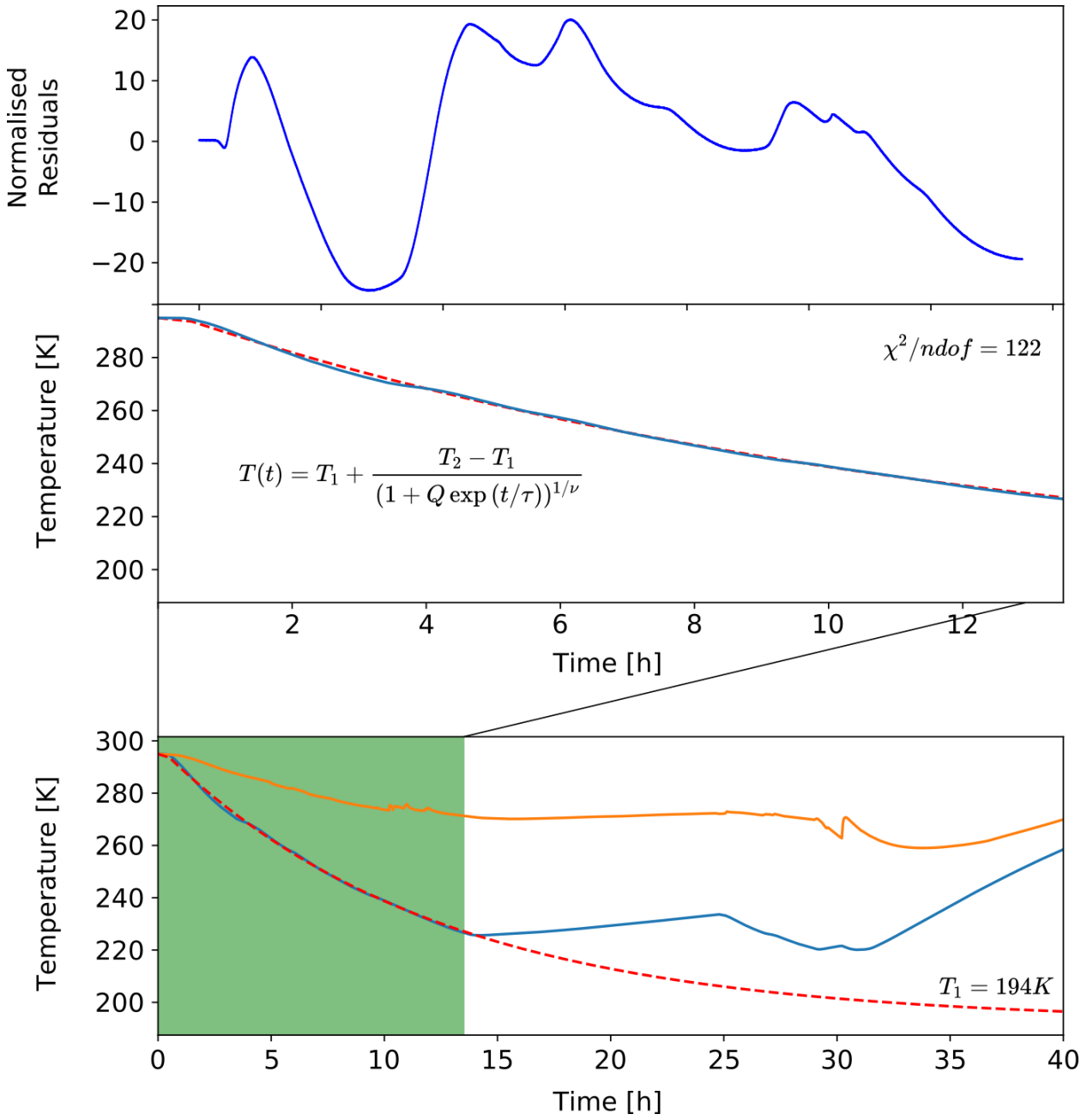

Figure 3-25: Data from the second commissioning run. The bottom plot shows the temperature at the SiPM top-plate (blue), the free RTD (orange), and an extrapolation (red) by fitting the data in the shaded green region using a generalised logistic function. The top plots show a blow-up of the shaded green region, where the residuals have been normalised by the standard error for each measurement. The temperature measurements from the three RTDs are averaged, and have a standard error of $100/\sqrt{3}$ mK, which is not visible in the scale shown. The larger amplitude in the residuals compared to the first commissioning run may be explained through the systematics of the experiment, which were less controlled than in the first commissioning run.

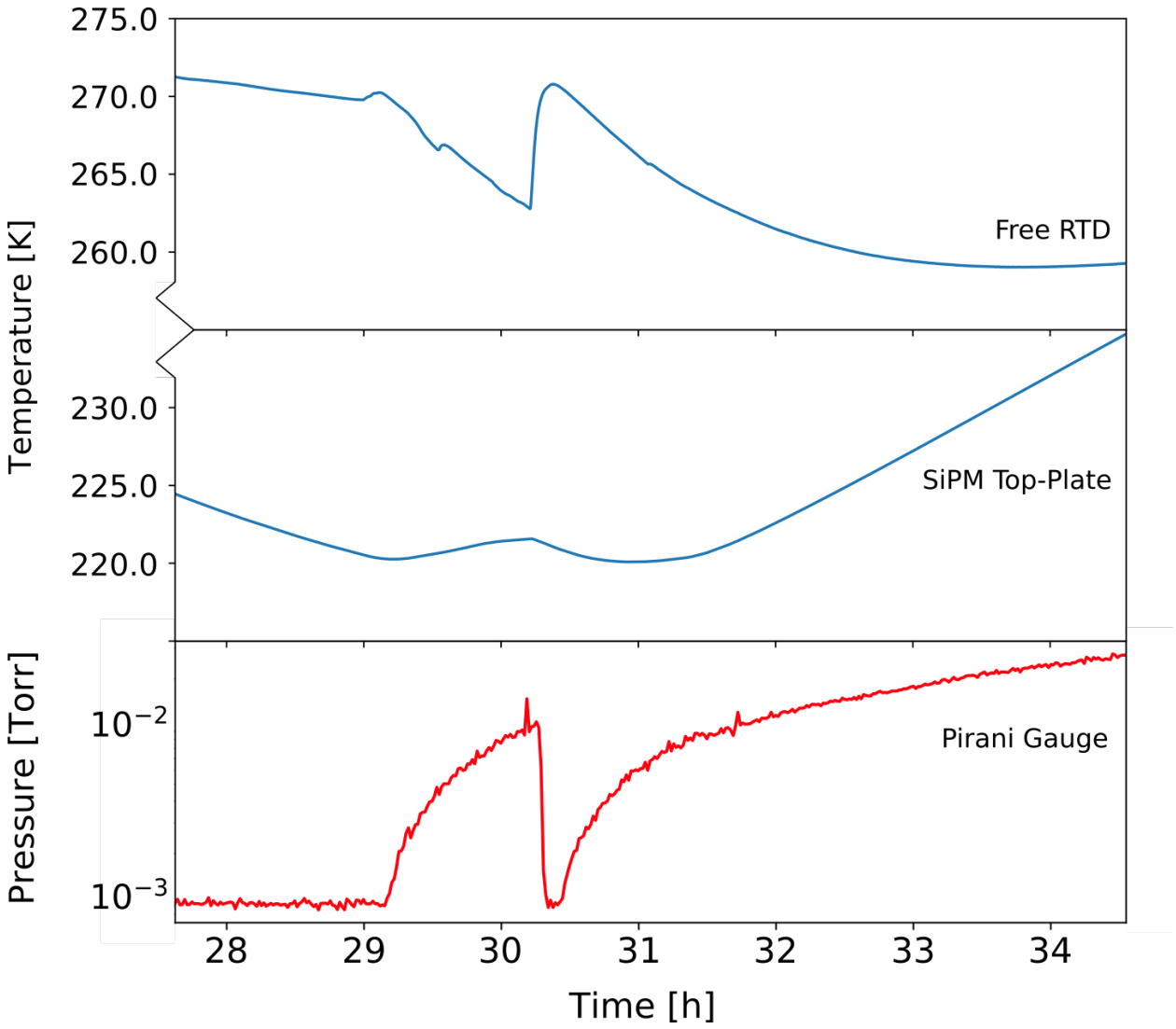

Figure 3-26: Data from the second commissioning run. An anticorrelation can be seen between the temperature measured at the free RTD and the SiPM top-plate; the changes in temperature are correlated with the pressure change in the vacuum chamber. The simplest explanation for the anticorrelation is that the cryostat equilibrates by conduction through vapor.

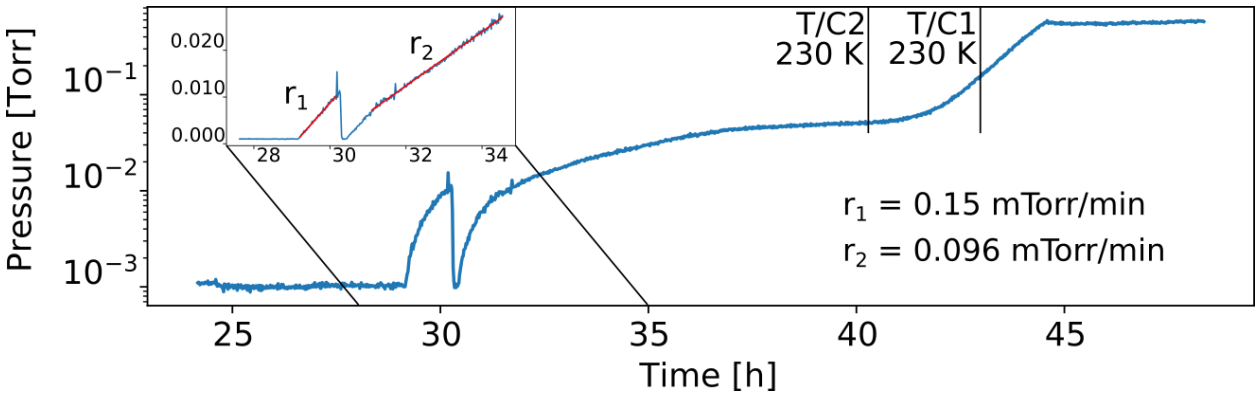

Figure 3-27: Pump data from the second commissioning run; data before 25 h is omitted as the pressure is below the measurement threshold for the Pirani gauge. The inlay shows a linear plot of the pressure, with a fit to the pressure change, giving the leak-rate. At $\sim$ 40 h the temperature of the dewar begins to warm above the freezing point of water, vaporizing the cryopumped particles.

perature at the SiPM top-plate that is significantly warmer than what was expected through simulations, which was reached $\sim 3\times$ later. The system was found to be leaking; when the valve to the pump was closed, the SiPM top-plate warmed, while the spare RTD cooled, indicating the system was equilibrating. Considering the totality of these results, it is likely that gas within the vacuum chamber, generated by some leak, was conducting heat between the cryostat and the warm vacuum chamber, and thermally shorting out elements within the cryostat.

Following the second commissioning test, helium was blown into the warm dewar while pumping on the vacuum chamber, and a leak was detected at a rate of $\sim 10^{-8}$ Torr l/s. The system was disassembled and checked again for leaks; no leaks were detected when the parts were checked independently. The system was reassembled with MLI (ETSv3b) and a virtual leak was detected somewhere in the bottom cross at a rate of $\sim 10^{-8}$ Torr l/s; although this leak is small, it may be exacerbated after thermocycling to cryogenic temperatures. The location of the leak is likely the demountable LIN lines since they are the only components that were checked independently, but not in their final mating configuration. A larger pumping station (turbo molecular pump backed by a scroll pump) has been ordered to mitigate any heat transferred through vapor, and is expected to arrive in early 2020.

4 Xenon Impurities

4.1 Charge Attenuation via Electronegative Impurities

In an ideal noble liquid TPC, all electrons that escape recombination will be collected at the anode. In a real noble liquid TPC, electronegative impurities diffusive into the system and attenuate the charge collected by the anode through electron capture: due to the large difference in mass, the ions formed through electron capture drift significantly slower than electrons under the same electric field, thereby escaping collection within the scintillation-triggered window. There are three dominant modes for electron capture in noble liquids by a neutral atom or molecule AB [61]:

(1) Radiative attachment

$e^- + \mathrm{AB} \rightarrow \mathrm{AB}^- + \mathrm{h}\nu.$

(2) Dissociative attachment

$e^- + \mathrm{AB} \rightarrow \mathrm{AB}^* + e^- \rightarrow \mathrm{A}^+ + \mathrm{B}^- + e^-$

$e^- + \mathrm{AB} \rightarrow \mathrm{AB}^- \rightarrow \mathrm{A} + \mathrm{B}^-.$

(3) Three-body attachment through the two-stage Bloch-Bradbury reaction

$e^- + \mathrm{AB} \rightarrow (\mathrm{AB}^-)^*$

$(\mathrm{AB}^-)^* + \mathrm{Xe} \rightarrow \mathrm{AB}^- + \mathrm{Xe}.$

The radiative attachment mode has a small cross-section, and the dissociative attachment mode requires much higher electron energies than can be expected under modest drift fields in LXe [61], therefore the two-stage Bloch-Bradbury reaction is the dominant electron capture process in EXO-200; the reaction follows a first-order rate law, and so the number of free electrons $N(t)$ is given by

$$N(t) = N_0 e^{-t/\tau_e}, \tag{39}$$

where N_0 is the original number of electrons, and τ_e is the electron lifetime, which in turn is given by

$$\tau_e = \sum_i k_i n_i, \tag{40}$$

where k_i and n_i is the rate constant and concentration for the i-th impurity species, respectively.

4.2 EXO-200 Purity Calibration

In EXO-200, electron lifetime is determined through calibration runs performed approximately three times per week, every other week day. These regular calibrations are performed by deploying a ^{228}Th source to a known location outside of the TPC: a 2615 keV gamma excites and ionizes the xenon; the gamma is emitted from ^{208}Tl, which is an isotope in the ^{232}Th decay chain. A diagram of the EXO-200 vessel with the source deployment locations is shown in Figure 4-1, and the charge/light measurements of a ^{228}Th calibration run are shown in Section 1, Figure 2-6. Following a calibration run, the method for determining the electron lifetime is as follows: each TPC[14] is divided into 13 bins along the z-axis, where the z-position and ionization energy are both fitted simultaneously through Monte Carlo based algorithms (MC2D) developed by the EXO-200 collaboration [62], allowing the extraction of the electron lifetime as a fit parameter. The uncertainties for the electron lifetime are asymmetric and grow with increasing electron lifetime. The causes for these features in electron lifetime uncertainties are well understood: a Compton shoulder at the low-energy

[14]EXO-200 utilizes a common cathode, allowing two 'twin' TPCs

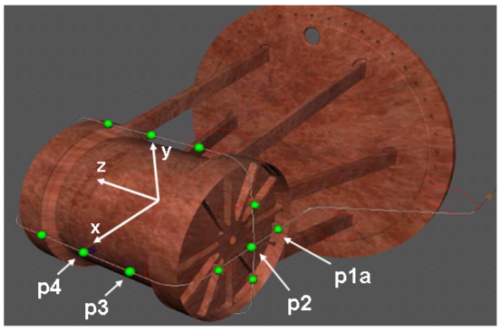

Figure 4-1: Calibration source deployment locations for the EXO-200 detector. The regular calibration runs use a ^{228}Th source deployed to the p4-x location for $\sim$ 4 hours; other source types (^{60}Co, ^{226}Ra) and locations are used during less regular calibration cycles.

side of the ionization energy spectrum causes the asymmetry; at long electron lifetimes the charge attenuation is approximately linear, which makes the determination of exponential fitting parameters less precise; at short electron lifetimes the charge attenuates to nearly its asymptotic value, which enables precise determination of exponential fitting parameters.

The electron lifetime during low background runs is approximated by fitting polynomial functions to the calibration run data over periods of stable purity. A period of stable purity is defined by a constant circulation through the two-phase xenon purification system. This definition is motivated by studies of the effect of xenon circulation on electron lifetime that suggest 3-5 days after a recovery period and under stable circulation, the electron lifetime should be constant [63]. The goodness of fit parameter was improved by using exponential functions to represent the electron lifetime rather than polynomial functions. However, by adjusting the transition dates between recovery and stability, the polynomial functions could be made nearly identical to the exponential functions, which was found to also optimize the goodness of fit parameter. This 'psuedo-exponential' electron lifetime flavor increased the relative energy resolution by $\sim$ 6%, and is used for the 2018 $0\nu\beta\beta$ analysis [34]. A plot comparing the energy resolution using the standard and 'psuedo-exponential' electron lifetime flavor for a sample period is shown in Figure 4-2. The electron lifetime and purifier flow, with the 'pseudo-exponential' fit, for Phase-II of EXO-200 operations is shown in Figure 4-3.

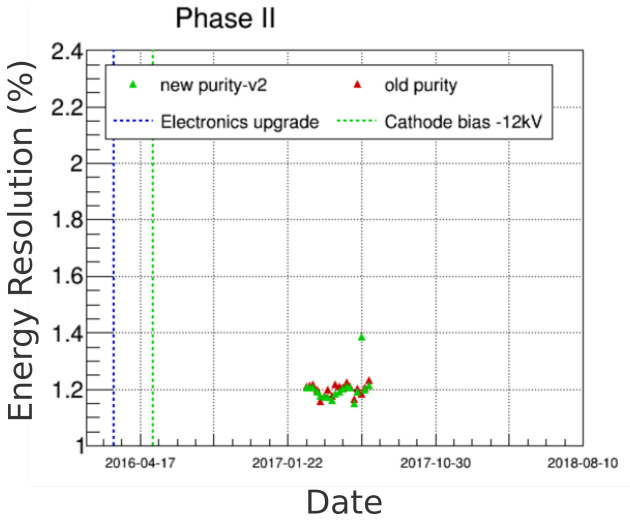

Figure 4-2: A sample period used to evaluate the effect of analysis techniques on energy resolution. The 'old purity' flavor uses polynomial functions with some parameters chosen arbitrarily, yielding an energy resolution of 1.20%; the 'new purity-v2' flavor uses polynomials functions that best match exponential behavior, yielding an energy resolution of 1.19% [64].

4.3 Anomalous Electron Lifetime

Although the flow-based purity model gives consistent results with the measured electron lifetime at low, average, and high circulation rates, there are a large number of anomalously low electron lifetime values during periods of stable circulation. Here, 'anomalously low' is referring to $\sim$ 10% of runs having $\tau_e < \bar{\tau_e} - 2\sigma$, and $\sim$ 5% of runs with $\tau_e < \bar{\tau} - 3\sigma$. A correlation was found between many of the anomalously low electron lifetime dates and the dates when then vacuum-spaces, which insulate the xenon circulation system, were evacuated. In many cases, the vacuum-spaces were pumped $\sim$ 5 minutes before beginning a calibration run, every 1-2 weeks. Figure 4-4 shows a plot of electron lifetime values taken over a three month period, with pump-out dates highlighted by vertical lines. An interesting feature in Figure 4-4 is that the distribution of binned residuals can be described using a bimodal distribution, and that each mode may correspond to whether or not the vacuum-spaces were pumped. However, the period shown only includes 43 runs, so it may not be a representative sample. To increase the data set, all of the residuals for the Phase-II electron lifetime are combined. From this data set, the recovery periods, calibration campaigns, and characterization experiments are removed, since they introduce confounding factors. The remaining runs were taken under similar conditions of stable operation with constant electron lifetime; the distribution of residuals for the combined data set is shown in Figure 4-5.

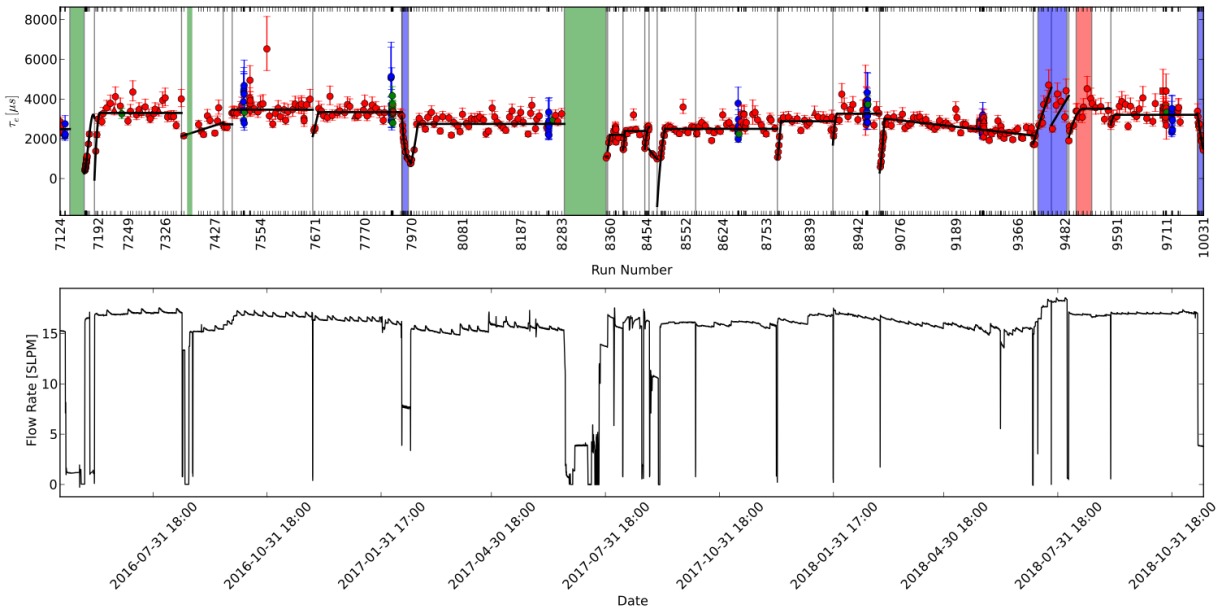

Figure 4-3: Phase-II electron lifetime (top) and averaged flow of xenon in the purification system measured by the 'I-X1' feed-side meter (bottom). The source-types are colored red, blue, and green for weak-Th, weak-Ra, and weak-Co, respectively; the source-positions are shaped circle, square, and triangle for p4-x, p4-y, and combined runs (low-stats), respectively; the green, blue, and red bands indicate power-outages, purifier circulation experiments, and purifier temperature experiments, respectively. The fits are performed using the MINUIT2 solver under the ROOT data analysis package [59].

The hypothesis that evacuating the vacuum-spaces, which thermally isolate the LXe plumbing, systematically lowers the electron lifetime can be traced through a physical process. In LXe, oxygen and water impurities can freeze to the walls. When vacuum-spaces are pumped, pressures throughout the system change, which causes changes in temperatures and liquid levels within the plumbing. When liquid levels fall, newly exposed frozen impurities can vaporize into the warm xenon gas and be introduced to the TPC through the circulation system. If this effect is realized in the detector, then there must be some additional systematic not considered to explain the skewness in distribution of residuals for the pumped vacuum-spaces. Attempts to determine the time-scale for recovery after one of these events have been inconclusive, but xenon purity recovers to its average value by the time of the next calibration measurement (1-2 days).

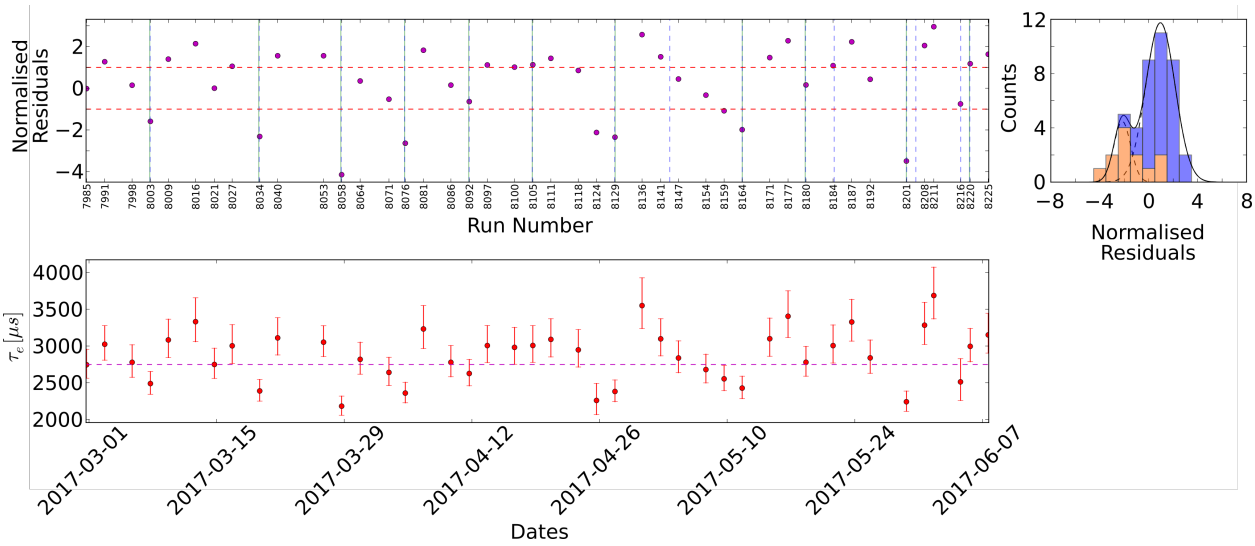

Figure 4-4: Average electron lifetime and residuals for a three month block in Phase-II; the residuals are normalised by the standard error for each measurement. The average electron lifetime is indicated by the dashed-magenta line; the vertical green and blue lines mark the dates where the return- and recovery-line vacuum-spaces are evacuated, respectively. The binned residuals are coloured orange if the vacuum-spaces were evacuated before beginning the calibration run, and blue otherwise. The residuals are described well by a bimodal distribution, and the small and large modes may correspond to pumping the vacuum-spaces.

Figure 4-5: The combined residuals, normalised by the standard error for each measurement, for the Phase-II electron lifetime model, with the recovery periods, calibration campaigns, and characterization experiments removed; the residuals are normalised by the standard error for each measurement. The binned residuals are coloured orange if the vacuum-spaces were evacuated before beginning the calibration run, and blue otherwise. The distribution of residuals is not convincingly bimodal, but the pumped vacuum-space runs clearly skew the overall distribution towards a lower electron lifetime.

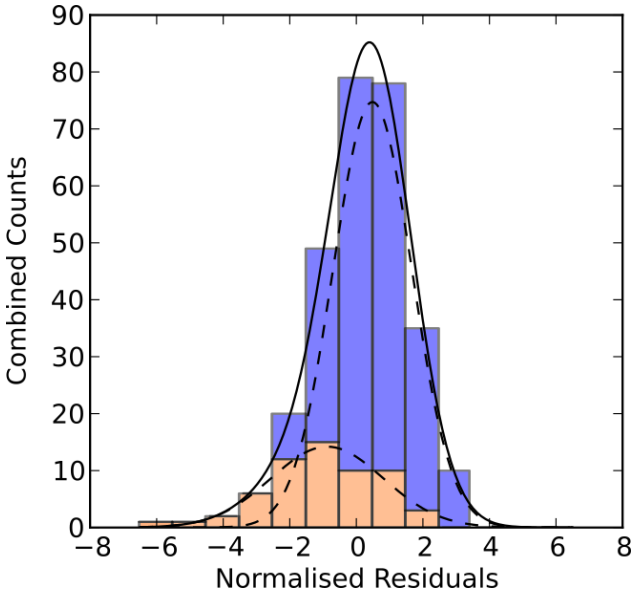

5 Conclusion and Outlook

A thermal-network model was developed as an alternative to the finite-element method to study heat flow, with promising initial results; work on this model is continuing, with the aim for a light-weight simulation package capable of producing transient simulations with surface-to-surface radiation. An environmental test stand for large area testing of silicon photomultipliers has been designed using COMSOL multiphysics, and the thermal-network model. The apparatus has been built, with the commissioning process underway. Upgrades are planned for the slow-control system so that data is saved in a database. Initial testing has shown that the system is not performing as expected due to leaks in the liquid nitrogen supply/return system; tests are underway to determine the vacuum integrity of the cryostat while cold, and a larger pumping station has been ordered to help mitigate this effect, which is expected to arrive in early 2020.

The electron-lifetime model for the EXO-200 detector that was presented in this document improved the energy resolution near the $0\nu\beta\beta$ Q-value over previous models, and was implemented in the final EXO-200 analysis [34]. A systematic error due to regular operations of the EXO-200 detector may have been uncovered, however the low-statistics of this phenomenon make this claim difficult to ground; a systematic study searching for correlations between various slow-control data and the low electron lifetime events is underway.

References

[1] M. Thomson. *Modern Particle Physics*. Modern Particle Physics. Cambridge University Press, 2013. ISBN: 9781107034266.

[2] G. Sterman. *An Introduction to Quantum Field Theory*. Cambridge University Press, 1993. ISBN: 9780521311328.

[3] Bruce T Cleveland et al. "Measurement of the solar electron neutrino flux with the Homestake chlorine detector". In: *The Astrophysical Journal* 496.1 (1998), p. 505.

[4] Hans Albrecht Bethe. "Energy production in stars". In: *Physical Review* 55.5 (1939), p. 434.

[5] E Margaret Burbidge et al. "Synthesis of the elements in stars". In: *Reviews of Modern Physics* 29.4 (1957), p. 547.

[6] Q Retal Ahmad et al. "Direct evidence for neutrino flavor transformation from neutral-current interactions in the Sudbury Neutrino Observatory". In: *Physical Review Letters* 89.1 (2002), p. 011301.

[7] Y Ashie et al. "Measurement of atmospheric neutrino oscillation parameters by Super-Kamiokande I". In: *Physical Review D* 71.11 (2005), p. 112005.

[8] *The Nobel Prize in Physics 2015*. URL: `https://www.nobelprize.org/prizes/physics/2015/summary/`.

[9] RN Mohapatra et al. "Theory of neutrinos: a white paper". In: *Reports on Progress in Physics* 70.11 (2007), p. 1757.

[10] C. Giganti, S. Lavignac, and M. Zito. "Neutrino oscillations: The rise of the PMNS paradigm". In: *Progress in Particle and Nuclear Physics* 98 (Jan. 2018), pp. 1–54. ISSN: 0146-6410.

[11] B Aharmim et al. "Independent Measurement of the Total Active B 8 Solar Neutrino Flux Using an Array of ^{3}He Proportional Counters at the Sudbury Neutrino Observatory". In: *Physical Review Letters* 101.11 (2008), p. 111301.

[12] John N Bahcall, Aldo M Serenelli, and Sarbani Basu. "New solar opacities, abundances, helioseismology, and neutrino fluxes". In: *The Astrophysical Journal Letters* 621.1 (2005), p. L85.

[13] S Abe et al. "Precision measurement of neutrino oscillation parameters with KamLAND". In: *Physical Review Letters* 100.22 (2008), p. 221803.

[14] P Adamson et al. "Measurement of the neutrino mass splitting and flavor mixing by MINOS". In: *Physical Review Letters* 106.18 (2011), p. 181801.

[15] Planck Collaboration. "Planck 2018 results. VI. Cosmological parameters". In: *arXiv:1-807.06209* (2018).

[16] Peter Minkowski. "$\mu \to e\gamma$ at a rate of one out of 109 muon decays?" In: *Physics Letters B* 67.4 (1977), pp. 421–428.

[17] Maria Goeppert-Mayer. "Double beta-disintegration". In: *Physical Review* 48.6 (1935), p. 512.

[18] CPDG Patrignani et al. “Review of particle physics”. In: *Chinese Physics C* 40 (2016), p. 100001.

[19] WH Furry. “On transition probabilities in double beta-disintegration”. In: *Physical Review* 56.12 (1939), p. 1184.

[20] N Abgrall et al. “The large enriched germanium experiment for neutrinoless double beta decay (LEGEND)”. In: *AIP Conference Proceedings*. Vol. 1894. 1. AIP Publishing. 2017, p. 020027.

[21] C Alduino et al. “First Results from CUORE: A Search for Lepton Number Violation via $0\nu\beta\beta$ Decay of ^{130}Te”. In: *Physical Review Letters* 120.13 (2018), p. 132501.

[22] O Azzolini et al. “Final result of CUPID-0 phase-I in the search for the ^{82}Se Neutrinoless Double-β Decay”. In: *Physical Review Letters* 123.3 (2019), p. 032501.

[23] A Gando et al. “Search for Majorana neutrinos near the inverted mass hierarchy region with KamLAND-Zen”. In: *Physical Review Letters* 117.8 (2016), p. 082503.

[24] S Al Kharusi et al. “nEXO Pre-Conceptual Design Report”. In: *arXiv:1805.11142* (2018).

[25] S. Andringa et al. “Current Status and Future Prospects of the SNO+ Experiment”. In: *Advances in High Energy Physics* 2016 (2016), pp. 1–21. ISSN: 1687-7365.

[26] S. I. Alvis et al. “Search for neutrinoless double-β decay in ^{76}Ge with 26 kg yr of exposure from the Majorana Demonstrator”. In: *Physical Review C* 100 (2 Aug. 2019), p. 025501.

[27] M Agostini et al. “Background-free search for neutrinoless double-β decay of ^{76}Ge with GERDA”. In: *Nature* 544.7648 (2017), p. 47.

[28] C Alduino et al. “CUORE sensitivity to $0\nu\beta\beta$ decay”. In: *The European Physical Journal C* 77.8 (2017), p. 532.

[29] KamLAND& Eguchi et al. “First results from KamLAND: evidence for reactor antineutrino disappearance”. In: *Physical Review Letters* 90.2 (2003), p. 021802.

[30] Matthew Redshaw et al. “Mass and Double-Beta-Decay Q Value of ^{136}Xe”. In: *Physical Review Letters* 98.5 (2007), p. 053003.

[31] H Ozaki, A Takeuchi, KamLAND-Zen Collaboration, et al. “Upgrade of the KamLAND-Zen mini-balloon and future prospects”. In: *Nuclear Instruments and Methods in Physics Research Section A* (2019), p. 162353.

[32] Q Retal Ahmad et al. “Direct evidence for neutrino flavor transformation from neutral-current interactions in the Sudbury Neutrino Observatory”. In: *Physical Review Letters* 89.1 (2002), p. 011301.

[33] Sofia Andringa, SNO+ collaboration, et al. “SNO+ present status and prospects”. In: *Journal of Physics: Conference Series*. Vol. 1137. 1. IOP Publishing. 2019, p. 012053.

[34] G Anton et al. “Search for Neutrinoless Double-β Decay with the Complete EXO-200 Dataset”. In: *Physical Review Letters* 123.16 (2019), p. 161802.

[35] T. Takahashi et al. "Average energy expended per ion pair in liquid xenon". In: *Physical Review A* 12 (5 Nov. 1975), pp. 1771–1775.

[36] M. Miyajima et al. "Average energy expended per ion pair in liquid argon". In: *Physical Review A* 9 (3 Mar. 1974), pp. 1438–1443.

[37] E. Aprile et al. "W value in liquid krypton". In: *Physical Review A* 48 (2 Aug. 1993), pp. 1313–1318.

[38] Elena Aprile, R Mukherjee, and Masayo Suzuki. "Performance of a liquid xenon ionization chamber irradiated with electrons and gamma-rays". In: *Nuclear Instruments and Methods in Physics Research Section A* 302.1 (1991), pp. 177–185.

[39] M.A. Zucker M.J. Berger J.S. Course and J. Chang. "Stopping-Power Range Tables for Electrons, Protons, and Helium Ions". In: *NIST Standard Reference Database 124* (2017).

[40] M Agostini et al. "Probing Majorana neutrinos with double-β decay". In: *Science* 365.6460 (2019), pp. 1445–1448.

[41] JB Albert et al. "Sensitivity and discovery potential of the proposed nEXO experiment to neutrinoless double-β decay". In: *Physical Review C* 97.6 (2018), p. 065503.

[42] Akira Hitachi et al. "Effect of ionization density on the time dependence of luminescence from liquid argon and xenon". In: *Physical Review B* 27.9 (1983), p. 5279.

[43] J. H. Hubbell and S. M. Seltzer. "Tables of X-Ray Mass Attenuation Coefficients and Mass Energy-Absorption Coefficients from 1 keV to 20 MeV for Elements Z = 1 to 92 and 48 Additional Substances of Dosimetric Interest". In: *NIST Standard Reference Database 126* (2004).

[44] Juris Meija et al. "Isotopic compositions of the elements 2013 (IUPAC technical Report)". In: *Pure and Applied Chemistry* 88.3 (2016), pp. 293–306.

[45] E Conti et al. "Correlated fluctuations between luminescence and ionization in liquid xenon". In: *Physical Review B* 68.5 (2003), p. 054201.

[46] Shinzou Kubota et al. "Recombination luminescence in liquid argon and in liquid xenon". In: *Physical Review B* 17.6 (1978), p. 2762.

[47] Keiko Fujii et al. "High-accuracy measurement of the emission spectrum of liquid xenon in the vacuum ultraviolet region". In: *Nuclear Instruments and Methods in Physics Research Section A* 795 (2015), pp. 293–297.

[48] Tadayoshi Doke et al. "Absolute scintillation yields in liquid argon and xenon for various particles". In: *Japanese Journal of Applied Physics* 41.3R (2002), p. 1538.

[49] A Hitachi, T Doke, and A Mozumder. "Luminescence quenching in liquid argon under charged-particle impact: Relative scintillation yield at different linear energy transfers". In: *Physical Review B* 46.18 (1992), p. 11463.

[50] E Aprile et al. "Observation of anticorrelation between scintillation and ionization for MeV gamma rays in liquid xenon". In: *Physical Review B* 76.1 (2007), p. 014115.

[51] JB Albert et al. "Cosmogenic backgrounds to $0\nu\beta\beta$ in EXO-200". In: *Journal of Cosmology and Astroparticle Physics* 2016.04 (2016), p. 029.

[52] M Auger et al. "The EXO-200 detector, part I: detector design and construction". In: *Journal of Instrumentation* 7.05 (2012), P05010.

[53] M. Jewell et al. "Characterization of an Ionization Readout Tile for nEXO". In: *Journal of Instrumentation* 13.01 (Jan. 2018), P01006–P01006. ISSN: 1748-0221.

[54] R Neilson et al. "Characterization of large area APDs for the EXO-200 detector". In: *Nuclear Instruments and Methods in Physics Research Section A* 608.1 (2009), pp. 68–75.

[55] *COMSOL Multiphysics v. 5.4. www.comsol.com. COMSOL AB, Stockholm, Sweden.*

[56] Jean Baptiste Joseph Baron Fourier. *The analytical theory of heat*. The University Press, 1878.

[57] Mark O. McLinden Eric W. Lemmon and Daniel G. Friend. "Thermophysical Properties of Fluid Systems". In: *NIST Standard Reference Database 69* (2018).

[58] FJ Richards. "A flexible growth function for empirical use". In: *Journal of Experimental Botany* 10.2 (1959), pp. 290–301.

[59] Rene Brun and Fons Rademakers. "ROOT—an object oriented data analysis framework". In: *Nuclear Instruments and Methods in Physics Research Section A* 389.1-2 (1997), pp. 81–86.

[60] CW Keller, CR Cunnington, and AP Glassford. *Thermal performance of multilayer insulations*. Lockheed Missles and Space Company, 1974.

[61] Elena Aprile et al. *Noble gas detectors*. John Wiley & Sons, 2006.

[62] JB Albert et al. "Improved measurement of the $2\nu\beta\beta$ half-life of ^{136}Xe with the EXO-200 detector". In: *Physical Review C* 89.1 (2014), p. 015502.

[63] P.C. Rowson and Yi-Hsuan Lin. "Simple Model of Xenon Purification in EXO-200". In: *Internal EXO-200 Collaboration Documents* (2017).

[64] Shilo Xia. Private Communication. Jan. 17, 2019.